Dissertation

submitted to the

Combined Faculty of Natural Sciences and Mathematics

of Heidelberg University, Germany

for the degree of

Doctor of Natural Sciences

Put forward by

Alexander Mil

born in: Rudnja, Russia

Oral examination: 29.05.2020

Experimental realization of U(1) gauge invariance in ultracold atomic mixtures

Referees:

Prof. Dr. Fred Jendrzejewski
Prof. Dr. Selim Jochim

Abstract

This thesis reports on the experimental realization of an elementary building block for analog quantum simulation of a U(1) lattice gauge theory in a mixture of two bosonic quantum gases. Experimentally, the building block is realized by Bose-Einstein condensates of lithium (^{7}Li) and sodium (^{23}Na) confined in a single optical dipole trap. Gauge and matter degrees of freedom are mapped in this system onto the internal states of the atomic species. The necessary U(1) gauge invariance is realized via heteronuclear spin changing collisions (SCC) between both species.

The building block represents an important stepstone towards quantum simulation of extended lattice gauge theories as, within the same setting, it features systematic protection of gauge invariance, a realistic approach of the continuum limit for gauge fields and the potential for scalability.

Using SCC, systematic protection of gauge invariance in the system is achieved by exploiting the inherent angular momentum conservation in the atomic mixture. The continuum limit of gauge fields is recovered in the framework of quantum link models by working with Bose-Einstein condensates with high atom numbers in the order of 10^5. The building block can be scaled up to an extended U(1) lattice gauge theory by arranging individual building blocks on the sites of an optical lattice and connecting them via Raman-assisted tunneling.

Great tunability of our experimental building block is demonstrated by studying SCC dynamics as a function of various experimental parameters. We observe coherent SCC interactions between both species after an initialization quench. Furthermore, we recorded the SCC resonance as a function of this initialization quench and the offset magnetic field. We present a theoretical framewok for the building block model based on a mean field theory with a phenomenological decoherence term. Within this framework the experimental SCC measurements are excellently described, identifying our experimental system as a faithful representation of the building block.

Our results open up the possibility for extended lattice gauge theories based on multiple building blocks. These systems will allow for quantum simulation of gauge theories with the potential to address important questions in modern physics that can currently not be simulated by classical computational techniques.

Zusammenfassung

Diese Arbeit berichtet über die experimentelle Realisierung eines elementaren Bausteins für analoge Quantensimulation einer U(1) Gittereichtheorie in einem Mischungsexperiment aus zwei bosonischen Quantengasen. Experimentell wird der Baustein durch Bose-Einstein Kondensate von Lithium (^{7}Li) und Natrium (^{23}Na) realisiert, die sich in einem optischen Fallenpotential befinden. Eich - und Materiefreiheitsgrade werden in diesem System auf die internen Zustände der Atome abgebildet. Die notwendige U(1)-Eichinvarianz des Systems wird durch heteronukleare Spin-Austauschprozesse (SCC) zwischen den beiden Atomsorten realisiert.

Der Baustein stellt einen wichtigen Schritt in Richtung Quantensimulation erweiterter Gittereichtheorien dar, da er gleichzeitig einen systematischen Schutz der Eichinvarianz, das Potenzial für Skalierbarkeit und einen realistischen Ansatz für das Erreichen des Kontinuumslimit für die Eichfelder bietet.

Durch die Verwendung von SCC wird systematischer Schutz der Eichinvarianz erreicht indem die inherente Drehimpulserhaltung des Systems ausgenutzt wird. Das Kontinuumslimit für die Eichfelder wird im Rahmen des Quantenlinkmodells erreicht, indem mit Bose-Einstein Kondensaten mit hoher Atomzahl in der Größenordnung von 10^5 gearbeitet wird. Unser Baustein lässt sich zu einer ausgedehnten U(1) Gittereichtheorie erweitern indem individuelle Bausteine auf den Gitterplätzen eines optischen Gitters angeordnet und mit Raman-unterstütztem Tunneln gekoppelt werden.

Gute Durchstimmbarkeit unseres experimentellen Bausteins wird demonstriert indem die SCC-Dynamik als Funktion von verschiedenen experimentellen Parametern untersucht wird. Wir beobachten kohärente SCC-Dynamik zwischen beiden Atomsorten, nachdem wir das System mit einem Quench initialisieren. Darüber hinaus haben wir die SCC-Resonanz als Funktion dieses Quenches und des Magnetfeldes aufgnommen. Wir präsentieren eine theoretische Beschreibung unseres Bausteins, die auf einer Näherung bei großen Besetzungszahlen und einem phänomenologischen Dekohärenzterm basiert. Im Rahmen dieser Theorie lassen sich die SCC-Messungen hervorragend beschreiben. Diese Übereinstimmung identifiziert unser experimentelles System als eine getreue Repräsentation des Bausteins.

Unsere Ergebnisse eröffnen die Möglichkeit für erweiterte Gittereichtheorien, die auf mehreren Bausteinen basieren. Diese Systeme ermöglichen die Quantensimulation von Eichtheorien mit dem Potenzial, wichtige Fragen der modernen Physik zu beantworten, die derzeit mit klassischen Computertechniken nicht simuliert werden können.

Contents

Publications:

The following peer-reviewed article has been published in the framework of this thesis:

- **A scalable realization of local U(1) gauge invariance in cold atomic mixtures**
  A. Mil, T. V. Zache, A. Hegde, A. Xia, R. P. Bhatt, M.K. Oberthaler,
  P. Hauke, J. Berges, F. Jendrzejewski
  Science **367**, 1128-1130 (2020)

1. Introduction

Since the early days of ultracold quantum gases, experiments in this field have been successfully used as a platform to study various quantum many-body problems. The superfluid to Mott insulator transition [1], the crossover from a Bose-Einstein condensate to a degenerate Fermi gas [2–4] and the quantum simulation of antiferromagnetic spin chains [5] are just a few examples where cold atom experiments have been used to shed light on long standing questions of modern physics.

Closely related to these findings is the principle of analog quantum simulation, that is using a highly tailored quantum system that constitues the same properties and Hamiltonian as the specific problem one wants to study. Due to the inherent quantum properties of this quantum simulator, its capability for providing solutions to certain quantum problems surpasses the ones of classical supercomputers [6–8].

Made possible by recent advances in the experimental field of ultracold atoms [9, 10] as well as by efforts from theoretical side to provide feasible proposals [11–17], has put gauge theories into the focus of recent experimental efforts for quantum simulation, a class of physical problems that for a long time has not attracted great attention from the cold atom community.

Gauge theories play a fundamental role in the description of quantum physics and are well studied in condensed matter physics [18] as well as high energy physics [19–21]. A prominent example is quantum electrodynamics, which describes the interaction of electrons with the electromagnetic field based on a U(1) gauge symmetry. Such a symmetry leads to dynamics between matter and gauge fields that include strict symmetry constraints. This leads to phenomena like Schwinger pair-production [22–24] or string breaking due to confinement [25–27].

Lattice gauge theories provide a framework to formulate gauge theories on a discrete lattice, offering a possibility to tackle these problems with numerical models, for instance Monte Carlo techniques [28]. Nonetheless, the prediction of the out of equilibrium dynamics of these theories remains an outstanding computational challenge. This fact has sparked great effort across communities to realize quantum simulation experiments for those theories in highly controlled table-top setups.

First experimental approaches have been made among others in trapped ions. In [29] a digital quantum simulation method was used to perform time evolution of a gauge theory on a few qubits. In [30] a hybrid classical–quantum algorithm is used to determine ground state properties of a gauge theory. Rydberg atoms trapped in optical tweezers are another promising experimental platform. As demonstrated in [31] such systems can be scaled up to large one dimensional systems that can simulate Ising-type quantum spin models. As shown in [32], the dynamics of such a Rydberg system map onto the ones of a U(1) lattice gauge theory. Although reaching large system sizes, this implementation restricts the Hilbert

space of the gauge fields. Another experimental approach is based on Floquet engineering in ultracold atoms in optical lattices [33–35]. This approach led to the realization of a minimal model of a discrete Z_2 gauge theory.

In this thesis we present the experimental realization of a minimal instance of a U(1) gauge theory in our ultracold mixture experiment of sodium and lithium. We call this minimal instance a building block, as it contains all crucial gauge invariant interactions between gauge and matter field. We point out conceptionally how the extension towards a one dimensional lattice gauge theory based on repetitions of this building block is performed. The strength of our proposed model lies in the combination of systematic protection of gauge invariance, the potential for scalability and working in a regime that approaches the continuum limit of the gauge fields [36].

Experimentally, the building block is realized in a mixture of optically trapped Bose-Einstein condensates of sodium and lithium. In this system gauge field (matter field) degrees of freedom are mapped on the internal states of sodium (lithium). The essential U(1) gauge symmetry in this system is enforced due to angular momentum conservation in the atomic mixture. Accordingly the necessary gauge invariant interactions are realized by heteronuclear spin changing collisions [37, 38]. The great advantage of using spin changing collisions is that gauge invariance is systematically protected by inherent energy and symmetry constraints of the system.

The main effort of this thesis as performed by myself has been the realization and the systematic study of heteronuclear spin changing collisions in a mixture of bosonic sodium and lithium and the verification of that system to be a faithful representation of the desired building block for the proposed gauge theory. The work included the ensuring of a reliable operation of the experimental setup for generating ultracold samples, the characterization and benchmarking of the experiment's performance, the design of an experimental sequence that allows to measure a clear signature of the desired spin changing collision process, the identification of the relevant experimental parameter regimes and the acquisition and postprocessing of all experimental data presented in this work. From a theoretical point of view my effort has been the preparation and display of experimental data as well as setting up the necessary routines for analysis and comparison of measured data and the theoretical prediction based on a mean field theory. The theoretical work has been done in close collaboration with T. V. Zache, the entire work of this thesis has been supervised by F. Jendrzejewski.

The main findings of this thesis are based on the article [36]. The data analysis that was used for the current work is based on updated calibration and data treatment routines, leading to slight variation in numerical values compared to the data presented in [36].

The thesis is structured in the following way:

- In chapter 2 we introduce theoretical concepts which will be used throughout this work. This includes a short introduction on Bose-Einstein condensation and the framework of the Gross-Pitaevskii equation.

  We then continue with a general introduction of lattice gauge theories. In particular we

point out how gauge fields emerge from imposing gauge invariance onto the system and how this leads to constraints on, for instance, the dynamics of the system. We also introduce quantum link models, being the framework in which lattice gauge theories are treated in this work.

In this chapter we also derive the building block Hamiltonian from a full microscopic treatment of our ultracold atomic mixture system. We point out the important features of the building block and show how multiple building blocks can be utilized to construct an extended U(1) lattice gauge theory.

- In chapter 3 we introduce the experimental setup used to implement the building block Hamiltonian with cold atoms. Many basic parts of the experiment have been developed prior to this thesis and are well documented in previous works [39–42]. Therefore, the focus of this chapter is on the experimental methods and techniques which were designed and used for performing the measurements which are presented in this work and are not described elsewhere.

  We present the general setup and the experimental sequence that is used to prepare ultracold mixtures of sodium and lithium. We explain in detail the methods we use to characterize our experimental system including total atom number detection by absorption imaging and determination of the trapping potential by trap frequency measurements. Moreover, we explain in detail the experimental sequence for initializing and observing heteronuclear spin changing collisions. In particular we elaborate on the initial criteria to facilitate this effect and explain which experimental parameters we can tune to systematically investigate heteronuclear spin changing collisions. The chapter closes with a description of our data acquisition and processing routines that were used to generate the data presented in this work.

- In chapter 4 we compare our experimental measurements with theoretical model predictions. To this end we numerically study the dynamics that emerge from the building block Hamiltonian in the mean field limit. In order to perform this study in a physically meaningful regime we use ab initio estimates for the building block parameter based on experimental input and atomic density profiles determined by means of the Gross-Pitaevskii equation. We identify very characteristic features of the emerging dynamics as a function of evolution time, initial internal state population of sodium and magnetic offset field which are parameters that are systematically scanned in the experimenal measurements. We find that all experimental findings are excellently described by the mean field building block model with a phenomenological decoherence term and numerically determined best fitting building block parameters. We discuss the physical reasons that lead to decoherence in our setup and point out strategies to overcome them.

- In chapter 5 we summarize the main aspects of this work and point out the possibilities that have been opened up by the findings related to our building block system.

2. Theoretical concepts

In this chapter we provide theoretical concepts which are used throughout this thesis. Mainly this covers three areas.

First, a short summary on Bose-Einstein condensation and an introduction of the Gross-Pitaevskii Equation in order to introduce relations which will be used later in this work.

Second, an overview of U(1) lattice gauge theories. Main aspect will be to point out the relation between gauge invariance and the emergence of gauge fields and how this affects the structure of the theory. Furthermore, we present concrete Hamiltonian formulations of lattice gauge theories describing quantum electrodynamics. In addition the concept of quantum link models will be introduced, which is the underlying framework for the experimental implementation of lattice gauge theories in this work.

Third, a derivation of the building block Hamiltonian, which is the central subject of this thesis. We start out from a microscopic description of our cold atom system and derive the building block as an effective model. Furthermore, we show how to construct an extended lattice gauge theory based of repetitions of individual building blocks.

The first two points can be considered textbook knowledge and are included here for the sake of completeness as well as to point out the context in which some of the relations are used later on in the thesis. The third point is more novel and is partly based on the article [36] and has been mainly developed by T. V. Zache [43].

2.1. Bose-Einstein condensation and Gross-Pitaevskii Equation

The experiments that are presented in this work are performed in trapped ultracold atomic gases of the bosonic species of sodium (^{23}Na) and lithium (^{7}Li). During the experiment the gases are cooled to quantum degeneracy, which results in Bose-Einstein condensation, an effect that leads to the ground state of the trap being macroscopically populated.

Bose-Einstein condensation has been extensively coverd in literature both experimentally [44–48] and theoretically [49–52]. Therefore this section presents the main findings that are known about Bose-Einstein condensates (BECs) and describes some of the key properties that we can determine experimentally to benchmark our system, see 3.4.2. In the following we use the notation and line of reasoning of [53].

2.1.1. General considerations

In the following we consider a gas of N bosonic particles confined to a three dimensional harmonic potential

$$V(x,y,z) = \frac{1}{2}m(\omega_x^2 x^2 + \omega_y^2 y^2 + \omega_z^2 z^2) \ , \tag{2.1}$$

with $\omega_i, i \in x,y,z$ being the trapping frequency in the according spatial direction and m being the mass of the trapped species. Furthermore the introduce the geometric average trapping frequency $\bar{\omega} = (\omega_1\omega_2\omega_3)^{1/3}$. The distribution of those particles is governed by Bose-Einstein statistics

$$\bar{n}_i = \frac{1}{\exp\left(\frac{\epsilon_i - \mu}{k_\mathrm{B}T}\right) - 1} \ , \tag{2.2}$$

with $\bar{n}_i$ being the mean occupation number of ith quantum state, ϵ_i being the corresponding energy of that state, μ being the chemical potential, T being the temperature and k_B being the Boltzmann constant.

From 2.2 one can directly see some pecularities of the Bose distribution. The chemical potential is restricted to $\mu < \epsilon_0$, where ϵ_0 is the lowest energy level of the system. Otherwise one would obtain negative occupation numbers, which is an unphysical result. Furthermore we can write the total particle number as $N = N_0 + N_T$ with N_0 being the particle number occupying the ground state and N_T being the particle number in all the other (excited) states. The normalization condition $N = \sum_i \bar{n}_i$ leads to the fact that for a given temperature the amount of particles that occupy excited states is limited. This maximum $N_{T,\mathrm{max}}$ is reached in the limit of $\mu \to \epsilon_0$. When the total particle number is higher than $N_{T,\mathrm{max}}$, the rest of the particles has to go to the ground state in order to satisfy the normalization, this is the emergence of Bose-Einstein condensation. The temperature where $N = N_{T,\mathrm{max}}$ is called critical temperature T_c. In the case of the harmonic trapping potential 2.1 the critical temperature is given by [54]

$$T_\mathrm{c} = 0.94\hbar\bar{\omega}N^{1/3}/k_\mathrm{B} \ . \tag{2.3}$$

From this expression directly follows the relation between temperature T and condensate fraction $\eta_\mathrm{CF} = N_0/(N_0 + N_\mathrm{T})$

$$\eta_\mathrm{CF} = 1 - \left(\frac{T}{T_\mathrm{c}}\right)^3 \ . \tag{2.4}$$

Therefore, a measurement of the condensate fraction can be used to determine the temperature of the system.

2.1.2. Gross-Pitaevskii Equation

In most experimental cases Bose-Einstein condensates are weakly interacting (in case the experiment is performed far from a Feshbach resonance, as it is the case for our experiment). Microscopically, the interactions are based on scattering processes of individual atoms. Since typical Bose-Einstein condensates are occuring at low densities and low temperatures, the interactions are described by s-wave scattering [55], with the interaction strength

$$g = \frac{4\pi\hbar^2 a}{m} \,, \tag{2.5}$$

where a is the s-wave scattering length, and m the mass of the colliding atoms.

A profound framework to treat such interacting Bose-Einstein condensates is the Gross-Pitaevskii equation (GPE). In the following we consider the time-independent GPE [56, 57]. It is similar to the Schrödinger equation, but additionally takes into account the s-wave interaction in a mean field description by an interaction term. The stationary wave function $\Phi(\mathbf{x})$ of an interacting Bose-Einstein condensate is governed by the time-independent GPE

$$\mu\Phi(\mathbf{x}) = -\frac{\hbar^2}{2m}\nabla^2\Phi(\mathbf{x}) + V(\mathbf{x})\Phi(\mathbf{x}) + g|\Phi(\mathbf{x})|^2\Phi(\mathbf{x}) \,, \tag{2.6}$$

where μ is the chemical potential and $|\Phi(\mathbf{x})|^2 = n(\mathbf{x})$ the spatial density of the condensate. The first term on the right hand side of the equation describes the kinetic energy, the second the potential energy due to an external potential and the third one the interaction energy.

For realistic experimental parameters of Bose-Einstein condensates, the kinetic energy term can be neglected compared to the interaction energy term. This approximation is called Thomas-Fermi approximation [55]. In this regime the solution of equation 2.6 simplifies to

$$|\Phi(\mathbf{x})|^2 = n(\mathbf{x}) = \frac{\mu - V(\mathbf{x})}{g} \,. \tag{2.7}$$

The explicit solution for a harmonic trapping potential is

$$n_{\mathrm{TF}}(x,y,z) = \frac{15}{8\pi r_{\mathrm{TF,x}} r_{\mathrm{TF,y}} r_{\mathrm{TF,z}}} \left(1 - \frac{x^2}{r_{\mathrm{TF,x}}^2} - \frac{y^2}{r_{\mathrm{TF,y}}^2} - \frac{z^2}{r_{\mathrm{TF,z}}^2}\right) \,, \tag{2.8}$$

with Thomas-Fermi radii

$$r_{\mathrm{TF,i}} = \sqrt{\frac{2\mu}{m\omega_i^2}} \,, \tag{2.9}$$

and chemical potential

$$\mu = \frac{1}{2}\left(15aN\hbar^2\bar{\omega}^3\right)^{2/5} m^{1/5} \,. \tag{2.10}$$

The functional form of equation 2.8 is an inverted parabola and can be used as an experimental signature for Bose-Einstein condensation. It was shown [49, 58] that this parabolic shape not only describes the density distribution of a Bose-Einstein condensate in the trap but also the shape of the cloud after free ballistic expansion. Therefore, a Thomas-Fermi profile is seen in time of flight measurements as presented in section 3.4.2. The description of Bose-Einstein condensates via the aforementioned GPE formalism assumes $T = 0$ or in other words that all bosonic particles are condensed. In experimental systems this assumption is only partially fullfilled, as certain amount of atoms accupy the thermal phase.

In order to compare the experimental time of flight images of our clouds to a theoretical model we use a bimodal function which is fitted to the data. As a bimodal function we choose a combination that describes the atomic cloud in two limiting cases, i.e. the bimodal function contains the parabolic Thomas-Fermi profile 2.8 that is a good description in the $T = 0$ limit, and contains a gaussian profile that describes the high temperature limit [59]. By fitting time of flight absorption images to this bimodal distributions allows to determine the number of atoms in the condensed phase and the numbe of atoms in the thermal phase. Using relation 2.3 and 2.4 this gives insight into important benchmark characteristics of the experimental system, as will be shown in section 3.4.

2.2. Lattice gauge theories

Gauge theories are a fundamental concept in physics, being not only the base of theories like electrodynamics but also the standard model of particle physics [60, 61]. The basis of each gauge theory is a local gauge invariance determined by a gauge group. Quantum Electrodynamics (QED) for instance has an underlying U(1) group whereas Quantum Chromodynamics (QCD) is based on the SU(3) symmetry group. Enforcing the local gauge invariance leads to the emergence of gauge fields, which mediate the interaction between charged matter particles. This local symmetry of the system leads to strong constraints on the dynamics of gauge field and matter.

Lattice gauge theories are successful methods for studying above-mentioned theories by formulating them on discretized space. The strength of these models is the ability to treat nonperturbative problems numerically, for instance by using Monte-Carlo techniques [28]. This is especially useful in calculating out-of-equilibrium dynamics in QCD, where many regimes cannot be accessed perturbatively due to the strong coupling. In the following I will give a brief introduction to the principles of lattice gauge theory based on a U(1) gauge group in one dimensional space. For further reading and a comprehensive treatment of the topic I recommend [62–65]. Dedicated work to lattice gauge theories for implementation in cold atom systems is found in [13, 16, 17].

For theoretical derivations regarding lattice gauge theories we use the units $\hbar = c = 1$.

Whenever we treat real systems or parameters related to experimental implementation we use the proper SI units.

2.2.1. Introducing general concepts of lattice gauge theories

Let us consider a matter field on a one dimensional lattice represented by field operators $\psi_n^\dagger$ and ψ_n, where n denotes the lattice sites. The Hamiltonian describing a free moving matter particle is given by:

$$H = \sum_n m_n \psi_n^\dagger \psi_n + J \sum_n (\psi_{n+1}^\dagger \psi_n + h.c), \tag{2.11}$$

with m_n being the mass and J being the hopping element of the nearest-neighbour hopping term. We further introduce the unitary gauge transformation

$$\psi_n \longrightarrow V_n \psi_n \quad ; \quad \psi_n^\dagger \longrightarrow \psi_n^\dagger V_n, \tag{2.12}$$

with V_n being an element of the gauge group $\mathcal{G}$. In the following we will treat the group $\mathcal{G} = U(1)$ as found in QED. U(1) is the group of elements on the unit circle in the complex plane. It is a continous symmetry group as rotations in the complex plane can be done in contious fashion. In this case the gauge transformation can explicitly be written as:

$$V_n = \exp\left(i \sum_n \alpha_n G_n\right), \tag{2.13}$$

with α_n being the local phase and G_n being the Generator of transformation. It is important to note that the gauge transformation is strictly local, i.e. the phase factor is changed on each lattice site n independently. In other words, the effect of the transformation by V_n is multipying a phase factor $\propto \exp(i\alpha_n)$ to each lattice site. The important point is that this phase factor is not the same for all lattice sites but individually depending on n. In a descriptive picture one can imagine the discretized space, and the effect of this transformation is going to each single lattice point and perform a local rotation at this point that is independent of the neighbouring lattice sites.

A theory is said to be a gauge theory if the gauge transformation leaves it invariant. One can see that this is not the case for Hamiltonian 2.11 assuming local gauge invariance (it is invariant under a global gauge transformation though), as the hopping term is varied under the transformation

$$\psi_{n+1}^\dagger \psi_n \longrightarrow \psi_{n+1}^\dagger V_{n+1}^\dagger V_n \psi_n \tag{2.14}$$

for the case of nonconstant arbitrarily chosen $\alpha_n \neq \alpha_{n+1}$.

However, the local gauge invariance can be restored by introducing so called gauge links U_n which are located inbetween lattice sites and connect two matter fields, see Fig. 2.1. The

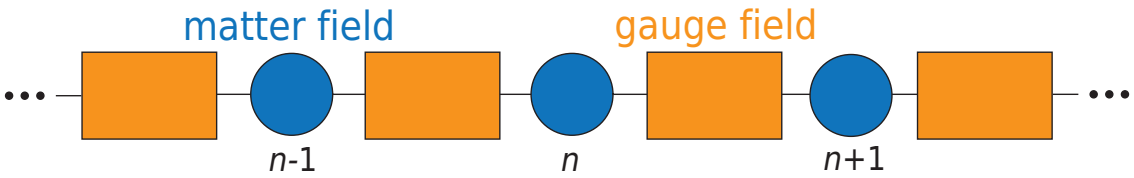

Figure 2.1.: **Structure of a lattice gauge theory.** Matter fields reside on sites represented by circles. Gauge fields connecting two neighbouring matter sites are located inbetween, represented by rectangles.

links are elements of the gauge group and transform in the following way:

$$U_n \longrightarrow V_{n+1} U_n V_n^\dagger \tag{2.15}$$

Note that we used the definition $U_n = U_{n,n+1}$ here, where the two indices label the position of the two matter sites which are connected by the link. Note that the link is strictly defined as the connector between two matter sites and not as a standalone object [66]. Furthermore, the link operators obey the following commutation relation:

$$\left[U_n, U_m^\dagger\right] = 0 \tag{2.16}$$

With the link added, the hopping term transforms as

$$\psi_{n+1}^\dagger U_n \psi_n \longrightarrow \psi_{n+1}^\dagger V_{n+1}^\dagger V_{n+1} U_n V_n^\dagger V_n \psi_n = \psi_{n+1}^\dagger U_n \psi_n \ . \tag{2.17}$$

and Hamiltonian 2.11 becomes gauge invariant:

$$H \longrightarrow V H V^\dagger = H \tag{2.18}$$

Which is equivalent to the commutation relation

$$[G_n, H] = 0 \ . \tag{2.19}$$

Relation 2.18 is achieved with the generator

$$G_n = E_{n+1} - E_n - e\psi_n^\dagger \psi_n \ , \tag{2.20}$$

with e being the unit charge which is carried by the matter field and E_n being the conjugate field of the gauge link fullfilling the commutation relations

$$\begin{aligned} [E_n, U_m] &= \delta_{n,m} U_m e \\ \left[E_n, U_m^\dagger\right] &= -\delta_{n,m} U_m^\dagger e \ . \end{aligned} \tag{2.21}$$

From equation 2.19 follows that the eigenvalues g_n of G_n are conserved quantities

$$G_n |\psi\rangle = g_n |\psi\rangle . \tag{2.22}$$

Therefore the full Hilbert space is decomposed into sectors associated with different eigenvalues g_n and gauge invariant dynamics do not mix between those sectors. We further impose that the physical part of the Hilbert space is gauge invariant as well

$$V_n |\psi_{\text{phys}}\rangle = |\psi_{\text{phys}}\rangle , \tag{2.23}$$

from which follows:

$$G_n |\psi_{\text{phys}}\rangle = 0 \tag{2.24}$$

$$(E_{n+1} - E_n) |\psi_{\text{phys}}\rangle = g_n |\psi_{\text{phys}}\rangle \tag{2.25}$$

Last expression is the lattice version of Gauss' law $\nabla E = \rho$.

The physical interpretation of above derivations is the following: Demanding gauge invariance on the theory of free matter fields gives rise to gauge fields. These gauge fields which were introduced as auxiliary fields to restore gauge invariance lead to new physical constraints in the theory. One consequence is that matter particles carry charges which interact with the conjugate field of the gauge fields, the electric field. The hopping term in 2.11 is modified such that gauge and matter field interact in a correlated way which respects Gauss' law i.e. a particle hopping from one site to another is always accompanied with changing electric fields on the neighbouring links, see Fig. 2.2. In this correlated hopping process U_n and $U_n^\dagger$ can be inteprated as the operators that raise and lower the value of E_n. In addition gauge fields have dynamics of their own. In analogy to real space momentum describing kinetic energy of moving mass the conjugate momentum of the gauge link represents the energy stored in the gauge field and therefore the dynamic part of the gauge field is

$$H_{\text{gauge}} \propto E_n^2 \ . \tag{2.26}$$

Note that in dimensions higher than one an additional contribution of the magnetic field to the gauge field energy will arise.

2.2.2. Lattice formulation of quantum electrodynamics

In the previous section we pointed out general structures of lattice gauge theories based on a U(1) gauge symmetry in one dimension. Main idea was to point out that imposing gauge invariance leads to constraints on the resulting dynamics of the system, which in that case manifests in the emergence of the correlated hopping term 2.17.

In the following section we will show concrete examples of lattice gauge theories in Hamilton formulation for quantum electrodynamics. In the following the presentation will be less didactical as the previous section and we will only present main findings. Comprehensive information on this topic is found in [12, 13, 16, 17, 62–65].

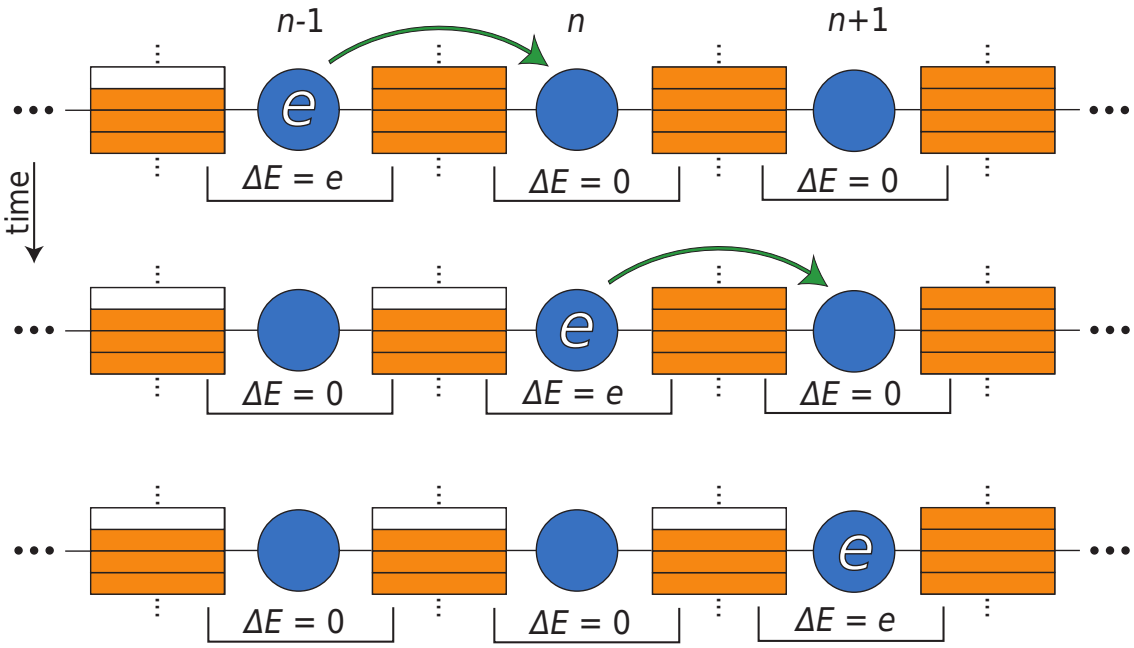

Figure 2.2.: **Illustration of correlated hopping.** Analog to Fig. 2.1 blue circles represent matter sites. The sectioned rectangles represent the electric field which is the canonic conjugate field of the gauge field. A matter particle represented by e is moving along the lattice. The rows depict three instances in time when the particle has hopped one site further. Gauge invariant dynamics respect Gauss' law, therefore at each site n the relation $E_{n+1} - E_n \equiv \Delta E = e$ must hold. This leads to correlated hopping, where each hopping of the matter particle is linked to a change of the electric field by one quantum, illustrated by the blanking of one unit of the rectangles.

A Hamilton formulation of quantum electrodynamics in one dimension on a lattice is given by

$$H_{KS} = \frac{a}{2}\sum_n E_n^2 + m\sum_n (-1)^n \psi_n^\dagger \psi_n - \frac{i}{2a}\sum_n (\psi_{n+1}^\dagger U_n \psi_n - h.c) \ , \tag{2.27}$$

where matter particles are electrons following fermionic commutation relations

$$\left\{\psi_m, \psi_n^\dagger\right\} = \delta_{m,n} \ , \tag{2.28}$$

and a is the lattice spacing of the discretized real space lattice .

This is the well established Kogut-Susskind Hamiltonian [62, 66]. It is employing the so called staggered fermion discretization to deal with the fermion doubling problem which is the appearence of redundant fermionic states due to the discretizing procedure when making the transition from continuous real space to a lattice [67]. In this formulation the matter sites are staggered, such that even lattice sites represent "particles" with positive mass and odd sites

"holes" with negative mass. The odd sites are interpreted as the Dirac sea. Occupation of an odd site corresponds to a filled Dirac sea i.e. vacuum, whereas a vacant odd site corresponds to an antiparticle. The charge operator takes the form

$$\frac{q_n}{e} = \psi_n^\dagger \psi_n + \frac{(-1)^n - 1}{2} \ . \tag{2.29}$$

However, the staggered formulation is not unique for discretizing fermionic fields. Another way to implement the discretization is using Wilson fermions [68]. It turns out that this method is advantageous for an experimental implementation with cold atoms [17], as will be shown in section 2.4.4. When using Wilson Fermions, the matter field operators are two component spinors:

$$\psi_n = \begin{pmatrix} \psi_{n,1} \\ \psi_{n,2} \end{pmatrix} \tag{2.30}$$

In this case the generator of gauge transformations contains a sum over both spinor components:

$$G_n = E_{n+1} - E_n - e \sum_{i=1,2} \psi_{n,i}^\dagger \psi_{n,i} \tag{2.31}$$

Using this approach one can write down the lattice QED Hamiltonian analogously to 2.27:

$$H_W = \frac{a}{2} \sum_n E_n^2 + \left(m + \frac{1}{a} \right) \sum_n \psi_n^\dagger \begin{pmatrix} 0 & 1 \\ 1 & 0 \end{pmatrix} \psi_n + \frac{1}{a} \sum_n \psi_n^\dagger \begin{pmatrix} 0 & 1 \\ 0 & 0 \end{pmatrix} U_n \psi_{n+1} + h.c. \tag{2.32}$$

As one can see this formulation differs to some degree from the Kogut-Susskind Hamiltonian, yet the fundamental constraint that hopping of matter particles form one site to the other is correlated with altering the gauge fields.

The goal of introducing the formulations 2.27 and 2.32 is to highlight the general structure of lattice gauge theories and point out the necessary ingredients. On the Hamiltonian level this includes degrees of freedom for gauge and matter fields as well as the gauge invariant interaction between both.

2.3. Quantum link model

To implement lattice gauge theories with ultracold atoms one has to properly map the structure of the theory onto the experimental system. An inevitable problem that any experimental implementation will face is that relations 2.16 and 2.21 are defined on an infinite dimensional Hilbert space. Since an infinite amount of degrees of freedom cannot be realized experimentally, a cutoff on the link's Hilbert space dimensionality will always be introduced in real systems.

A formal description on how this cutoff can be introduced in a controlled way is given

by the so called quantum link model (QLM) [69]. The QLM for a U(1) lattice gauge theory employs a substitution of the gauge link degrees of freedom by angular momentum operators [15–17, 66]:

$$E_n \longrightarrow eL_{z,n} \tag{2.33}$$
$$U_n \longrightarrow [l(l+1)]^{-1/2} L_{+,n} \tag{2.34}$$
$$U_n^\dagger \longrightarrow [l(l+1)]^{-1/2} L_{-,n} \ . \tag{2.35}$$

Here, l is the magnitude of the angular momentum vector $\vec{L}$, the components L_i of the angular momentum operator fulfill the commutation relation

$$[L_i, L_j] = i\epsilon_{ijk} L_k \ , \tag{2.36}$$

with $i, j, k \in \{x, y, z\}$. Furthermore the angular momentum raising and lowering operators L_+ and L_- are defined as

$$\begin{aligned} L_+ &= L_x + iL_y \\ L_- &= L_x - iL_y \ . \end{aligned} \tag{2.37}$$

This substitution of parameters preserves the gauge invariance as well as the commutator relation 2.21. However, the link's Hilbert space is now finite dimensional with l determining the largest value for the electric field representation. As a consequence, relation 2.16 is replaced in QLM by

$$\left[U_n, U_m^\dagger\right] = \frac{2\delta_{n,m} E_m}{[l(l+1)]} \ , \tag{2.38}$$

which reaches the value of the original relation 2.16 only in the limit of large l. However, already for small values of l QLMs provide insights into genuine features of gauge theories [70]. Furthermore, the full theory is recovered in the limit of large angular momentum ($l \to \infty$), a regime which is approached in our experimental setup, where l is in the order of 10^4 to 10^5.

Besides providing a formal description for the finite size Hilbert space of the link, QLMs offer a descriptive interpretation of the gauge link. By introducing the well established SU(2) algebra the link degrees of freedom can now be described with the Bloch sphere picture [71], see Fig. 2.3. Now, inbetween two matter sites an angular momentum vector $\vec{L}_n$ is located, which is represented on the bloch sphere. The magnitude of the electric field is easily read off as the z-projection of $\vec{L}_n$. The correlated hopping of matter particles is associated with the raising and lowering operators $L_{+,n}$ and $L_{-,n}$ which increase or decrease $L_{z,n}$ by one quantum.

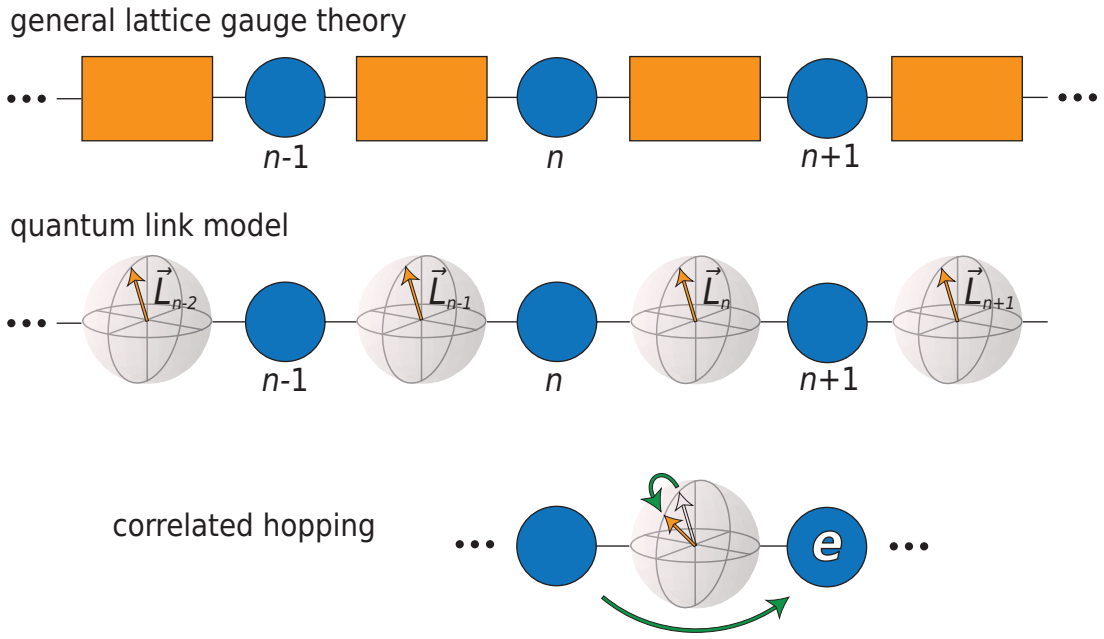

Figure 2.3.: **Illustration of quantum link models.** Two neighbouring matter sites are connected by an angular momentum vector (depicted by Bloch spheres). Main difference compared to regular lattice gauge theory is that now the gauge degrees of freedom have a finite dimensional Hilbert space determined by the vector's magnitude l. The hopping of matter particles (indicated by e) is now correlated with a raising/lowering operation on the angular momentum vector.

In the QLM formalism Hamiltonian 2.32 is replaced by:

$$\begin{aligned} H_{WQLM} =& \frac{a}{2}\sum_n L_{z,n}^2 \\ &+ \left(m + \frac{1}{a}\right)\sum_n \psi_n^\dagger \begin{pmatrix} 0 & 1 \\ 1 & 0 \end{pmatrix} \psi_n \\ &+ \frac{1}{a\sqrt{l(l+1)}}\sum_n \psi_n^\dagger \begin{pmatrix} 0 & 1 \\ 0 & 0 \end{pmatrix} L_{+,n}\psi_{n+1} + h.c. \ . \end{aligned} \tag{2.39}$$

Inspired by this Hamiltonian we developed a proposal for an implementation of a U(1) gauge theory in an ultracold atoms experiment [36]. Central point of this implementation is the building block, which is a fundamental unit of the gauge theory containing all necessary gauge invariant interactions. In the following sections we derive the building block from the microscopic description of our experimental system.

2.4. Derivation of the building block from microscopic description of the ultracold mixture

In this section we present the derivation of the building block. We start out from the microscopic description of the experimental cold atom system that is bosonic sodium ^{23}Na and lithium ^{7}Li that are trapped in a single optical dipole trap and interact via s-wave scattering. By taking into account all microscopic interactions in the mixture, using a spin representation for the internal state population of the species and exploiting conserved quantities in the system one can recast the full microscopic Hamiltonian into an effective spin model – the building block– which is described by three model parameters.

In the framework of quantum link models this building block is interpreted as a minimal gauge theory including degrees of freedom for the gauge and matter field as well as fulfilling gauge invariant interactions. Furthermore, we show how repetitions of the building block can be used to construct an extended U(1) lattice gauge theory. Conceptionally, this section links the physical disciplines of cold atoms and gauge theories by providing the information how the experimental system maps onto the physical system that is to be quantum simulated. The derivation presented is mainly based on [17, 36].

2.4.1. Microscopic cold atom Hamiltonian

Detailed description about the exact experimental system is provided in section 3.5. In general we have sodium and lithium atoms that are externally trapped. Both species are prepared in the hyperfine groundstate with total spin $F = 1$. Within this manifold we consider the two internal spin states with the magnetic quantum number $m_F = \{0, 1\}$. In section3.5 it is shown that for our specifically chosen experimental parameters the $m_F = -1$ state is not populated throughout the entire experiment and is therefore disregarded. In the following we use the indices N (sodium) and L (lithium) as a label for the species. For internal state labelling we use the value of the m_F state as indices, i.e. 1 and 0. The Hamiltonian of the this combined system is written in terms of a free part and an interaction part

$$H = \underbrace{H_{\mathrm{N}} + H_{\mathrm{L}}}_{\text{free}} + \underbrace{H_{\mathrm{NN}} + H_{\mathrm{LL}} + H_{\mathrm{NL}} + H_{\mathrm{SCC}}}_{\text{interaction}} \ . \tag{2.40}$$

The free parts contain the contribution of kinetic energy, potential energy from the confining trap and the energy in the presence of a magnetic field

$$H_s = \int_{\mathbf{x}} \sum_{\alpha} \hat{\psi}^{\dagger}_{s,\alpha}(\mathbf{x}) \left[\frac{-\nabla^2_{\mathbf{x}}}{2m_s} + V_s(\mathbf{x}) + E_{s,\alpha}(B_0) \right] \hat{\psi}_{s,\alpha}(\mathbf{x}) \ , \tag{2.41}$$

where s $\in \{\mathrm{N}, \mathrm{L}\}$, m_s denotes the atomic masses and V_s is the trapping potential (we assume the trapping potential to be the same for the two magnetic substates). $E_{s,\alpha}(B_0)$ is the Zeeman shift in the presence of an external magnetic field B_0 and it can be calculated from the

Breit-Rabi formula. The field operators $\hat{\psi}_{s,\alpha}(\mathbf{x})$ fulfill canonical commutation relations

$$\left[\hat{\psi}_{s,\alpha}(\mathbf{x}), \hat{\psi}^{\dagger}_{s',\beta}(\mathbf{y})\right] = \delta_{ss'}\delta_{\alpha\beta}\delta\left(\mathbf{x}-\mathbf{y}\right) \ , \tag{2.42}$$

with $\alpha, \beta \in \{0, 1\}$.

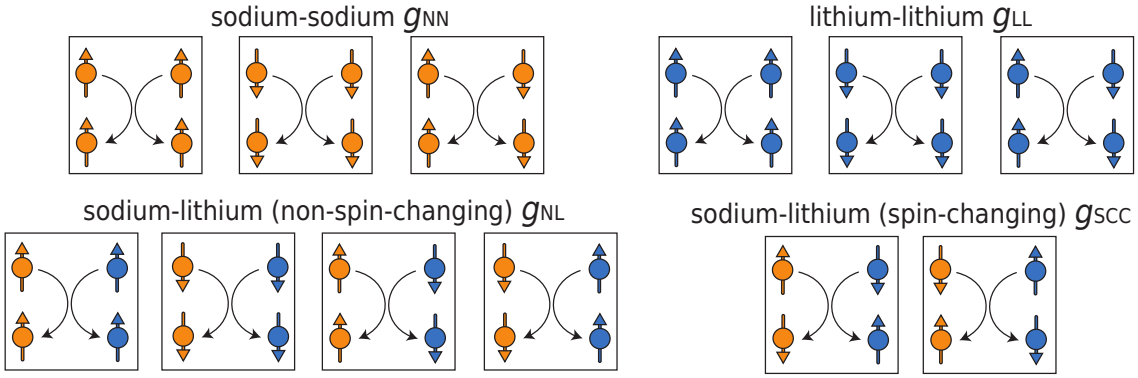

Figure 2.4.: **Illustration of the two-body scattering processes appearing in the interaction Hamiltonian.** Having two species with two internal spin states each, leads to 11 permutations. Sodium atoms are displayed in orange, lithium atoms in blue. Upwards pointing arrows represent atoms with $m_F = 0$, downwards pointing arrows represent atoms with $m_F = 1$. The two upper particles denote the configuration before the collision, the lower particles denote the configuration after the collision.

The interactions within the BEC mixture arise almost entirely from two-body collisions which can be treated within the framework of quantum scattering theory in the low energy limit (s-wave scattering) [72]. Following [37, 38] we decompose the interaction potential (which contains density and spin dependent contributions) such that the Hamiltonian is grouped in terms of two-particle scattering processes, see Fig. 2.4. We distinguish between intra-species and interspecies interactions. The intra-species Hamiltonian takes the form

$$H_s = \frac{1}{2}\int_{\mathbf{x}} \left[g^s_{11}\hat{\psi}^{\dagger}_{s,1}\hat{\psi}^{\dagger}_{s,1}\hat{\psi}_{s,1}\hat{\psi}_{s,1} + g^s_{00}\hat{\psi}^{\dagger}_{s,0}\hat{\psi}^{\dagger}_{s,0}\hat{\psi}_{s,0}\hat{\psi}_{s,0} + 2g^s_{10}\hat{\psi}^{\dagger}_{s,1}\hat{\psi}^{\dagger}_{s,0}\hat{\psi}_{s,1}\hat{\psi}_{s,0}\right] \ , \tag{2.43}$$

with

$$g^s_{jj} = \frac{4\pi\hbar^2}{m_s}a^s_{jj} \tag{2.44}$$

being the interaction strength parameter, m_s being the atomic mass of the species and a^s_{jj} being the reduced scattering lengths for homonuclear scattering with $j \in \{0, 1\}$.

The interspecies Hamiltonian again is separated into two parts. First a part H_{NL} that describes all heteronuclear scattering processes whereby the initial m_F of a single atom is not changed after scattering (non-spin-changing). Secondly a part H_{SCC} which describes

species	red. scattering length	value $[a_B]$
sodium	$a_{11}^N = a_{10}^N$	55
	a_{00}^N	53
lithium	$a_{11}^L = a_{10}^L$	12.5
	a_{00}^L	6.8
sodium/lithium	a_{11}^{NL}	20
	$a_{00}^{NL} = a_{10}^{\mathrm{NL}}$	19.65
	a_{SCC}	0.35

Table 2.1.: **Summary of the reduced scattering lengths.** The reduced scattering lengths are linear combinations of the scattering lengths a_0 and a_2, see [38]. The numerical values for the intraspecies scattering lenghts are taken from [38], the values for the interspecies scattering lengths are from (Eberhart Tiemann, personal communication).

the scattering process whereby the inital m_F of both atoms changes such that total angular momentum is conserved (spin-changing). The non-spin-changing part has the form

$$H_{NL} = \int_{\mathbf{x}} \Big[g_{11}^{NL} \hat{\psi}_{N,1}^\dagger \hat{\psi}_{N,1} \hat{\psi}_{L,1}^\dagger \hat{\psi}_{L,1} + g_{00}^{NL} \hat{\psi}_{N,0}^\dagger \hat{\psi}_{N,0} \hat{\psi}_{L,0}^\dagger \hat{\psi}_{L,0} + g_{10}^{NL} \hat{\psi}_{N,1}^\dagger \hat{\psi}_{N,1} \hat{\psi}_{L,0}^\dagger \hat{\psi}_{L,0} + g_{10}^{NL} \hat{\psi}_{N,0}^\dagger \hat{\psi}_{N,0} \hat{\psi}_{L,1}^\dagger \hat{\psi}_{L,1} \Big] , \tag{2.45}$$

with

$$g_{jj}^{NL} = \frac{2\pi\hbar^2}{\mu} a_{jj}^{NL} . \tag{2.46}$$

Here, μ is the reduced mass of both species and a_{jj}^{NL} are the reduced scattering lengths for non-spin-changing heteronuclear scattering with $j \in \{0, 1\}$. Finally, the spin changing collision part of the interaction Hamiltonian is

$$H_{\mathrm{SCC}} = g^{\mathrm{SCC}} \int_{\mathbf{x}} \left[\hat{\psi}_{N,0}^\dagger \hat{\psi}_{L,1}^\dagger \hat{\psi}_{N,1} \hat{\psi}_{L,0} + \hat{\psi}_{N,1}^\dagger \hat{\psi}_{L,0}^\dagger \hat{\psi}_{N,0} \hat{\psi}_{L,1} \right] , \tag{2.47}$$

with

$$g^{\mathrm{SCC}} = \frac{2\pi\hbar^2}{\mu} a_{\mathrm{SCC}} , \tag{2.48}$$

where a_{SCC} is the reduced scattering length of the spin-changing-collisions. The numerical values for the reduced scattering lengths can be found in Tab. 2.1.

2.4.2. Spin and density decomposition of the system Hamiltonian

In the previous section we have derived the microscopical Hamiltonian of our experimental system, which included the free part of each species as well as the interaction part arising from two body collisions of atoms. On our way to establish a connection between this Hamiltonian and the Hamiltonian of gauge theories we perform a number of steps. Since we are interested in the spin dynamics of the system we will separate the interactions in the system into spin and density dependent parts.

As a first step we assume the spatial dynamics to be frozen out, which is a reasonable assumption for atoms confined in tight traps (a discussion regarding the validity of this approximation is found in section 4.2.4). Formally this is done by a single mode approximation (SMA) whereby the field operators are approximated as

$$\hat{\psi}_{s,\alpha}(\mathbf{x}) \approx \Phi_{s,a}(\mathbf{x})\hat{b}_{s,\alpha} \ , \tag{2.49}$$

with the single mode $\Phi_{s,a}(\mathbf{x})$ being an appropriately chosen wavefunction (which can be determined from the ground state of the Gross-Pitaevskii equation 2.6), and $\hat{b}_{s,\alpha}, \hat{b}^\dagger_{s,\alpha}$ being the annihilation and creation operators for the single mode, hence $\hat{N}_{s,\alpha} = \hat{b}^\dagger_{s,\alpha}\hat{b}_{s,\alpha}$ is the number operator for given species and magnetic substate. In the SMA the total Hamiltonian is

$$\begin{aligned}
H_{\mathrm{SMA}} &= h^{\mathrm{SMA}}_{\mathrm{N}} + h^{\mathrm{SMA}}_{\mathrm{L}} + h^{\mathrm{SMA}}_{\mathrm{NN}} + h^{\mathrm{SMA}}_{\mathrm{LL}} + h^{\mathrm{SMA}}_{\mathrm{NL}} + h^{\mathrm{SMA}}_{\mathrm{SCC}} \\
&= \sum_s \left[\tilde{E}_{s,1}(B_0)\hat{b}^\dagger_{s,1}\hat{b}_{s,1} + \tilde{E}_{s,0}(B_0)\hat{b}^\dagger_{s,0}\hat{b}_{s,0}\right] \\
&+ \sum_s \left[X^s_{11}\hat{b}^\dagger_{s,1}\hat{b}^\dagger_{s,1}\hat{b}_{s,1}\hat{b}_{s,1} + X^s_{00}\hat{b}^\dagger_{s,0}\hat{b}^\dagger_{s,0}\hat{b}_{s,0}\hat{b}_{s,0} + 2X^s_{10}\hat{b}^\dagger_{s,1}\hat{b}^\dagger_{s,0}\hat{b}_{s,1}\hat{b}_{s,0}\right] \\
&+ X^{NL}_{11}\hat{b}^\dagger_{N,1}\hat{b}_{N,1}\hat{b}^\dagger_{L,1}\hat{b}_{L,1} + X^{NL}_{00}\hat{b}^\dagger_{N,0}\hat{b}_{N,0}\hat{b}^\dagger_{L,0}\hat{b}_{L,0} + X^{NL}_{10}\hat{b}^\dagger_{N,1}\hat{b}_{N,1}\hat{b}^\dagger_{L,0}\hat{b}_{L,0} + X^{NL}_{10}\hat{b}^\dagger_{N,0}\hat{b}_{N,0}\hat{b}^\dagger_{L,1}\hat{b}_{L,1} \\
&+ X^{\mathrm{SCC}}\hat{b}^\dagger_{N,0}\hat{b}^\dagger_{L,1}\hat{b}_{N,1}\hat{b}_{L,0} + X^{\mathrm{SCC}}\hat{b}^\dagger_{N,1}\hat{b}^\dagger_{L,0}\hat{b}_{N,0}\hat{b}_{L,1} \ ,
\end{aligned} \tag{2.50}$$

with the modified energy levels

$$\tilde{E}_{s,\alpha}(B_0) = E_{s,\alpha}(B_0) + \int_{\mathbf{x}} \Phi^*_{s,\alpha}(\mathbf{x}) \left[\frac{-\nabla^2_{\mathbf{x}}}{2m_s} + V_s(\mathbf{x})\right] \Phi_{s,\alpha}(\mathbf{x}) \ , \tag{2.51}$$

and the reduced interaction constants

$$X^s_{\alpha\beta} = \frac{g^s_{\alpha\beta}}{2} \int_{\mathbf{x}} |\Phi_{s,\alpha}(\mathbf{x})|^2 |\Phi_{s,\beta}(\mathbf{x})|^2 \ , \tag{2.52}$$

$$X^{NL}_{\alpha\beta} = g^{NL}_{\alpha\beta} \int_{\mathbf{x}} \Phi^*_{N,1}\Phi^*_{L,1}\Phi_{N,0}\Phi_{L,0} \ , \tag{2.53}$$

$$X^{SCC} = g^{SCC} \int_{\mathbf{x}} \Phi^*_{N,1}\Phi^*_{L,1}\Phi_{N,0}\Phi_{L,0} \ . \tag{2.54}$$

Having integrated out all spatial degrees of freedom we want to focus on the spin dynamics of the system. First we introduce spin operators using the Schwinger boson representation

$$\hat{L}_{z,s} = \frac{1}{2}\left(\hat{N}_{s,1} - \hat{N}_{s,0}\right),\ \hat{L}_{+,s} = \hat{b}^{\dagger}_{s,1}\hat{b}_{s,0},\ \hat{L}_{-,s} = \hat{b}^{\dagger}_{s,0}\hat{b}_{s,1}\ . \tag{2.55}$$

We further want to exploit conserved quantities of the system. Since we are dealing with a closed system where no atoms can leak to other states, the total number of atoms of each species is conserved

$$\begin{aligned} \hat{N}_N &= \hat{N}_{N,1} + \hat{N}_{N,0} = const. \\ \hat{N}_L &= \hat{N}_{L,1} + \hat{N}_{L,0} = const. \end{aligned} \tag{2.56}$$

We use the introduced notation in 2.56 and 2.55 to separate the system Hamiltonian into parts that contain spin operators and parts that contain number operators. This composition will allow us to simplify the Hamiltonian later on as we will be able to drop terms which are conserved quantities, since those do not contribute to dynamics in the system. Applying this separation to the free Hamiltonian part yields

$$\begin{aligned} h_s^{\mathrm{SMA}} &= \tilde{E}_{s,1}(B_0)\hat{N}_{s,1} + \tilde{E}_{s,0}(B_0)\hat{N}_{s,0} \\ &= \hat{N}_s\left(\frac{\tilde{E}_{s,1}(B_0) + \tilde{E}_{s,0}(B_0)}{2}\right) + \hat{L}_{z,s}\left(\tilde{E}_{s,1}(B_0) - \tilde{E}_{s,0}(B_0)\right)\ . \end{aligned} \tag{2.57}$$

Next we proceed in the same way with the interaction Hamiltonian part. Note that by moving form the normal ordered creation and annihilation operators to number operators we have to apply the bosonic commutation relations, i.e. $\hat{b}^{\dagger}_{s,1}\hat{b}^{\dagger}_{s,1}\hat{b}_{s,1}\hat{b}_{s,1} = \hat{N}_{s,1}(\hat{N}_{s,1} - 1)$. Furthermore it turns out that in the resulting representation the reduced interaction strengths always appear as linear combinations. This motivates the definitions (following the notation in [73])

$$\chi_s = X^s_{11} - X^s_{00} \tag{2.58}$$

$$\chi_{NL} = X^{NL}_{11} - X^{NL}_{00}\ . \tag{2.59}$$

Eventually we get for the intra-species Hamiltonian

$$\begin{aligned} h_{ss}^{\mathrm{SMA}} &= X^s_{11}\hat{N}_{s,1}(\hat{N}_{s,1} - 1) + X^s_{00}\hat{N}_{s,0}(\hat{N}_{s,0} - 1) + 2X^s_{10}\hat{N}_{s,0}\hat{N}_{s,1} \\ &= \chi_s(\hat{N}_s - 1)\hat{L}_{z,s} - \chi_s\hat{L}^2_{z,s} \\ &\quad + \left[X^s_{11} + X^s_{00} + 2X^s_{10}\right]\frac{\hat{N}_s^2}{4} - \left[X^s_{11} + X^s_{00}\right]\frac{\hat{N}_s}{2}\ . \end{aligned} \tag{2.60}$$

In similar fashion we get for the interspecies Hamiltonian

$$\begin{aligned} h_{\mathrm{NL}}^{\mathrm{SMA}} &= (X_{11}^{NL}\hat{N}_{N,1} + X_{00}^{NL}\hat{N}_{N,0})\hat{N}_{L,1} + X_{00}^{NL}(\hat{N}_{N,1} + \hat{N}_{N,0})\hat{N}_{L,0} \\ &= \frac{\chi_{NL}}{2}\hat{N}_N\hat{L}_{z,L} + \frac{\chi_{NL}}{2}\hat{N}_L\hat{L}_{z,N} + \chi_{NL}\hat{L}_{z,N}\hat{L}_{z,L} \\ &+ \frac{(X_{11}^{NL} + 3X_{00}^{NL})}{4}\hat{N}_N\hat{N}_L \ , \end{aligned} \tag{2.61}$$

and for the SCC Hamiltonian

$$h^{\mathrm{SCC}} = X^{\mathrm{SCC}}\left[\hat{b}_{L,1}^{\dagger}\hat{L}_{-,N}\hat{b}_{L,0} + \hat{b}_{L,0}^{\dagger}\hat{L}_{+,N}\hat{b}_{L,1}\right] . \tag{2.62}$$

2.4.3. Effective model of the microscopic system – the building block

In the previous section we decomposed the Hamiltonian into parts that are proportional to spin operators and number operators, respectively. As the number dynamics is frozen out by the local conservation laws for no kinetic energy we fully focus on the spin degrees of freedom and drop all terms in the Hamiltonian which only contain number operators of conserved quantities.

Finally we arrive at the full spin Hamiltonian by putting all terms together

$$\begin{aligned} H_{\mathrm{SMA}}^{\mathrm{spin}} &= \left[\big(E_{N,1}(B_0) - E_{N,0}(B_0)\big) + \chi_N(\hat{N}_N - 1) + \frac{1}{2}\chi_{NL}\hat{N}_L\right]\hat{L}_{z,N} - \chi_N\hat{L}_{z,N}^2 \\ &+ \left[\big(E_{L,1}(B_0) - E_{L,0}(B_0)\big) + \chi_L(\hat{N}_L - 1) + \frac{1}{2}\chi_{NL}\hat{N}_N\right]\hat{L}_{z,L} - \chi_L\hat{L}_{z,L}^2 \\ &+ \chi_{NL}\hat{L}_{z,N}\hat{L}_{z,L} + h_{\mathrm{SCC}} \ . \end{aligned} \tag{2.63}$$

We define the total magnetization as $M = \hat{L}_{z,N} + \hat{L}_{z,L}$, which is a conserved quantitiy. The reason for the total magnetization being the conserved quantitiy instead of the magnetization of each species is the SCC process. It allows for the spin state of a single species to change during a collisional process. In order to fulfill angular momentum conservation such a spin change in one species is always correlated with an opposite spin change in the other species (compare Fig. 2.4). We use the definition of M to rewrite 2.63 such that we are only left with spin operators that scale linearly with $\hat{L}_{z,L}$ and quadratic with $\hat{L}_{z,N}$. Hence we get

$$\begin{aligned} H_{\mathrm{BB}}/\hbar &= \chi\hat{L}_{z,N}^2 + \Delta\hat{L}_{z,L} + \lambda\left(\hat{L}_{-,N}\hat{L}_{+,L} + \hat{L}_{+,N}\hat{L}_{-,L}\right) \\ &= \chi\hat{L}_{z,N}^2 + \frac{\Delta}{2}\left(\hat{b}_{L,1}^{\dagger}\hat{b}_{L,1} - \hat{b}_{L,0}^{\dagger}\hat{b}_{L,0}\right) + \lambda\left(\hat{b}_{L,1}^{\dagger}\hat{L}_{-,N}\hat{b}_{L,0} + \hat{b}_{L,0}^{\dagger}\hat{L}_{+,N}\hat{b}_{L,1}\right) \ , \end{aligned} \tag{2.64}$$

with the parameters λ, χ and Δ defined as

$$\lambda = X^{\mathrm{SCC}} \tag{2.65}$$

$$\chi = -\chi_N - \chi_L - \chi_{NL} \tag{2.66}$$

$$\begin{aligned}\Delta = &\left(E_{L,1}(B_0) - E_{L,0}(B_0)\right) - \left(E_{N,1}(B_0) - E_{N,0}(B_0)\right) \\ &+ \chi_L(\hat{N}_L - 1) - \chi_N(\hat{N}_N - 1) + \frac{1}{2}\chi_{NL}(\hat{N}_N - \hat{N}_L) + 2M\left(-\chi_L - \frac{1}{2}\chi_{NL}\right) .\end{aligned} \tag{2.67}$$

Hamiltonian 2.64 has an equivalent form when instead of using the representation in 2.55 we use

$$\hat{L}_{z,s} = \frac{1}{2}\left(\hat{N}_{s,0} - \hat{N}_{s,1}\right),\ \hat{L}_{+,s} = \hat{b}^\dagger_{s,0}\hat{b}_{s,1},\ \hat{L}_{-,s} = \hat{b}^\dagger_{s,1}\hat{b}_{s,0} . \tag{2.68}$$

In this case we get

$$H_{\mathrm{BB}}/\hbar = \chi\hat{L}^2_{z,N} + \frac{\Delta}{2}\left(\hat{b}^\dagger_{L,0}\hat{b}_{L,0} - \hat{b}^\dagger_{L,1}\hat{b}_{L,1}\right) + \lambda\left(\hat{b}^\dagger_{L,0}\hat{L}_{-,N}\hat{b}_{L,1} + \hat{b}^\dagger_{L,1}\hat{L}_{+,N}\hat{b}_{L,0}\right) , \tag{2.69}$$

with the identification

$$\lambda = X^{\mathrm{SCC}} \tag{2.70}$$

$$\chi = -\chi_N - \chi_L - \chi_{NL} \tag{2.71}$$

$$\begin{aligned}\Delta = -\Big\{ &\left(E_{L,1}(B_0) - E_{L,0}(B_0)\right) - \left(E_{N,1}(B_0) - E_{N,0}(B_0)\right) \\ &+ \chi_L(\hat{N}_L - 1) - \chi_N(\hat{N}_N - 1) + \frac{1}{2}\chi_{NL}(\hat{N}_N - \hat{N}_L) + 2M\left(-\chi_L - \frac{1}{2}\chi_{NL}\right) \Big\} .\end{aligned} \tag{2.72}$$

We call H_{BB} the "building block" Hamiltonian, since it incorporates the important features to be considered a minimal gauge theory. In the following we use H_{BB} in the representation given in equation 2.76. The parameters λ, χ and Δ we call consequently "building block parameters". The physical origin of those is outlined in Fig. 2.5.

We associate the sodium degrees of freedom to a gauge field and the lithium degrees of freedom to a matter field. For lithium we introduce the notation $\hat{b}_{L,0} \equiv \hat{b}_{\mathrm{p}}$ for "particle" and $\hat{b}_{L,1} \equiv \hat{b}_{\mathrm{v}}$ for "vacuum". This labeling indicates that when lithium is prepared fully in the $M_F = 1$ state, this can be considered to be the vacuum configuration in the widest sense and thus population transfer to the $M_F = 0$ corresponds to excitations in the matter field i.e. particles, see [36].

The building block Hamiltonian has great similarity to the QLM as introduced previously. In the Schwinger boson representation the sodium population imbalance is mapped on a term $\propto \hat{L}^2_z$ which is exactly the same term that describes the dynamics of the gauge field of a single link in the QLM of 2.39. Furthermore, the spin-changing-collision term is in its form equivalent to the gauge interaction (correlated hopping) term of 2.39, where the two internal

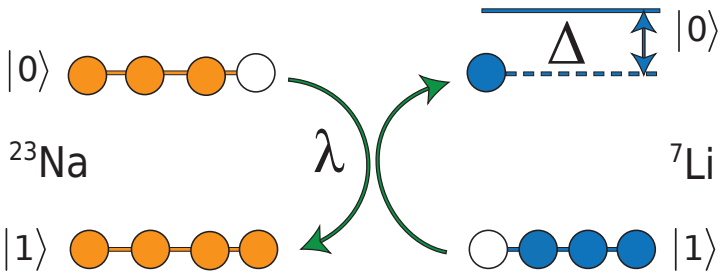

Figure 2.5.: **Relation of building block parameters to microscopic properties of the system**. Parameter λ stems from the heeronuclear spin changing collision process, where the internal state of one species is changed in correlation with an opposite change in the other species. Parameter Δ has several contributions, including energy shifts due to the Zeeman effect, mean field shifts and total magnetization. All these effects can be interpreted as the parameter that shifts the resonance of the spin changing collisions process by effectively introducing an energy penalty. Parameter χ is a combination of overlaps of all species and is not indicated in the figure for the sake of clarity. Detailed discussion of the building block parameters with respect to our experimental system is found in section 4.1.2.

states of lithium represent the two component spinors of the matter field. Since the building block is realized in a single trap, i.e. physically represents one site, one interprets the two lithium states each as one component of two adjecent matter sites in the lattice gauge theory (see Fig. 2.6) with the notation $\hat{b}_\mathrm{p} \equiv \hat{b}_{n+1,\mathrm{p}}$ and $\hat{b}_\mathrm{v} \equiv \hat{b}_{n,\mathrm{v}}$. The building block Hamiltonian is U(1) gauge invariant which is formally shown by defining the reduced Gauß' law operators

$$\hat{G}'_n = \hat{L}_z + \hat{b}^\dagger_\mathrm{p}\hat{b}_\mathrm{p} \,, \qquad \hat{G}'_{n+1} = -\hat{L}_z + \hat{b}^\dagger_\mathrm{v}\hat{b}_\mathrm{v} \,. \tag{2.73}$$

Due to total angular momentum conservation in the system $\left[H_\mathrm{BB}, \hat{G}'_n\right] = 0$ and $\left[H_\mathrm{BB}, \hat{G}'_{n+1}\right] = 0$ is fulfilled and thus the building block Hamiltonian is gauge invariant.

The building block contains all necessary gauge invariant processes to construct an extended lattice gauge theory by assembling multiple building blocks. The proposal for this implementation is outlined in the next section.

2.4.4. Extended lattice gauge theory based on building blocks

We suggest to implement a 1d extended U(1) lattice gauge theory based on elementary building blocks 2.64. As a first step one introduces a deep optical lattice potential. Such that atomic clouds of sodium and lithium are localized on individual lattice wells n. For sufficiently strong confinement in the lattice wells, direct tunneling of atoms between neighbouring wells is supressed and the system resembles an array of individual building blocks. Mapping the cold atom degrees of freedom onto building block parameters is then straightforward as in the previous section (detailed steps are found in the supplementary materials of [36]).

Finally, the building blocks need to be connected with the term (in analogy to the mass

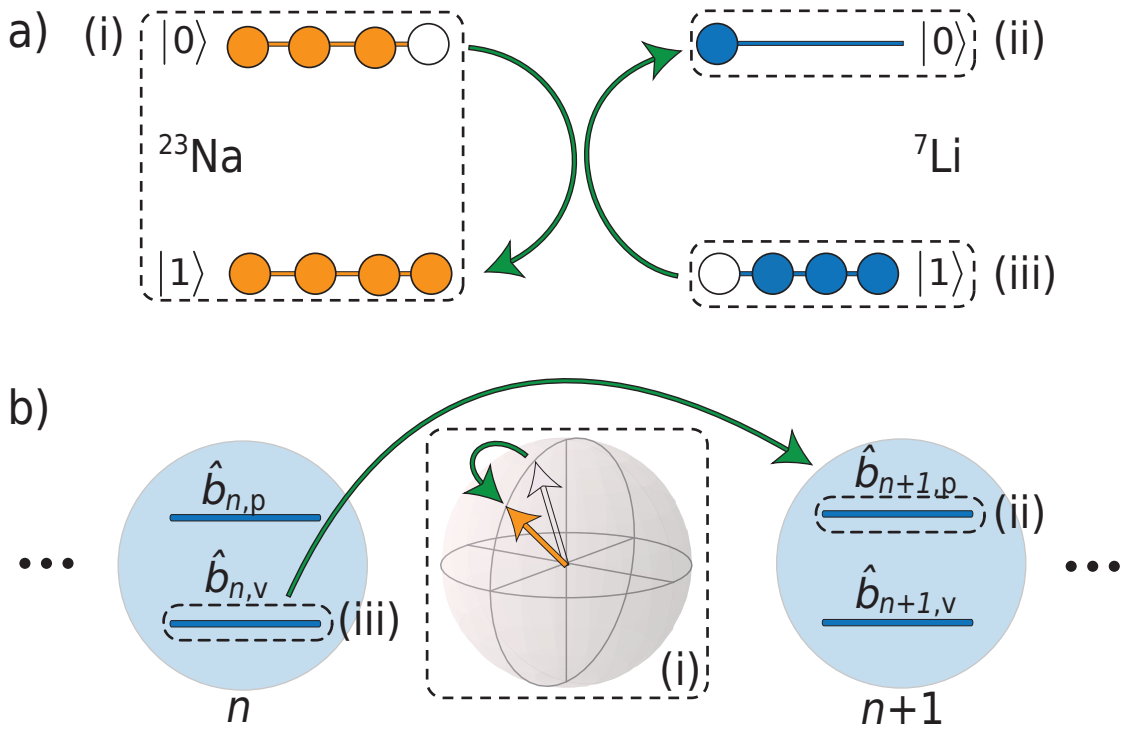

Figure 2.6.: **Illustration of the way the building block maps onto a lattice gauge theory. a) The building block in the cold atom system. b) Building block as part of an extended lattice gauge theory**. Sodium and lithium atoms are trapped in a single optical dipole trap. The internal states of sodium are mapped on spin operators which represent the gauge field. The two internal states of lithium correspond to the matter field components as in the Wilson representation 2.30. The gauge invariant hopping of matter in the lattice gauge theory is realized experimentally via spin-changing collisions between sodium and lithium. Since the cold atom system is physically located at one site, the building block is interpreted as a single quantum link with one matter field component each of the two adjecent matter sites n and $n+1$.

term in 2.39)

$$H_{\Omega,n} = \Omega \left(\hat{b}^{\dagger}_{n,\mathrm{v}} \hat{b}_{n,\mathrm{p}} + \mathrm{h.c.} \right) \ , \tag{2.74}$$

with Ω being the coupling strength between the two matter states $\hat{b}_{n,\mathrm{v}}$ and $\hat{b}_{n,\mathrm{p}}$. This coupling can be realized, for instance, with Raman-assisted tunneling [74–77]. It is important to note that in the lattice gauge theory this coupling is between matter components on the same matter site, however, as mentioned in the previous section one physical site in the optical lattice does not correspond to a site of the simulated lattice gauge theory, and therefore the Raman-assisted tunneling is coupling different internal lithium states of neighbouring optical

lattice sites (see Fig. 2.7). The full Hamiltonian of the proposed extended lattice gauge theory then reads

$$\hat{H} = \sum_n \left[\hat{H}_{\mathrm{BB},n} + \hat{H}_{\Omega,n} \right] \ , \tag{2.75}$$

with the index notation for the building block $\hat{b}_\mathrm{p} \equiv \hat{b}_{n+1,\mathrm{p}}$, $\hat{b}_\mathrm{v} \equiv \hat{b}_{n,\mathrm{v}}$ and for the sodium in Schwinger boson representation $\hat{\vec{L}} \equiv \hat{\vec{L}}_n$

$$H_{\mathrm{BB},n}/\hbar = \chi \hat{L}_z^2 + \frac{\Delta}{2}\left(\hat{b}_\mathrm{p}^\dagger \hat{b}_\mathrm{p} - \hat{b}_\mathrm{v}^\dagger \hat{b}_\mathrm{v}\right) + \lambda\left(\hat{b}_\mathrm{p}^\dagger \hat{L}_- \hat{b}_\mathrm{v} + \hat{b}_\mathrm{v}^\dagger \hat{L}_+ \hat{b}_\mathrm{p}\right) \ . \tag{2.76}$$

Compared to former proposals for U(1) lattice gauge theories in one dimension [16, 17],

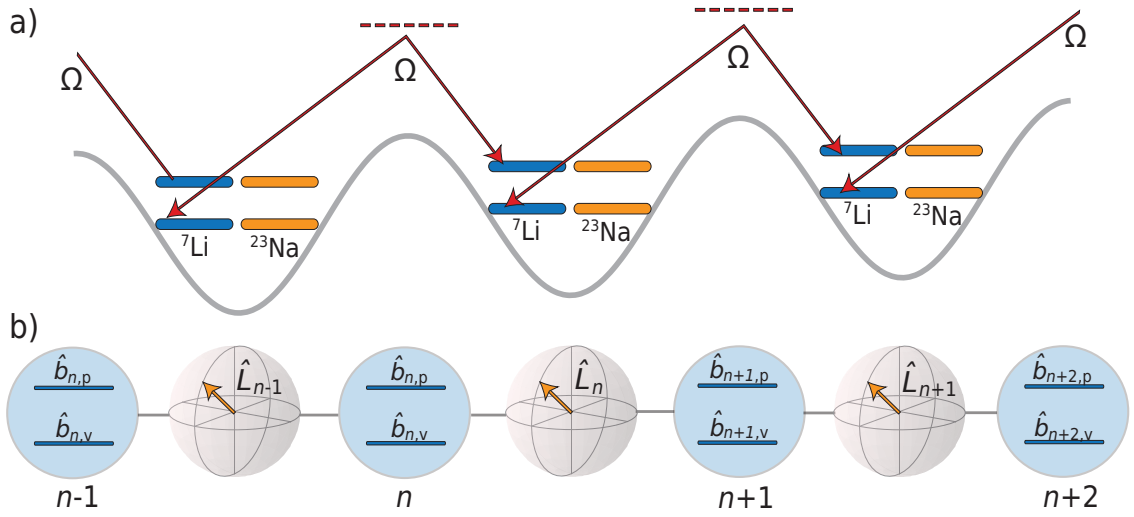

Figure 2.7.: **Illustration of the proposed implementation of an extended lattice gauge theory based on building blocks. a) The implementation in the cold atom system. b) The corresponding simulated lattice gauge theory in the QLM formalism.** Individual building blocks are arranged next to each other by means of an optical lattice potential. The coupling of neighbouring building blocks 2.74 is achieved by Raman-assisted tunneling with the coupling strength Ω. To avoid transitions between internal states of lithium on the same optical lattice site, the lattice potential is tilted. The gauge preserving interactions are realized by spin-changing collisions according to Fig. 2.6, which are not indicated in this illustration for the sake of clarity.

which were relying on a one-to-one correspondance of optical lattice and simulated lattice, the architecture presented here exhibits various advantages. First of all, the mentioned proposals rely on a species selective lattice which is technically much more demanding compared to an optical lattice where both species are trapped on the same sites. Furthermore the implementation presented here contains all necessary gauge invariant dynamics on-site. In

order to increase the interaction strength of the gauge invariant coupling (spin-changing collisions) one can use a stronger confinement of the lattice, leading to a larger overlap of the atomic clouds. At the same time a stronger confinement aids in supressing unwanted spontaneous tunneling between sites. The necessary coupling 2.74 is then tuned by the independend process of Raman-assisted tunneling where the coupling can be varied with experimental parameters, e.g. laser intensity, and wherefore account for possibly small spatial overlap of lithium atoms in neighbouring sites.

In former proposals sodium and lithium are arranged on alternating lattice sites and the gauge invariant coupling involves spin-changing collisions across multiple lattice sites. Therefore in order to supress direct tunneling via tight confinement inevitably compromises the rate of spin-changing collisions.

In terms of the simulated lattice gauge theory the here described system is equivalent to 2.39 as proposed in [17], with the difference of having bosonic degrees of freedom for the matter fields instead of fermionic ones as well as high population of the matter field sites. Therefore the continuum limit of this theory does not correspond to QED since Lorentz invariance is not fulfilled. However, the significant features of a gauge theory, especially the protection of gauge invariance, are not influenced by the bosonic matter fields. The building block was experimentally realized first with bosonic sodium and bosonic lithium for technical reasons and replacing lithium by the fermionic isotope ^{6}Li in the experiment is straightforward.

2.5. Summary

In this chapter we have introduced the main theoretical concepts that are important for a comprehensive understanding of this work. First main aspect was to provide a basis understanding of gauge theories. For instance a formal description how gauge fields arise from enforcing gauge invariance on the system. Furthermore, the goal was to break down lattice gauge theories into their essential ingredients and mechanisms aiming at an better understanding from an experimentalist's point of view. We have presented two different Hamilton formulations of quantum electrodynamics to exemplary show what needs to be engineered experimentally to sucessfully quantum simulated such theories. In essence these main ingedients are: Matter degrees of freedom, gauge field degrees of freedom, and a gauge invariant interaction between matter and gauge field. This interaction will lead to strong constraints on the resulting dynamics which manifests among others in an appropriate version of Gauss' law.

Second main aspect of this chapter was to introduce our novel approach for an experimental implementation to quantum simulate a U(1) lattice gauge theory in ultracold mixture experiments. This implementation is based on a specific building block, which by itself features matter degrees of freedom, gauge degrees of freedom and proper gauge invariant interaction. The full extended lattice gauge theory is achieved by spatial repetitions of individual building blocks and additional coupling between the building blocks. The physical system for the building block are trapped ultracold sodium and lithium atoms interacting via contact interaction. Starting out from a full microscopic description of the cold atom system we derived the building block as an effective model for this system. We pointed out the properties of the

building block that predestine it to be used as a fundamental cornerstone for a lattice gauge theory. Finally, we showed how the building block is used to construct the full extended U(1) lattice gauge theory and pointed out the advantages of this proposed implementation over former proposals.

3. Experimental system

This chapter is dedicated to the experimental aspects of this work including technical information about the experimental setup as well as the routines for data acquisition and processing. It is structured in the following way.

In the beginning we introduce the experimental apparatus that was used to generate the data that is presented in this work. The main components of the experimental setup have been developed prior to this work and are described elsewhere [39–42]. Therefore the description of the apparatus will focus on the main aspects. The sequence that constitues an individual experimental cycle until reaching ultracold clouds of sodium and lithium is explained. For further detailed information on this topic we refer to the cited work.

Next we describe the absorption imaging routine that is used in our experiment. This includes a theoretical description of this imaging technique as well as the particular optical setup that is used in our experiment. Furthermore we show the method that we used to calibrate the imaging procedure for absolute atom number detection.

Then we present measurements that characterize our cold atom system, this includes trapping frequency measurements of the optical dipole trap, which is the final trapping stage of the experiment, as well as measurements of condensate fraction of the species.

The main focus of the chapter is then a detailed description of the procedure to experimentally realize heteronuclear spin changing collisions between sodium and lithium. We start by explaining the initial setting of the experiment, including the trap configuration, the configuration of internal state population of the species and working offset magnetic field. We then explain how we initialize spin dynamics in the system and how we detect the signature for spin changing collisions.

In the last sections of this chapter we explain our data acquisition and data processing procedure for the experimental measurements on spin changing collisions that we performed. We show how we extract the necessary observables from large data sets of absorption images. We show that we use three experimental tuning parameters to systematically scan the parameter regime of spin changing collisions. These parameters are: The evolution time after the spin dynamics have been initialized, the initial internal sodium state population ratio, and the magnetic offset field during the experiment. For these parameters we exemplarily show how the data processing is applied.

Apart from the first section, where the experimental setup is introduced, this chapter represents genuine and generally novel work performed by myself, in particular the experimental measurements on heteronuclear spin changing collisions between sodium and lithium.

3.1. Experimental setup — an overview

Our experimental apparatus is a machine dedicated to producing ultracold mixtures of sodium and lithium. The sodium isotope in the experiment is ^{23}Na, which is bosonic. In case of lithium we have access to two lithium isotopes, ^{6}Li (fermionic) and ^{7}Li (bosonic). As our lithium laser setup can only be tuned to one of the lithium isotopes, we can only trap one lithium species at a time together with sodium. In the course of this work we used exclusively the bosonic lithium species, however, changing the experimental setup in order to use fermionic lithium only involves minor changes (choosing different frequency lock point and recoupling some beam paths).

The main components of the current setup have been described in detail in former works [40–42]. Therefore the description here will be restricted to a general overview, mainly to point out the main stages within one experimental cycle.

3.2. Sequence for preparing ultracold atomic mixtures

This section describes the chronological order of a typical experimental sequence from the beginning to the creation of BECs of sodium and lithium.

The atom source in the experiment is a dual species oven [78]. Collimated atomic beams of sodium and lithium with longitudinal velocities[1] in the order of $1000\,\mathrm{m\,s^{-1}}$ are copropagating out of the oven. The atoms are slowed down by a Zeeman slower which is designed to enable the slowing of both species [80]. The slowed atomic beams are used to load a two species Magneto-Optical-Trap (MOT) [81]. The loading rate for lithium was generally much lower than for sodium (loading time in the order of tens of seconds compared to a few seconds for sodium). Therefore we programmed our sequences such that an experimental cycle starts with parameters tuned to favour the lithium MOT loading and once it has been preloaded, parameters are switched to enable the loading of a large sodium MOT as well. This two stage loading procedure ensured to have a sufficient amount of lithium for the experiments.

After the MOTs have been loaded, the atoms are transferred to the magnetic trap (MT) which is a Ioffe-Pritchard type trap in cloverleaf configuration [82]. Detailed parameters and geometries of the MT in our experiment are found in [39]. Right before being transfered into the MT we apply a spin polarizing scheme [40, 83] to prepare both species in the stretched hyperfine state $|F = 2, m_F = 2\rangle$ in order to increase the transfer efficiency into the MT as well as to avoid detrimental atom loss in the MT later on due to spin exchange collisions. In the MT we perform a standard forced evaporative cooling technique on sodium using microwave (MW) coupling between the two hyperfine states $|F = 2\rangle$ and $|F = 1\rangle$. With this procedure we decrease the temperature of the sodium atoms to a few μK. Lithium atoms are cooled by sodium sympathetically [84].

After the evaporation in the MT, both atomic clouds are loaded into the optical dipole trap (ODT), which is comprised of two crossed beams from a far red-detuned ($1064\,\mathrm{nm}$) infrared laser. We call the two beams “waveguide” and “dimple”. In order to overcome the problem of

[1] At typical oven temperatures of 350°C the longitudinal velocity is centered around $800\,\mathrm{m\,s^{-1}}$ for sodium and $1600\,\mathrm{m\,s^{-1}}$ for lithium [79].

strongly mismatching spatial modes of MT and ODT, the tranfer is arranged in two stages: First, only the waveguide is ramped up leading to an elongated confinement of the atoms and which is favouring the transfer efficiency as the waveguide accounts for the elongated shape of the MT. After being loaded into the waveguide, both species are transfered with a rapid adiabatic passage (RAP) [85] from $|F = 2, m_F = 2\rangle$ to $|F = 1, m_F = 1\rangle$. Compared to the F = 2 manifold, atoms in the hyperfined groundstate exhibit about ten times lower three-body loss rates, which is a major issue to consider when the density is increased in the crossed dipole trap. After the RAP the dimple beam is ramped up and we perform evaporative cooling in the ODT by lowering the laser intensity. Within this last evaporation we reach Bose-Einstein condensation of both atomic species.

At this point we have set the foundation for the spin dynamics experiments which are the main focus of this work. Section 3.5 of this chapter provides detailed information related to this stage of the experiment. The redout via absorption imaging is described in section 3.3. Since this imaging technique is destructive it marks the finish of a single experimental run. Fig. 3.1 summarizes the aforementioned segments of a typical experimental cycle indicating the main stages of the sequence.

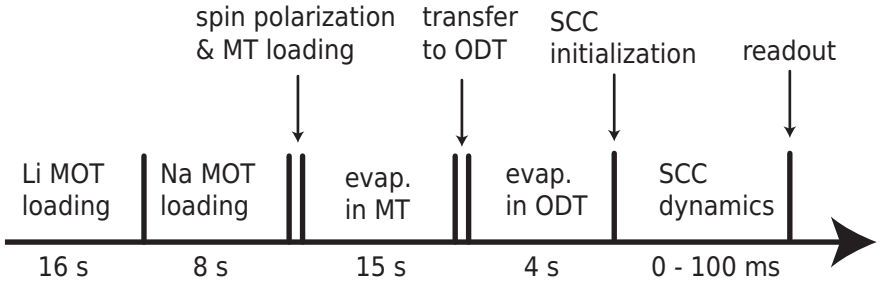

Figure 3.1.: **Timeline of a typical experimental cycle.** The main conceptual steps of the sequence are mentioned and the usual duration is indicated (not to scale). Since the redout is absorption imaging (which is destructive) the experimental sequence has to be repeated after each measurement.

3.3. Absorption imaging

There are various imaging techniques in order to retrieve information about ultracold atomic clouds [86–88]. In our experiment we use an absorption imaging technique, which relies on the resonant interaction of atoms with light. The basic idea of this method is to illuminate the atomic cloud with a laser beam pulse that is tuned to an optical transition of the species. A certain amount of photons from the imaging beam are scattered due to the atom light interaction. When recording the imaging beam pulse after passing through the atoms this scattering results in a decrease of intensity in the beam profile. This signal can be used to retrieve information about the spatial distribution as well as the total atom number of the cloud.

3.3.1. Theoretical description of absorption imaging

The reduction in light intensity when passing through an absorptive medium on resonance is described by Beer's law (following [88])

$$\frac{dI}{dz} = -n\sigma(I)I \ , \tag{3.1}$$

where I is the intensity of the imaging light, n is the density of the absorptive medium (in our case the ultracold atomic clouds), $\sigma(I)$ is the intensity dependent scattering cross section and z is the propagation direction of the imaging beam. The intensity dependence of the cross section stems from saturation effects in the transition[2]. We can write the intensity dependence in 3.1 explicitly as

$$\frac{dI}{dz} = -n\frac{\sigma_0}{\alpha^*}\frac{1}{1+I_{\mathrm{eff}}^{\mathrm{sat}}}I \ , \tag{3.2}$$

with $\sigma_0 = 3\lambda^2/2\pi$ being the resonant scattering cross section assuming a two level transition. Here we have introduced the effective saturation intensity $I_{\mathrm{eff}}^{\mathrm{sat}} = \alpha^* I_0^{\mathrm{sat}}$ with the dimensionless parameter $\alpha^* > 1$, which accounts for experimental imperfections leading to a deviation from the ideal value of the saturation intensity I_0^{sat}. By integrating equation 3.2 in z direction one obtains an expression for the atomic column density

$$n_c(x,y) = -\frac{1}{\sigma_0}\left[\alpha^* \ln\left(\frac{I_f(x,y)}{I_i(x,y)}\right) + \frac{I_i(x,y) - I_f(x,y)}{I_0^{\mathrm{sat}}}\right] \ , \tag{3.3}$$

where $I_i(x,y)$ and $I_f(x,y)$ are the initial (final) intensities before (after) passing through the atomic cloud. From that the total atom number is retrieved by integrating the column density in xy direction. In practice, $I_i(x,y)$ and $I_f(x,y)$ are detected with cameras during a single experimental cycle. I_0^{sat} and α^* have to be calibrated with an independent set of measurements. The exact details are explained in the following sections.

3.3.2. Experimental setup and imaging sequence

Independently generated imaging light for both species (imaging transitions with wavelengths $\lambda_{\mathrm{Na}} = 589\,\mathrm{nm}$ and $\lambda_{\mathrm{Li}} = 671\,\mathrm{nm}$) is coupled into the same optical fiber and guided to the experiment table. After exiting the fiber outcoupler, the collimated beams pass a polarizing beam splitter and enter the vacuum glass cell where they illuminate the trapped atomic clouds. In order to strongly increase the intensity of the imaging light at the position of the atoms (which will be used for calibration of the imaging system), a lens with positive focal length can be placed in the imaging beam path right before it enters the glass cell. The imaging beam profile is imaged with the following optical assembly, see Fig. 3.2. First, a specially designed

[2]The scattering response of a two level atom scales linearly in the low intensity limit and approaches a constant value in the high intensity limit, see [85]

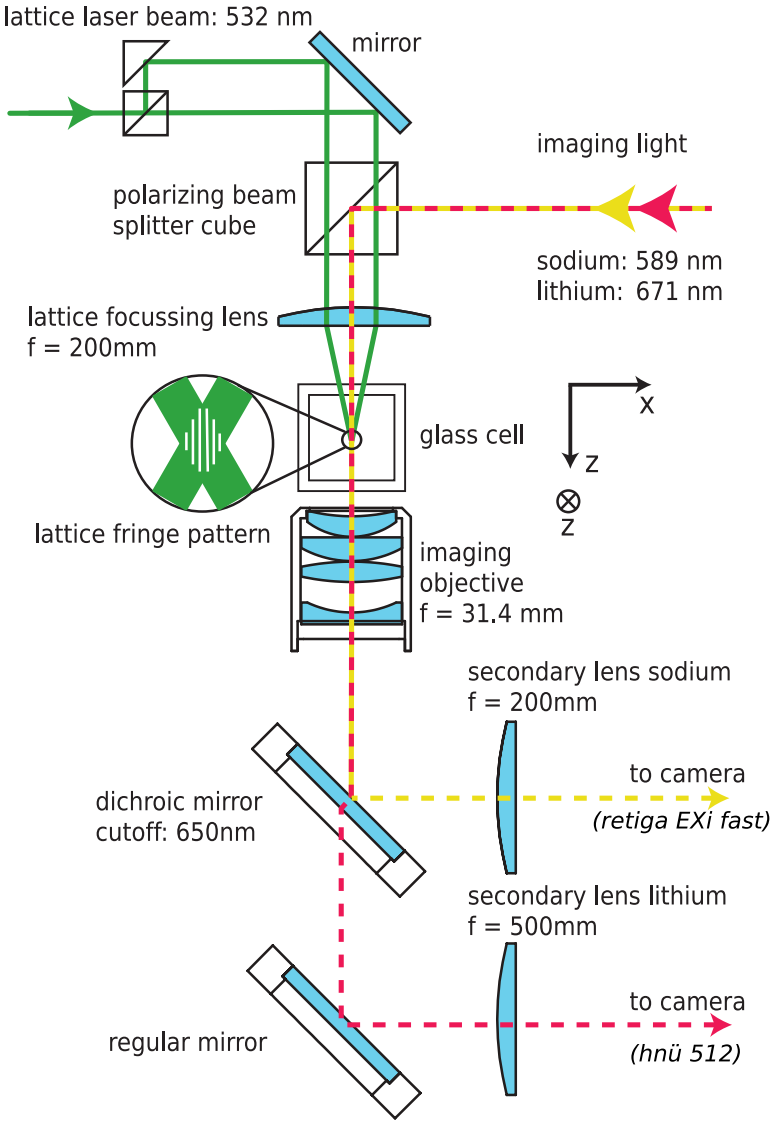

Figure 3.2.: **Sketch of the optical elements in the imaging system.** Imaging light for sodium and lithium is copropagating and illuminates the atomic clouds in the glass cell. The atoms are imaged by a system of an objective lens and a secondary lens. After the objective lens the two wavelengths are separated by a dichroic mirror and imaged on separate cameras. Also shown is the optical lattice setup which shares optical elements with the imaging beams. Two parallel beams of the same laser are crossed onto the position of the atoms by a focussing lens. The lattice spacing is determined by the spatial separation of the parallel beams and the focal length of the focussing lens. This is used to determine the magnification of the imaging systems.

objective lens [89] ($f_{\mathrm{obj}} = 31.4\,\mathrm{mm}$ for lithium and $f_{\mathrm{obj}} = 31.18\,\mathrm{mm}$ for sodium) is placed close to the glass cell such that its focal plane matches the plane of the atoms, effectively

sending the image to infinity. After the objective lens, a dichroic longpass (cutoff at $650\,\mathrm{nm}$) is placed in the imaging path to separate the imaging beams of both species into two individual paths. The final image of each path is cast by an individual secondary lens ($f_{\mathrm{sec}} = 500\,\mathrm{mm}$ for lithium and $f_{\mathrm{sec}} = 200\,\mathrm{mm}$ for sodium) onto a CCD camera. Optical bandpass filters (Semrock BrightLine HC 673/11 for lithium and HC 590/20 for sodium) are placed in front of each camera to avoid any light besides the imaging pulse to enter the detector.

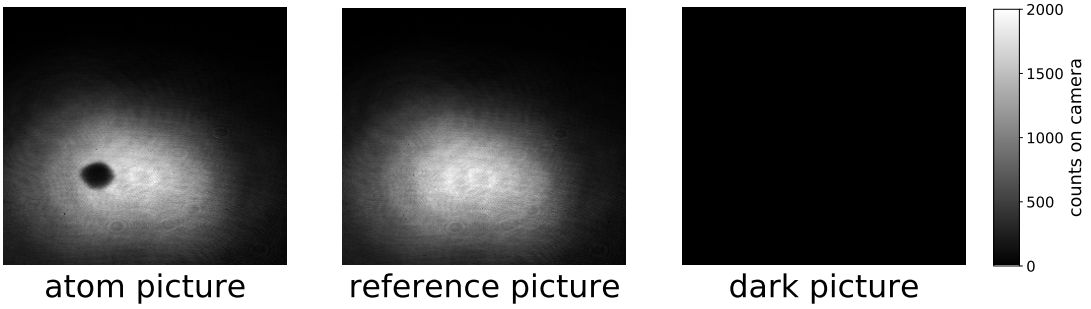

Figure 3.3.: **Example set of the three pictures that are taken during the imaging sequence (sodium imaging).** The images in chonological order as they are taken during the imaging procedure. For each image the camera is exposed for the duration of the imaging pulse. Inbetween pictures there is a dwell time of $400\,\mathrm{ms}$. In the first two pictures one can see the clear near gaussian intensity profile of the imaging light. The black shadow in the middle of the imaging light profile in the atom picture is cast by a sodium BEC in time of flight.

The absorption imaging sequence constitues the end of a single experimental cycle (as the measurement is destructive). In particular, during the imaging procedure a set of three images per species is recorded: The atomic picture $I_{\mathrm{atom}}(x, y)$, the reference picture $I_{\mathrm{ref}}(x, y)$ and the dark picture $I_{\mathrm{dark}}(x, y)$, see Fig. 3.3. First picture taken is the atomic picture that records the imaging light pulse that interacts with the atoms. During this process the atoms are expelled from the trap due to the resonant light force. Afterwards, the reference picture is taken which records a light pulse with the same parameters (duration, intensity) as the first pulse but in the absence of any atoms. The last picture is the dark picture which records the background signal on the camera when all experimental light sources are shut down. With this set of images we employ euation 3.3 to calculate the atomic column density using the identification

$$I_f(x, y) = I_{\mathrm{atom}}(x, y) - I_{\mathrm{dark}}(x, y) \tag{3.4}$$

$$I_i(x, y) = I_{\mathrm{ref}}(x, y) - I_{\mathrm{dark}}(x, y)\ , \tag{3.5}$$

and the experiment specific values for I_0^{sat} and α^*, which need to be calibrated as explained in the following section. Note that the imaging frequency for both species is tuned to the $F = 2 \longrightarrow F'$ transition which necessitates the use of a repumping beam when the atoms occupy the hyperfine ground state before being imaged. The repumping beam is then shone in simultaneously with the imaging beam. In the case of lithium the same repumper beams as in the MOT phase are used, for lithium the repumper is shone in from one side perpendicular

to the imaging beam (same optical path as used during spin polarization).

3.3.3. Calibration of the imaging magnification

In order to determine the total atom number from the absorption images the magnification of the imaging system has to be known. As described in the previous section we have to individual imaging paths for sodium and lithium as well as two individual cameras: *Retiga EXi fast* from Qimaging for the sodium imaging and *hnü 512* from nüvü cameras for the lithium imaging.

In our imaging system that is comprised of imaging objective and secondary lens, the ideal case magnification M is given as the ratio of the secondary lens focal length f_{sec} and imaging objective focal length f_{obj}

$$M = \frac{f_{\mathrm{sec}}}{f_{\mathrm{obj}}} \,. \tag{3.6}$$

As this formula for M assumes perfect optical elements and perfect alignment, it is advisable to determine the magnification directly with a measurement. One profound method for determining M is to observe the atoms in free fall and relate the travelled distance (in units of camera pixels) to the expected travel distance (in real space units) from gravity. In our setup, however, this method can not be applied, because the imaging beam propagation direction is parallel to gravity.

Therefore we used our optical lattice setup to calibrate the magnification. This is suitable, since the lattice beams share the same optical path as the imaging beam after they are combined on a polarizing beam splitter cube, see Fig. 3.2.

The lattice is generated in the following way (for detailed description on the lattice setup, see [42, 90]: A single laser beam is split into two parallel beams of equal power and a distance $d = 10\,\mathrm{mm}$ between the two beams. The two parallel beams are focussed onto the position of the atoms by a focussing lens of focal length $f_{\mathrm{foc}} = 200\,\mathrm{mm}$. Due to the initial separation of the two parallel beams, they cross at the position of the atoms under an angle 2α, where α is geometrically defined by

$$\tan\alpha = \frac{d}{2f_{\mathrm{foc}}} \,. \tag{3.7}$$

The crossed lattice beams create a periodic interference pattern with periodicity a_{latt} determined as

$$a_{\mathrm{latt}} = \frac{\lambda}{2\sin\alpha} \,, \tag{3.8}$$

with λ being the wavelength of the lattice laser light. On the left hand side of Fig. 3.4 we show the fringe pattern as directly recorded on the lithium camera (for test purposes this was recorded at low laser power and with the bandpass filter in front of the camera removed). On the right hand side of Fig. 3.4 we show an in situ absorption image of lithium in the

crossed dipole trap with superimposed lattice laser beams. Since the lattice laser wavelength is $532\,\mathrm{nm}$, the lattice potential is repulsive and atoms accumulate in the regions of dark fringes of the lattice.

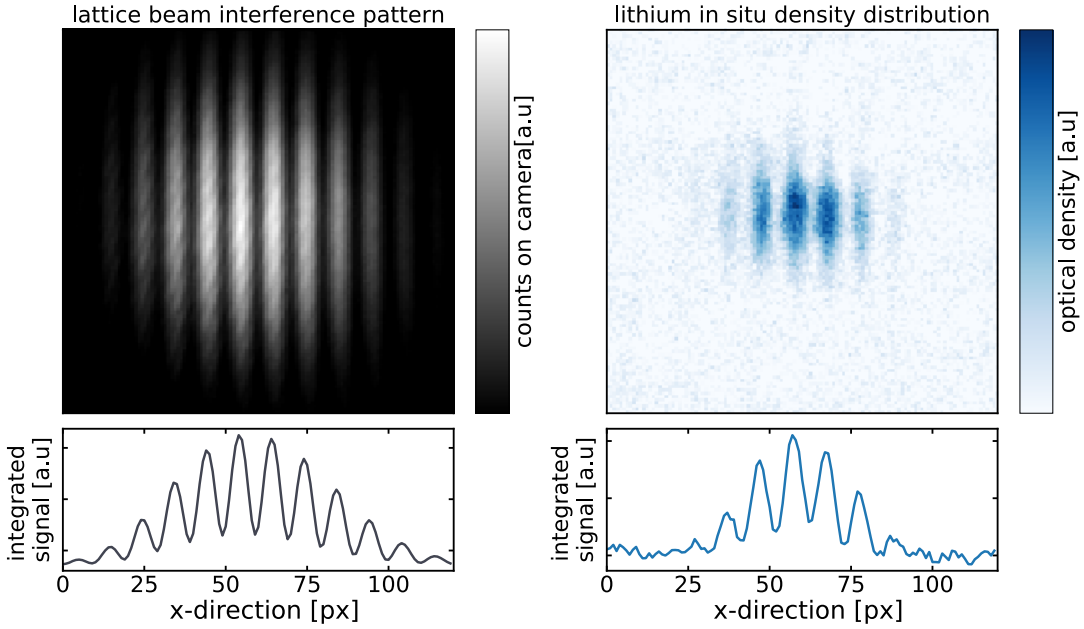

Figure 3.4.: **Experimental measurements of the optical lattice for calibration of the magnification. Direct measurement of the Laser intensity pattern on the lithium camera (left) and in situ density distribution of lithium in a combined trap of lattice and crossed dipole trap (right).** On the left hand side is a direct image of the laser pattern on the lithium camera with reduced intensity. On the right hand side is an in situ image of lithium when the regular optical dipole trap is superimposed with the lattice. By fitting the periodic structure one obtains the lattice spacing in camera pixel units. Since the theoretical lattice spacing in real space units is known from geometric properties (see. equation 3.8), with this measurements one can determine the magnification of the imaging system.

We determine a_{latt} by fitting a sine to the integrated signals (after we manually compensated for the evelope). The fitting yields $a_{\mathrm{latt}} = (10.16 \pm 0.03)$ px for the interference pattern and $a_{\mathrm{latt}} = (10.27 \pm 0.08)$ px for the density distribution of lithium. These values are compared to the predicted lattice spacing $a_{\mathrm{latt,pred}}$ using equations 3.7 and 3.8 with the known values $d = 10\,\mathrm{mm}$ and $f_{\mathrm{foc}} = 200\,\mathrm{mm}$ yielding $a_{\mathrm{latt,pred}} = 10.6\,\mu\mathrm{m}$. By knowing that the real pixel size of the *hnü 512* is $16\,\mu\mathrm{m} \times 16\,\mu\mathrm{m}$ the magnification is estimated to be $M_{\mathrm{Li}} = 15.44 \pm 0.12$ for the lithium imaging. With the same procedure the magnification of the sodium imaging (pixelsize *Retiga EXi fast* is $6.45\,\mu\mathrm{m} \times 6.45\,\mu\mathrm{m}$) is determined to be $M_{\mathrm{Na}} = 6.58 \pm 0.04$. Table 3.1 summarizes the determined values for the magnification depending on species and evaluation method.

	magnification using 3.6	magnification using lattice pattern
sodium	6.41	6.58 ± 0.04
lithium	15.92	15.44 ± 0.12

Table 3.1.: **Summarizing the magnification of the imaging system based on the imaging path and the method of evaluation.** The errors on the values determined by the method that employ the lattice pattern represent standard error determined from the fitting routine.

3.3.4. Absolute atom number calibration

As described before, in order to determine the total atom number from an absorption image one has to know the two parameters I_0^{sat} and α^*. I_0^{sat} describes the saturation intensity in the ideal case of a driven two level system in the presence of a decaying excited state with decay rate Γ. The value for the saturation intensity is computed for each species according to [91]

$$I_0^{\mathrm{sat}} = \frac{\pi}{3}\frac{hc\Gamma}{\lambda^3} \,, \tag{3.9}$$

which results in $I_0^{\mathrm{sat}}(\mathrm{Na}) = 6.26\,\mathrm{mW\,cm^{-2}}$ and $I_0^{\mathrm{sat}}(\mathrm{Li}) = 2.54\,\mathrm{mW\,cm^{-2}}$. Since the numerical values are known, the calibration of I_0^{sat} reduces to determining how intensity of an imaging pulse in the plane of the atoms translates to counts detected on the camera, taking into account the properties of the imaging setup (quantum efficiency of camera, magnification, reflections on optics surfaces, etc.). To do so we make use of the fact that the imaging beam profile spatially fits within a camera frame, see Fig 3.3. We perform a sequence of measurements where we repeatedly record imaging beam profiles (without the presence of atoms) on the camera, varying the total power of the beam from shot to shot. In addition we measure the absolute total power of the beam with an optical laser powermeter. Assuming a gaussian profile for the imaging beam we determine the spot size parameter w and the peak intensity I_{peak} by a Gaussian fit to the recorded beam profiles. Together with the measured total power P_{tot} of the beam one can represent the physical values for the intensity in camera specific units using the relation between total power and peak intensity of a Gaussian beam $I_{\mathrm{peak}} = 2P_{\mathrm{tot}}/(\pi w^2)$. By displaying the count rate of a pixel on the camera as a function of intensity of the imaging beam and linear fitting the data yields

$$I_0^{\mathrm{sat}}(\mathrm{Na}) \equiv 20.3\ \frac{\mathrm{counts}}{\mathrm{px}\times\mu\mathrm{s}} \,, \tag{3.10}$$

$$I_0^{\mathrm{sat}}(\mathrm{Li}) \equiv 11.2\ \frac{\mathrm{counts}}{\mathrm{px}\times\mu\mathrm{s}} \,. \tag{3.11}$$

Next, α^* has to be calibrated. This parameter accounts for the fact that in the experiment the intensity to saturate the imaging transition is generally higher than I_0^{sat}. The deviation has multiple physical reasons. First, the atomic transition has substructure (Zeeman levels) in the excited as well as in the ground state. This leads to different steady state configurations of the optical pumping which are further dependent on the polarization of the imaging light. Residual detuning of the imaging light plus finite linewidth of the transition contribute to this effect, too. Furthermore, stray magnetic fields which lead to fluctuations in the quantization axis as well as limited quality in the polarization of the imaging light are experimental imperfections which are accounted for by introducing the effective saturation intensity.

There are various methods for determining the effective saturation intensity, [92] exploit the linear scaling of quantum fluctuations of mean atom number in a coherent spin state, [93] use the momentum transfer between imaging light and atoms. In this work we follow the method described in [88].

From equation 3.3 one sees that two terms enter the calculation of the column density. The first term contains the ratio of atomic and reference picture, the second one the difference. In the limit case of low intensity imaging $I \ll I_0^{\mathrm{sat}}$ the second term is negligible and for calculating the atomic density it is sufficient to know the ratio of atomic and reference picture. The downside of this regime is that an optically dense cloud is difficult to image due to its opaqueness, leading to a low signal to noise ratio. Furthermore imaging with low intensities requires longer imaging pulses to scatter a sufficient amount of photons for the overall signal. However, longer imaging pulses lead to stronger displacement of the atomic cloud during the imaging process due to radiation pressure. This can lead to significant defocussing effects as the cloud is pushed out of the focal plane of the imaging system. This effect is all the more dominant for lighter species. In Fig 3.5 we show this displacement of the cloud as a function of the imaging pulse length for different species and imaging intensities. For this example we assumed the atoms to be initially at rest and neglected the Doppler shift induced detuning. The displaced distance in light propagation direction Δ_z as a function of time is then calculated according to

$$\Delta_z = \frac{v_{\mathrm{rec}}\gamma_{\mathrm{p}}}{2}\, t^2 \,, \tag{3.12}$$

with v_{rec} being the recoil velocity and γ_{p} being the intensity dependent on-resonance scattering rate. As seen in Fig 3.5, Δ_z is about one order of magnitude larger for ^{23}Na and ^{7}Li than for ^{87}Rb, which is used in [88, 92].

Moreover, the figure reveals another impactful relation to consider. In order to restrain Δ_z to about 15μm, which corresponds to the depht of focus for the imaging lens in our setup [89], an imaging pulse for lithium in the low intensity regime ($I/I_0^{\mathrm{sat}} = 0.1$) can be about three times longer than in the high intensity case ($I/I_0^{\mathrm{sat}} = 10$). However, the total photon count in the imaging pulse is smaller by a factor of 30. This eventually limits accessible low intensity values due to too small signal to noise ratios or otherwise due to detrimental defocus effects.

In the high intensity limit $I \gg I_0^{\mathrm{sat}}$ the first term of equation 3.3 becomes less important. In this regime imaging pulses can generally be kept short, and aforementioned complications due to radiation force do not play a major role. However, as the scattering cross section is reduced

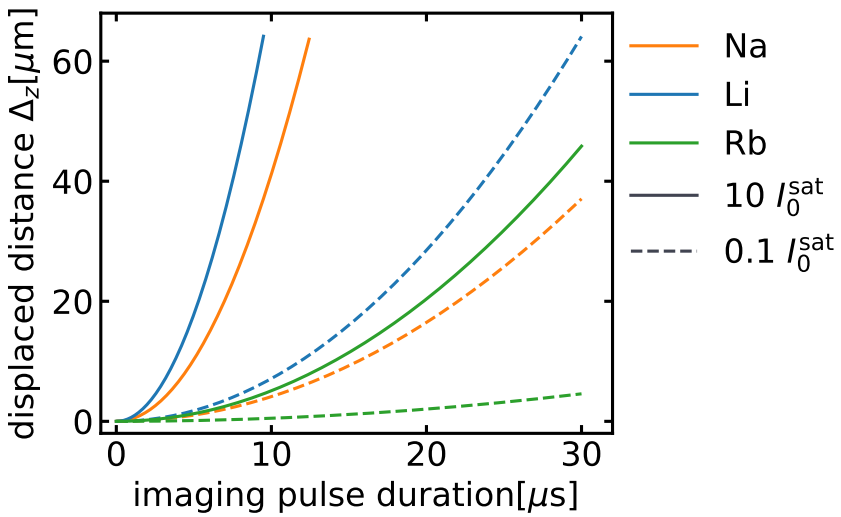

Figure 3.5.: **Displacement of an atom due to the light force during the imaging process as a funciton of imaging pulse duration.** The resonant atom light interaction results in a directed momentum transfer to the atoms which displace them from the initial position. The atoms are assumed to be initially at rest and Doppler induced shifts in detuning are neglected. Compared to rubidium the lighter species sodium and lithum are displaced much more for given pulse duration and imaging intensity.

at higher intensities this regime is disadvantageous when imaging very dilute atomic clouds. The conceptual idea for the calibration of α^* lies in the assessment that the column density (or total atom number) of an atomic cloud is a propertiy that is independent of the intensity of the imaging pulse. Therefore we repeatedly record atomic clouds with same experimental settings only varying the imaging pulse intensity. We compute the total atom number of the clouds according to equation 3.3 with different numerical values of α^*. The proper value for α^* is the one that results in the least fluctuations of the numerical value for the atom number across the whole range of imaging intensities, see Fig. 3.6. For each α^* the corresponding standard deviation of the atom number N is calculated, see Fig. 3.7. From this $\alpha^*(\mathrm{Na}) = 3.6$ and $\alpha^*(\mathrm{Li}) = 3.1$ are determined as the values corresponding to the minimum standard deviation. In summary, the imaging calibration employed here provides reasonable results compared to [94]. The method is straightforward to apply as from a technical perspective it does not require additional setups and sequences besides the regular imaging routine. However, in order for the method to perform properly the application of imaging intensities across multiple orders of magnitude is necessary which leads to considerably long imaging pulses for low intensities. This can lead to the aforementioned problems associated with acceleration of the atomic cloud during the imaging process. This can lead to systematic uncertainties in the calibration parameters especially considering the low mass of the atomic species we use in the experiment.

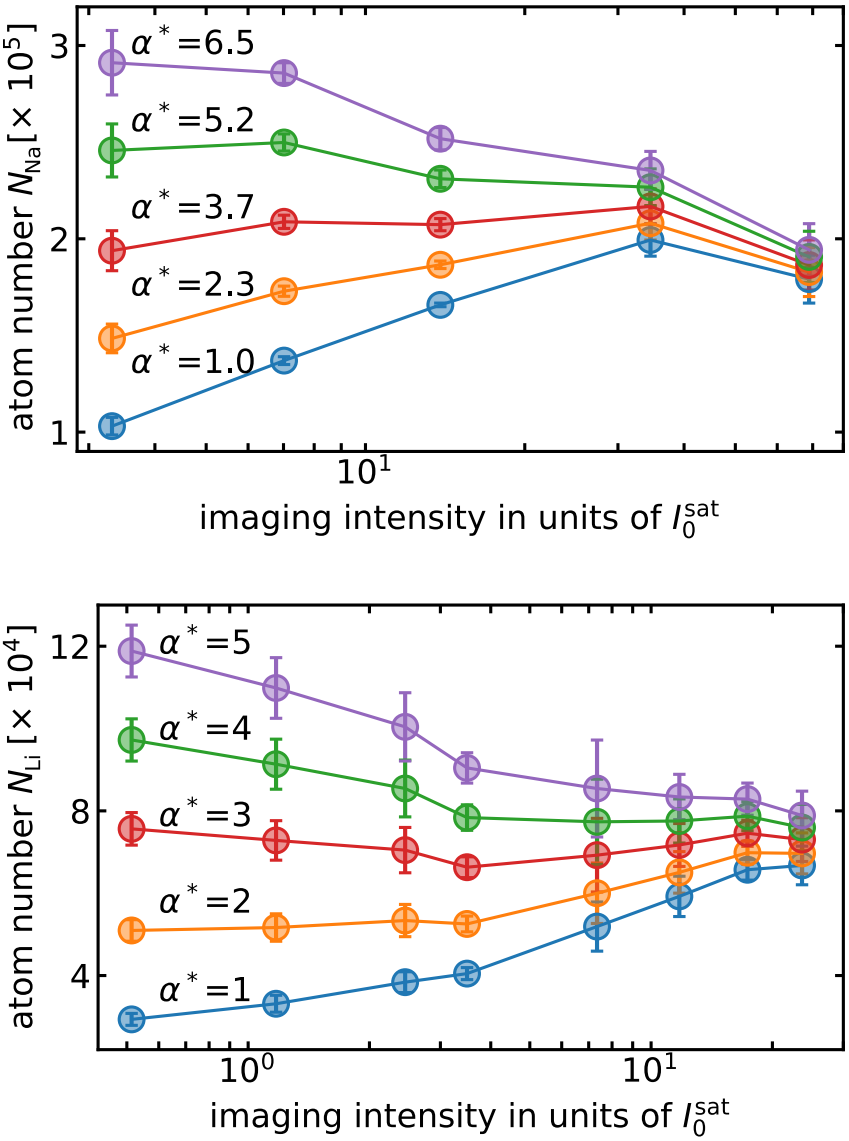

Figure 3.6.: **Calibration of the α^* parameter for sodium (top) and lithium (bottom).** Atomic clouds of the same atom number are recorded using varying imaging intensities. The atom number is evaluated using equation 3.3 for various values of α^*. As the atom number is a genuine property of the atomic cloud it is not supposed to vary with the imaging intensity. The value for α^* that results in the least fluctuation in atom number across the whole range of imaging intensities represents the correctly calibrated numerical value. Circles represent measured data, solid lines are guides to the eye.

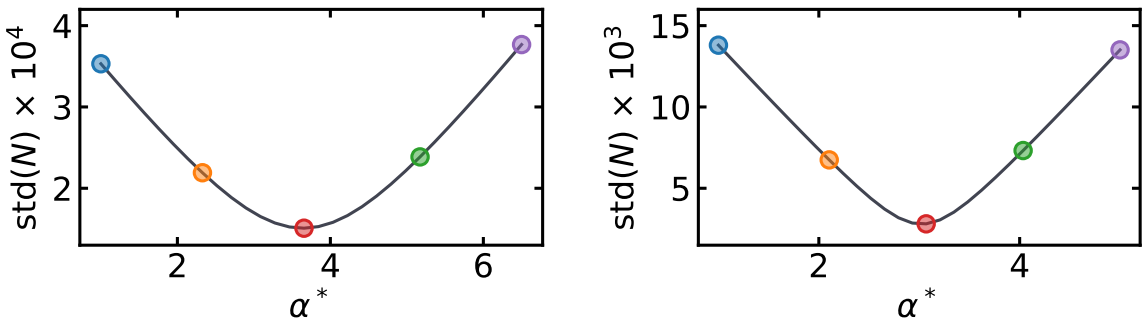

Figure 3.7.: **Fluctuation of atom number as a function of α^* for sodium (left) and lithium (right).** The standard deviation of the atom number across all imaging intensities is evaluated for each value of α^*. The minimum position of the graph corresponds to the proper calibrated parameter α^*. The colored data points correspond to the colored datasets shown in Fig. 3.6. The solid black line corresponds to the α^* datasets not shown in Fig. 3.6.

3.4. Characterization of trapped ultracold atoms

In the final stage of the experiment both species are trapped in an optical dipole trap. By lowering the dipole laser beams' intensity we further evaporatively cool both clouds and reach temperatures below the critical temperature of Bose-Einstein condensation. As this point we have set the experimental platform for the spin dynamics experiments which are described in section 3.5. Since all important measurements are performed at condiditions which are set at this stage it is necessary to characterize the experimental system at this point. On the one hand this is important in order to make quantitative comparisons between experimental data and theoretical models later on, since many parameters, for instance the total atom number, enter into theoretical models and have to be determined experimentally. On the other hand it is very useful from a technical point of view to benchmark the experimental system at this crucial stage. Having a set of benchmark values which can easily be checked allows to determine whether the whole experimental system is operating in a proper parameter space or technical readjustments are necessary.

3.4.1. Optical trapping potential

Optical dipole traps are a well established technique in ultracold atom experiments [95–99] to confine atoms in space. Hereby the laser intensity exerts an attractive or repulsive force on the atoms depending on the detuning of the laser relative to the optical transition in the atomic species. As mentioned in section 3.2 our dipole trap is generated by two crossed laser beams of a far red-detuned laser. The resulting potential can be approximated with a three dimensional harmonic potential, see equation 2.1. Experimentally the trapping potential can be characterized by determining the three trapping frequencies. In order to experimentally access the trap parameters with TOF measurements we perform externally

controlled trap oscillations by inducing a well controlled motional excitation of the atoms in the trap. Afterwards we release the atoms from the trap and the momentum of the atoms maps onto real space position. By varying the waiting time between excitation and release from the trap we sample the oscillation and thus the trapping frequency along the excited direction.

Experimentally the motional excitation is performed by applying a pulse to the piezo actuator that controls the mirror displacement in the optical path of the optical dipole beams, see Fig. 3.8. The pulse displaces one of the dipole beams and moves it back to the original

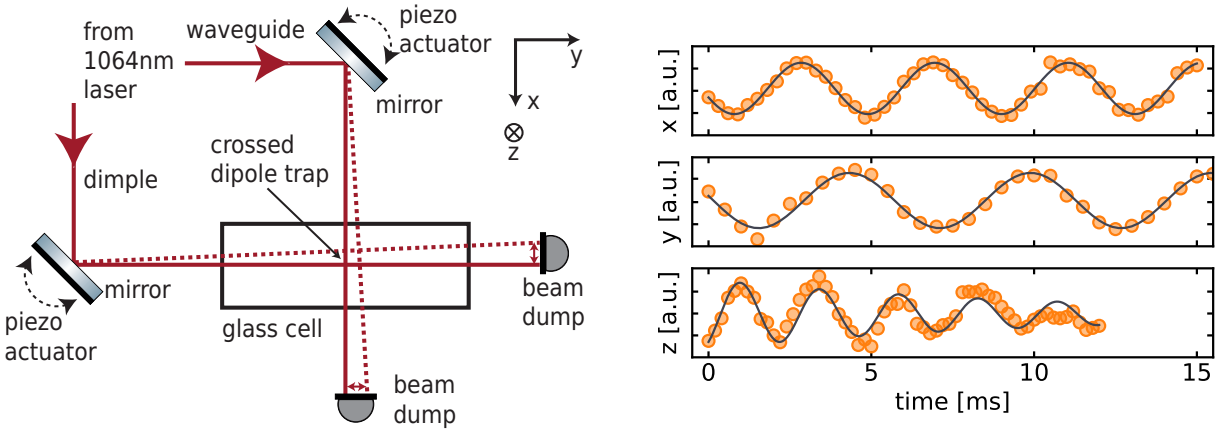

Figure 3.8.: **Schematic of the crossed optical dipole setup (left) and trap oscillations measurements with sodium (right).** A sudden shift of the trap center along a certain axis induced by piezo actuators placed on mirrors results in oscillation of the cloud. After the oscillation is excited the atoms are held in the trap for a certain time and released afterwards. The Absorption images are taken after a time of flight of 8 ms (x,y-direction) and 18ms (z-direction). The circles are the measured center of mass positions of the clouds as a function of time. The solid line is a damped sine fit to the data from which the trapping frequencies are deduced.

position. The pulse duration is chosen such that on one hand it is non adiabatic and on the other hand the trapped atoms can follow the changing trapping potential effectively resulting in a momentum transfer to the atoms perpendicular to the direction of the beam that is effected by the piezo pulse. Fig. 3.8 shows the results of the trap frequency measurements performed on sodium. For each direction we excite a clear oscillation of the atoms and determine the clouds center position as a function of waiting time after the excitation. A sinusoidal fit to the data yields for the three trapping frequencies

$$\omega_x = 2\pi \times (243.7 \pm 1.5)\text{Hz} \tag{3.13}$$
$$\omega_y = 2\pi \times (179.6 \pm 0.4)\text{Hz} \tag{3.14}$$
$$\omega_z = 2\pi \times (410.4 \pm 6.5)\text{Hz} \,. \tag{3.15}$$

The measurements in the x and y directions were recorded with the main imaging system

(optical axis parallel to gravity). In order to observe the oscillations in z direction we switched to the alternative side imaging system (optical axis perpendicular to gravity). The oscillation in z direction displays clear anharmonicity (as compared to the other directions), which can be due to following reasons: Since the side imaging has a lower magnification as the main imaging (by an order of magnitude), a larger amplitude of the piezo excitation was needed. This led to an oscillation with components not only in z, but also in other directions. Furthermore, the strong aplitude caused the measurement to probe the non harmonic parts of the trapping potential as equation 2.1 is an approximation only valid for small displacements around the trap's center position [99]. This is reflected in ω_z entailing the largest uncertainty of all three trapping frequencies.

It is sufficient to perform the trap frequency measurements on one species only, which we did on sodium. Afterwards the trap frequencies for lithium can be computed [40] using the relation

$$(\omega_x, \omega_y, \omega_z)(\mathrm{Li}) = 2.08 \times (\omega_x, \omega_y, \omega_z)(\mathrm{Na}) \ . \tag{3.16}$$

The factor of 2.08 results from the fact that sodium and lithium have different optical transition frequencies. The optical dipole trapping depends on the detuning of the dipole laser from a species' transition. As the dipole laser has a fixed wavelength of $1064\,\mathrm{nm}$, the different transition frequencies of sodium and lithium lead to different trapping frequencies.

We have set up the geometry of the trapping laser beams to purposely generate an anisotropie of the dipole trap towards the z direction. For that we set up the optical parameters such that the waveguide laser beam has a tighter focus in the direction of gravity. This is done to reduce the differential gravitational shift [100–102] which leads to a displacement of the trap center between the two potentials which are experienced by sodium and lithium. This displacement leads to a reduced spatial overlap of the two species and eventually makes the heteronuclear spin changing collision process which we intend to study less favorable. According to our measured trapping frequencies, the differential gravitational shift amounts to $1.1\,\mu\mathrm{m}$, which is a great improvement compared to former works in this group [40, 59] and considering that the spatial extend of the clouds is on the order of $10\,\mu\mathrm{m}$.

3.4.2. Benchmarking the ultracold mixture

In order to increase the longevity of technical devices, the NaLi machine is put into standby mode during times of no data acquisition. This is usually done overnight or when long-standing hardware updates are performed on the experiment. The standby mode consists of shutting down lasers, power supplies and the cooling unit for the coils that generare the magnetic fields in the experiment. Furthermore we reduce the temperature of the oven, which reduces the flux of atoms and makes a refilling of the oven with new sodium and lithium less often necessary.

When we switch the experiment from standby into active mode, all devices are turned on and we perform basic optimization of parameters that are known to drift over time or to be very crucial for the performance of the experiment. Such parameters are for instance the coupling efficiency of optical fibers that transport various laser beams (MOT,repumper,imaging) from

the laser table to the position of the glass cell, as well as the level of the trap bottom [39, 41] of the magnetic trap which can require an adjustment of the MW evaporation ramp performed in the magnetic trap.

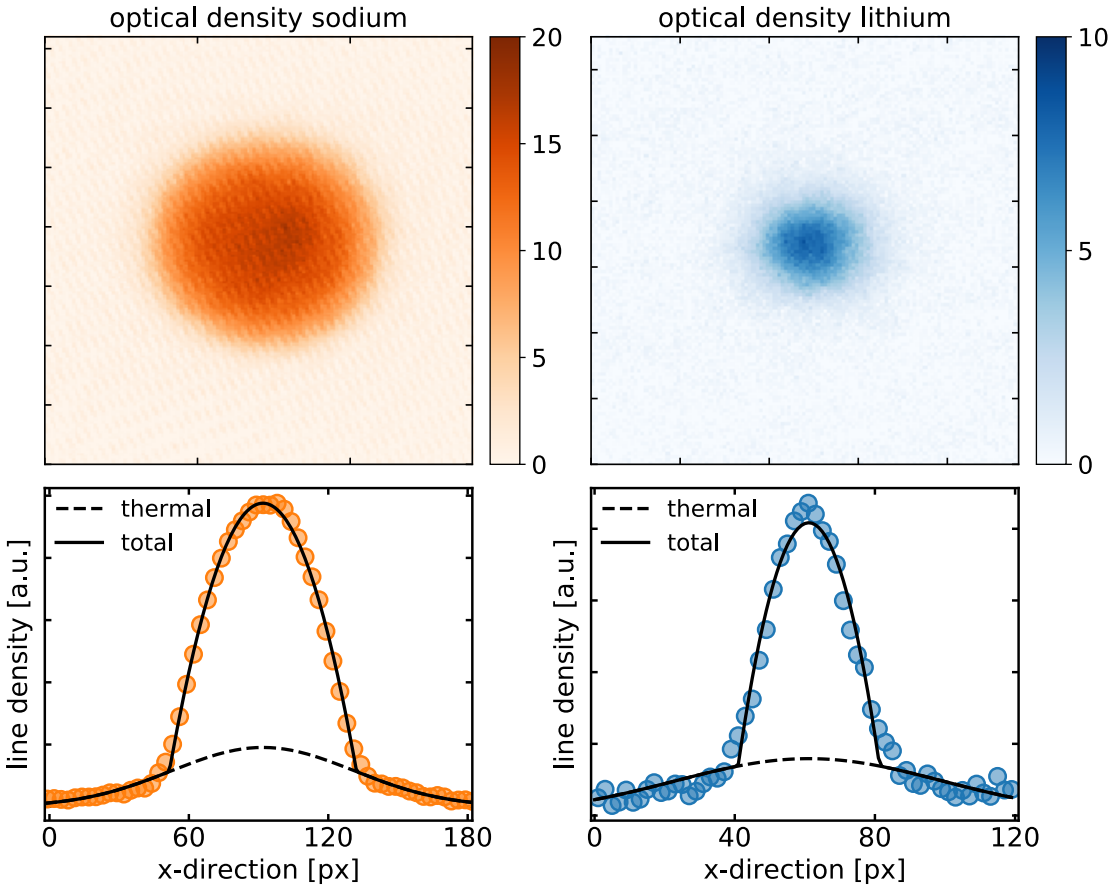

Figure 3.9.: **Time of flight absorption images (top) and corresponding integrated line profiles of sodium and lithium after the final evaporation in the ODT.** A time of flight of $3\,\mathrm{ms}$ for sodium and $2\,\mathrm{ms}$ for lithium was used. The images were recorded at the point in the sequence before the SCC experiments are initialized. Total atom number of each species is evaluated by integrating the signal in the region of the atomic cloud yielding 4.3×10^5 for sodium and 3.2×10^4 for lithium. The characteristic features of Bose-Einstein condensation can be seen in the bimodal distribution, which is qualitatively best seen in the line density. We apply a fit of a combined function of Gaussian profile and Thomas-Fermi profile to determine the condensate fraction η_{CF}, which yields 0.69 ± 0.01 for sodium and 0.56 ± 0.01 for lithium.

When performing this optimization we use the total atom number of sodium and lithium in the ODT as a figure of merit. The total atom number has empirically turned out to be a robust indicator for the performance of the experiment. Furthermore the atom numbers are straightforwardly determined from the absorption images. Fig. 3.9 shows typical TOF

	single realization in Fig. 3.9		set of 20 realizations	
	η_{CF}	T[K]	η_{CF}	T[K]
Sodium	0.69 ± 0.01	604 ± 7	0.62 ± 0.02	641 ± 12
Lithium	0.56 ± 0.01	594 ± 6	0.48 ± 0.02	626 ± 10

Table 3.2.: **Measured condensate fractions and resulting temperatures based on fitting a bimodal distribution.** The error from the single realization represents the uncertainty determined form the fitting routine, the error for the 20 realizations represents the statistical error, i.e. the standard error on the mean.

absorption images of sodium and lithium in the ODT after the final evaporation. The total atom number is evaluated using equation 3.3 and taking into account the experimentally determined magnification of the imaging system, see table 3.1. In the case of the data shown in Fig. 3.9 this yields 4.3×10^5 atoms for sodium and 3.2×10^4 atoms for lithium. We consider a total atom number for sodium in the range of (3-4.5)$\times10^5$ and for lithium in the range of (2-4)$\times10^4$ to be a sign for proper operation of the system. This range reflects the drifts in atom number that occur on the order of days/weeks and inbetween changes from standby and active mode of the experiment. During active data acquisition operation of the system which usually comprises hundrets of single experimental cycles in the course of multiple hours the atom number fluctuations are much smaller, see section 3.6.

In addition to the total atom number, we use the condensate fraction η_{CF} to benchmark the performance of the experiment. As described in section 2.1 the signature of Bose-Einstein condensation is the bimodal density distribution, which is seen in TOF images as well. In order to determine the condensate fraction we integrate the 2d absorption images along one axis and apply a fit to the data, see Fig. 3.9. The bimodal distribution that we use is a combined function of a gaussian profile and a Thomas-Fermi profile (see. section 2.1.2). The gaussian shape describes the thermal wings of the profile, while the Thomas-Fermi profile describes the narrow central peak corresponding to the atoms that are in the BEC phase. By determining η_{CF} we can infer the temperature of the system, see equation 2.4. The results for condensate fraction and temperature are summarized in table 3.2. In general, η_{CF} and T can be determined via a single experimental realization. However, the errors in that case represent the uncertainties that arise from fitting routines, in particular the uncertainty on the trap frequencies and the uncertainty on the condensate fraction as determined from the fit to the single realization. In order to assess the statistical uncertainty on the condensate fraction we evaluated a set of absorption images (total number of 20 shots) taken at the same experimental setting and determined the standard error on the mean. The results are shown in table 3.2.

It is important to note that the bimodal function we chose for the fitting routine is only an approximation that, for instance, does not take into account the interactions between the two species or the interactions between condensed part and thermal part within the same species.

This can also be seen in the fit to the lithium line profile in Fig. 3.9, where the transition between the two modes is poorly captured by the assumed bimodal distribution. Therefore a non negligible systematic error on the fit has to be expected.

Nonetheless, the condensate fraction provides a good measure for the stability of the experimental performance, because the qualitative difference between a partly condensed and a purely thermal cloud can be seen very clearly in a single experimental realization. Moreover, when the experimental parameters are tuned in accordance with hight condensate fraction this typically correlates with high total atom numbers as well.

3.5. Realizing heteronuclear spin-changing collisions

In section 3.2 we described the experimental sequence up until reaching Bose-Einstein condensation of sodium and lithium. From here we proceed with the measurements related to heteronuclear spin changing collisions (SCC). In the following subsections we provide a detailed description of the experimental setting and protocol which is used for realizing SCC. The timeline for a typical measurement is depicted in Fig. 3.10. After we have reached BECs of sodium and lithium we initiate the SCC dynamics by a superposition quench for sodium. Afterwards we let the system evolve for a given evolution time t_{evo}. For the state selective readout we apply a Stern Gerlach (SG) pulse [86] followed by TOF and absorption imaging.

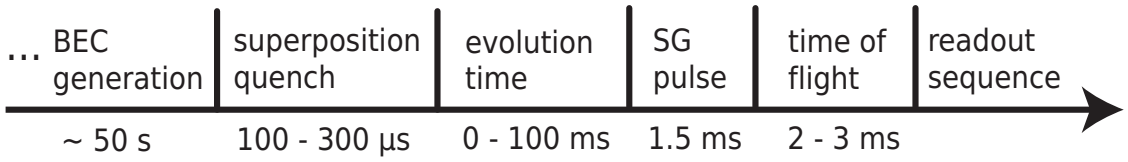

Figure 3.10.: **Timeline of a typical SCC sequence.**

3.5.1. Experimental setting

After the final evaporation in the ODT, both species occupy the $|1,1\rangle$ state[3]. The BECs are prepared at a specific magnetic offset field B. This field is ramped up after the atoms have been transferred from the magnetic trap to the waveguide. As will be shown in the following the initialization of spin changing collisions in our experiment involves internal state transitions between magnetically sensitive states. To perform those reliably, a magnetic offset field stabilitiy on the order of milliGauss is necessary. To ensure this stability we have established an active feedback stabilization based on a fluxgate sensor and a proportional–integral–derivative (PID) control loop. Details on experimental setup and performane of this stabilization is found in [42].

The value of the magnetic offset field B is usually in the range of 1.95 - 2.14 Gauss, which leads to a Zeeman splitting of the hyperfine groundstate according to the Breit-Rabi equation

[3]To describe internal states of atoms we use the following notation: $|F, m_F\rangle$, where F is the total atomic angular momentum quantum number, and m_F the corresponding magnetic quantum number [103]

[104] as shown in Fig. 3.11 and Fig. 3.12. B is chosen such that the energy splitting between

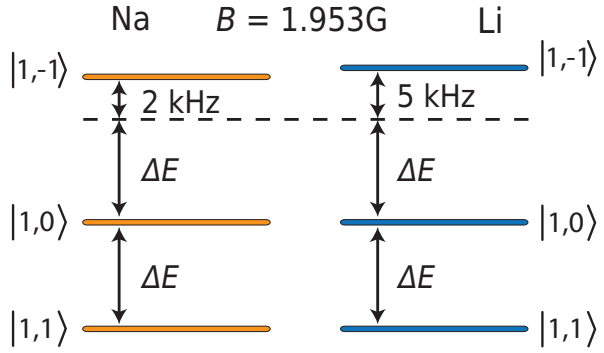

Figure 3.11.: **Level structure of sodium and lithium in a typical experimental setting.** Due to the applied magnetic offset field B the hyperfine ground state splits into three magnetic substates. In our experiments we tune B such that the energy splittings $\Delta E_{\mathrm{Na}} = (E_{\mathrm{Na},|1,1\rangle} - E_{\mathrm{Na},|1,0\rangle})$ and $\Delta E_{\mathrm{Li}} = (E_{\mathrm{Li},|1,1\rangle} - E_{\mathrm{Li},|1,0\rangle})$ are equal. According to the Breit-Rabi formula this equity is reached at B = 1.953G. This region is advantageous for our experiments as on the one hand it energetically enables SCC between the $|1,1\rangle$ and $|1,0\rangle$ states, while at the same time shifting the $|1,-1\rangle$ states out of resonance, allowing us to treat the system effectively as two two-level systems.

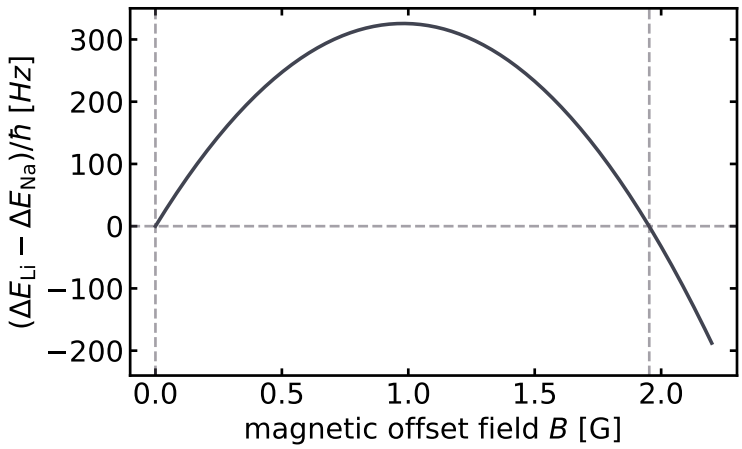

Figure 3.12.: **The difference in internal state energy splitting of the two species computed by the Breit-Rabi formula as a function of the magnetic offset field B.** The difference in energy splittings has two zero crossings, which indicate the magnetic offset fields B, at which SCC are energetically favourable. The first zero crossing is trivially at $B = 0$ G, where all three magnetically sensitive states are degenerate. The second crossing is at $B = 1.953$ G, which is the region in which we perform our SCC experiments.

the $|1,1\rangle$ and the $|1,0\rangle$ state of both species is identical, $\Delta E_{\mathrm{Na}} \approx \Delta E_{\mathrm{Li}}$ (at $B = 1.953$, the energy splitting is about $1.370\,\mathrm{MHz}$). At the same time the splittings between $|1,0\rangle$ and the $|1,-1\rangle$ states are detuned from ΔE_{Na} and ΔE_{Li} by a few kHz. This allows us to treat the hyperfine groundstate manifolds of sodium and lithium effectively as two two level systems, because the $|1,-1\rangle$ state is neither populated by any MW pulses during the initialization nor is it populated by the induced SCC dynamics due to aforementioned detuning.

3.5.2. Initializing spin dynamics

In order for spin exchange between sodium and lithium to occur by means of spin changing collisions it has to be energetically favourable (which is done by aforementioned tuning of the magnetic offset field). Moreover, the atoms before and after such a collision have to occupy m_F states that allow locally angular momentum conservation. Therefore, no spin dynamics are expected to happen while both species occupy the $|1,1\rangle$ state, because scattering into the energetically favourable $|1,0\rangle$ state requires the atom to loose one quantum of angular momentum which can not be absorbed by any scattering partner, see Fig. 3.13 top. In order to retrieve a clear signature for the spin changing collision process in the experiment, we use the following approach: Starting from the spin polarized state (both species occupy $|1,1\rangle$) we quench sodium into a superposition between $|1,1\rangle$ and $|1,0\rangle$ while keeping lithium in $|1,1\rangle$, hereby allowing the spin exchange process as shown in Fig. 3.13 bottom. After the quench we evaluate the state population of both species after some evolution time t_{evo} (up to $100\,\mathrm{ms}$). A clear signature for spin changing collisions between sodium and lithium is the appearance of lithium population in $|1,0\rangle$, as otherwise a direct transfer from $|1,1\rangle$ to $|1,0\rangle$ is supressed by the energy gap of $\Delta E_{\mathrm{Li}} \approx 1.37\,\mathrm{MHz}$, see Fig. 3.11.

3.5.3. Superposition quench

The initialization quench that renders sodium in a distinct superposition of $|1,1\rangle$ and $|1,0\rangle$ is done by applying a two-pulse microwave sequence, see Fig. 3.14. To make this superposition quench species dependent, the two-pulse sequence makes use of the different hyperfine splitting of sodium ($1772\,\mathrm{MHz}$) and lithium ($804\,\mathrm{MHz}$) [41]. First pulse of the sequence is of variable length τ_1 and is tuned to the transition of $|1,1\rangle$ to the intermediate state $|2,0\rangle$ of sodium. This pulse drives sodium population to the intermediate state with a Rabi frequency of $2\pi \times 2.5\,\mathrm{kHz}$. The second pulse is fixed to a length of $\tau_2 = 100\,\mu\mathrm{s}$, which corresponds to a π-pulse and subsequently drives the population from the intermediate state to $|1,0\rangle$. The total length of the pulse sequence is no longer than $300\,\mu\mathrm{s}$ and at least one order of magnitude shorter than the timescale which we observe the SCC dynamics on. Therefore we consider the superposition preparation as an instant quench that initializes the spin exchange.

3.5.4. State sensitive readout

For determining the exact sodium population imbalance which is generated by the initializing quench as well as for determining lithium spin transfer due to spin changing collisions, we rely on state sensitive detection by means of Stern Gerlach separation [86]. As described

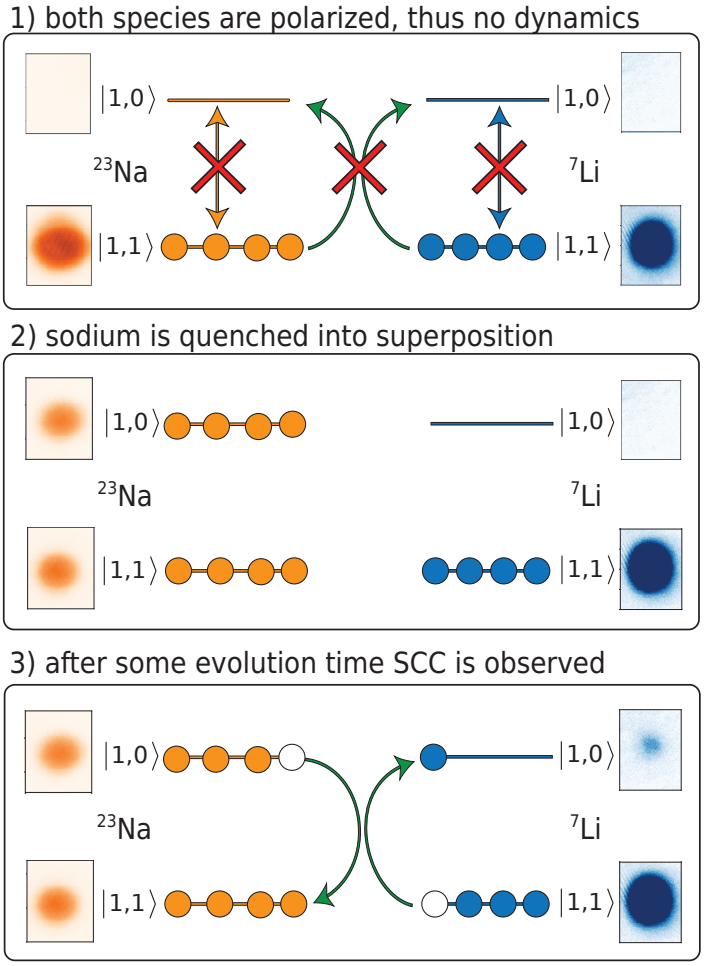

Figure 3.13.: **Illustration of the procedure for initializing spin changing collisions.** **1)** In the beginning both species are spin polarized, therefore no spin transfer is possible due to energy and angular momentum conservation. **2)** We apply a quench based on external MW radiation that creates a superposition in sodium while keeping the lithium state population unchanged. **3)** After the quench a heteronuclear spin exchange process is enabled, resulting in the emergence of lithium population in the $|0\rangle$ state after some evolution time t_{evo}. The inset absorption images were taken with time of flight and Stern Gerlach separation. The lithium spin transfer in the bottom absorption image was recorded with $t_{\mathrm{evo}} = 30\,\mathrm{ms}$.

above we initialize the spin dynamics by the superposition quench and let the system evolve for a given evolution time. Subsequently the trapping potential is switched off and a Stern Gerlach pulse is applied for $1.5\,\mathrm{ms}$, which is a strong magnetic field gradient. During the pulse atoms are accelerated according to the force F in gradient direction

$$F = -\mu \Delta B \,, \tag{3.17}$$

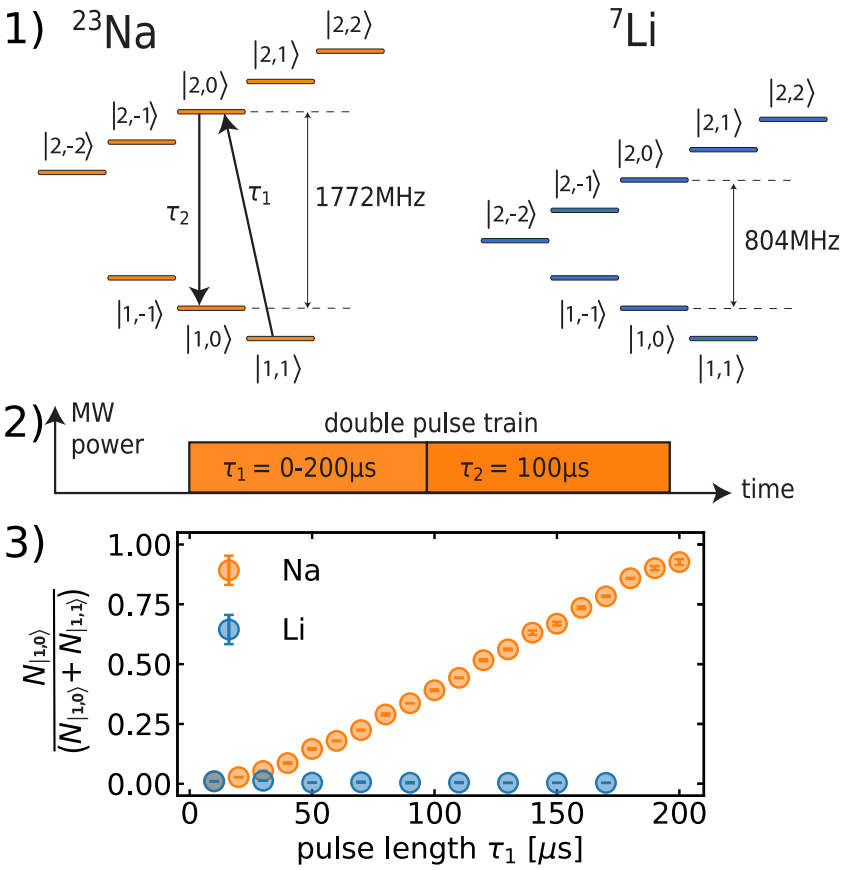

Figure 3.14.: **Implementation of the initialization quench. 1) Energy level scheme. 2) Double pulse sequence in time representation. 3) Relative state population of the $|1,0\rangle$ state as a function of the first pulse duration τ_1.** The quench is realized by two subsequent MW pulses. The first pulse is of variable duration τ_1 and tuned to $|1,1\rangle \rightarrow |2,0\rangle$ of sodium. This pulse drives population to $|2,0\rangle$ (200 µs corresponds to a π-pulse). The second pulse is tuned to $|2,0\rangle \rightarrow |1,0\rangle$ with a fixed duration of τ_2 = 100 µs (π-pulse) and drives the population from $|2,0\rangle$ to $|1,0\rangle$. Due to the different hyperfine splitting in sodium and lithium this scheme is only sensitive to sodium and does not affect the lithium state population. The graph in 3) is adapted from [36].

with μ being the magnetic moment, which is proportional to the magnetic quantum number m_F ($m_F \in \{-1, 0, 1\}$ in the case of the hyperfine groundstate manifold) and ΔB being the magnetic field gradient. The combination of SG pulse and TOF leads to a spatial separation of about 130 µm between the $|1,1\rangle$ and the $|1,0\rangle$ state, see Fig. 3.15. The absolut and relative state population is then determined by integrating the atomic signal in regions of interest which are spatially selected corresponding to the separated clouds. Table 3.3 defines the notation that is used in the following for the atom number corresponding to species and internal state.

	sodium	lithium
atom number in $\|1,1\rangle$	$N_{\mathrm{Na},1}$	$N_{\mathrm{Li},1}$
atom number in $\|1,0\rangle$	$N_{\mathrm{Na},0}$	$N_{\mathrm{Li},0}$
total atom number	$N_{\mathrm{Na,tot}}$	$N_{\mathrm{Li,tot}}$
initial state population ratio	$N_{\mathrm{Na},0}/N_{\mathrm{Na,tot}}(0)$ $\equiv \eta_0$	$N_{\mathrm{Li},0}/N_{\mathrm{Li,tot}}(0)$ $\equiv \mu_0$

Table 3.3.: **Notation for the atom number corresponding to species and internal state.** Since we performed almost all experiments with lithium initially spin polarized in $|1,1\rangle$, μ_0 is equal to zero most of the time. Note that in the other chapters the index notation N for sodium and L for lithium is used as well.

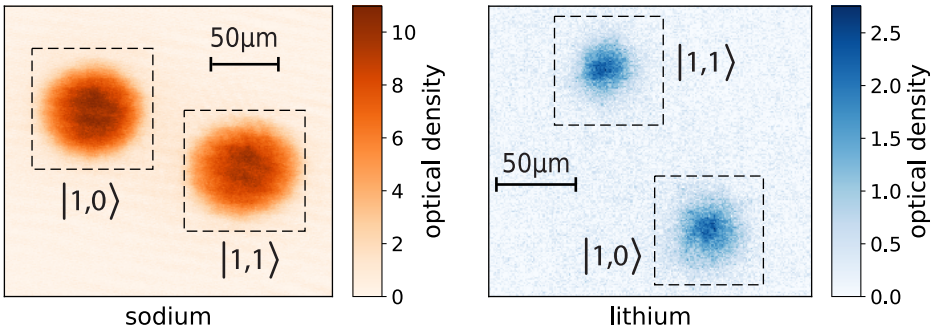

Figure 3.15.: **Absorption images of sodium (left) and lithium (right) after SG separation.** In this experimental cycle an equal superposition between the $|1,1\rangle$ and $|1,0\rangle$ state of sodium and lithium was generated by direct RF coupling. Before the imaging sequence a SG pulse ($1.5\,\mathrm{ms}$) and subsequent TOF ($3\,\mathrm{ms}$ for sodium, $2\,\mathrm{ms}$ for lithium) was applied. This leads to a clear spatial separation of about $130\,\mu\mathrm{m}$ between the two internal states. The relative population of the internal states is determined by integrating the signal in the regions of interest (dashed boxes). The different direction of separation which is visible in sodium and lithium stems from the different orientation of the cameras in the experiment.

3.6. Data acquisition and processing

The absorption imaging that we use is destructive, therefore a single experimental cycle has to be repeated multiple times to obtain a sufficient amount of data for quantitative analysis and comparison with theoretical model predictions. In the following we explain how we generate and analyse the datasets for our investigations.

3.6.1. Defringing of the absorption images for lithium

As mentioned in section 3.5.2 we aim to detect the population transfer of lithium from $|1,1\rangle$ to $|1,0\rangle$, with lithium being initially polarized in the $|1,1\rangle$ state. As shown in Fig. 3.15, we retrieve the information about state population by cropping a designated area in the absorption image and integrating the signal. As will be shown in the following sections, the lithium population transfer due to SCC amounts only to a few percent of the total lithium atom number. This can lead to low signal to noise ratio of the observable $N_{\mathrm{Li},0}$.

There are various sources of technical noise that are present in absorption images. One common source of noise is caused by interference fringes in the optical imaging system. Reflections of the imaging laser beam from the surfaces of optical elements are causing various interference patterns in the imaging path. These are detected by the camera as well and appear on the atomic picture as well as on the reference picture. This results in very typical imaging artifacts in the absorption images characterized by fringy patterns, see Fig. 3.16. It is

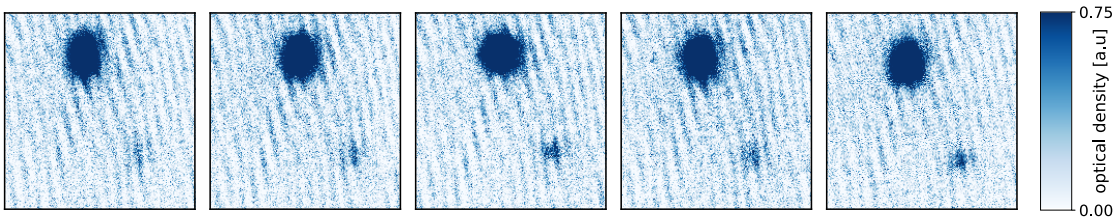

Figure 3.16.: **Absorption images of lithium selected from a large parameter scan dataset, highlighting the effects of interference fringes.** All five pictures were recorded with same parameter setting. One can see that the majority of atoms occupy the $|1,1\rangle$ state. Only about 5% of total atom number populate $|1,0\rangle$. In order to highlight the signal in $|1,0\rangle$, the colorcode was chosen accordingly. On this scale one can see the imaging artifacts due to interference patterns, manifesting as a periodic fringy pattern across the image. The amplitude of the artifacts is on the same order of magnitude as the atom signal in $|1,0\rangle$. About 50% out of all absorption images exhibit this effect.

important to note that not all interference patterns on atomic and reference picture will result in fringe patterns in the final absorption image. If these patterns are static, i.e. they appear with same phase and magnitude on the atom picture as well as on the reference picture then the effect of the fringes is compensated when using equation 3.3. However, if the fringes are fluctuating (caused for instance by vibrations in the experimental setup that translate onto the optical elements) and appear shifted in atomic and reference picture, they are incorrectly evaluated as atomic density signal in the absorption image. Since the time delay between atomic and reference picture in our experiment is $400\,\mathrm{ms}$, imaging artifacts due to moving interference fringes is a common issue in our data sets. About 50% of our absorption images do exhibit such fringe patterns.

In order to address the effects of these imaging artifacts in our lithium absorption images, we apply an idea which is presented in [105, 106] and which we are going to call “defringing” in the following. The method is based on imaging processing, in particular it exploits the

fact that the fringe patterns that appear in the experiment have very distinctive features that are recurring in the experiment. Therefore, when recording a large quantity of experimental shots back to back, the absorption images included in this extended dataset will contain all typical fringe patterns that can usually occur in the experiment. Technically, fringes in the absorption image appear, when the reference picture has a mismatched pattern compared to the atomic picture. The idea of the defringing method is to not use the reference picture $I_{\mathrm{ref},k}$ corresponding to k-th shot, but to use an individually constructed reference picture $I_{\mathrm{const},k}$, which is chosen to match best the individual fringe pattern present in the atomic picture $I_{\mathrm{atom},k}$. The conceptual steps for the defringing procedure are sketched in Fig. 3.17.

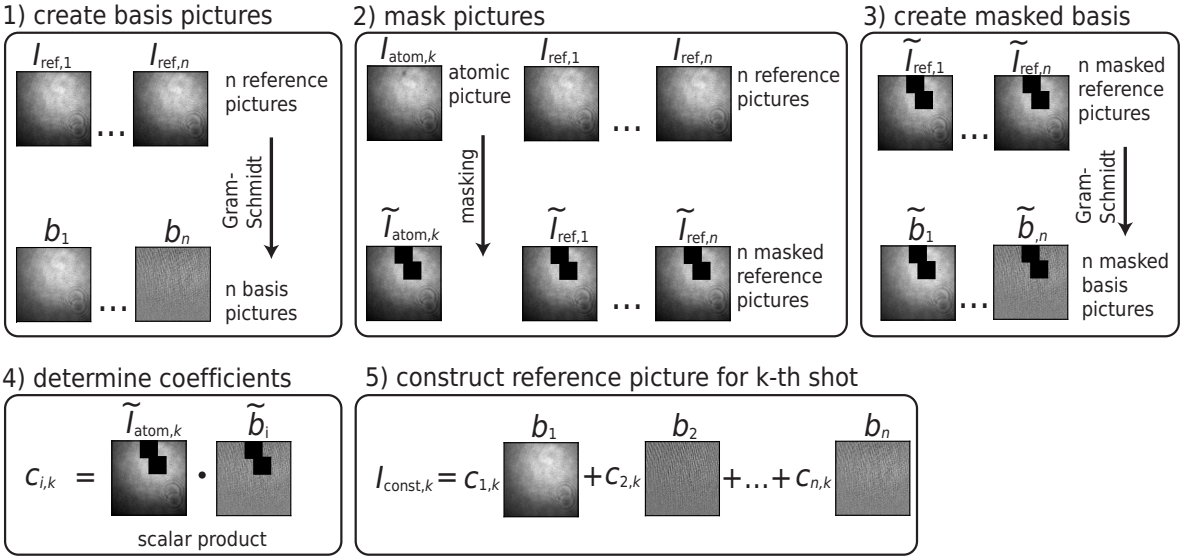

Figure 3.17.: **Sketch for illustrating the defringing procedure. 1)** We randomly select typically $n = 200$ reference pictures from a large dataset and apply the Gram-Schmidt method to create a basis. **2)** We mask an atomic picture and the n reference pictures, which is blacking out the regions where atomic signal is expected to appear. **3)** We create a masked basis analagous to the first step. **4)** We determine the coefficients for the basis expansion by projection of the masked basis pictures onto the atomic picture. **5)**We construct a new reference picture with matching fringe pattern to the atomic picture by expanding it in basis pictures with the appropriate coefficients.

First, we randomly select n reference pictures from a large dataset (usually we use $n = 200$, where the total number of shots is on the order of 300-500). We apply the Gram-Schmidt method [107] to those n reference pictures to construct n basis pictures b_i. These basis pictures form an orthogonal set and can be used to construct $I_{\mathrm{const},k}$ according to

$$I_{\mathrm{const},k} = \sum_{i=1}^{n} c_{i,k} b_i \ , \tag{3.18}$$

with $c_{i,k}$ being coefficients that have to be determined to best match the individual fringe pattern of k-th atomic picture.

Second, we select k-th atomic picture and mask the regions where atomic signal is expected to appear (in our case the crop regions for the $|1,1\rangle$ and $|1,0\rangle$ state). The same region is masked in the n reference pictures and the Gram-Schmidt method is applied to those to construct a masked basis $\tilde{b}_i$. The masked basis is used to determine the coefficients $c_{i,k}$ by projection onto the masked atomic picture $\tilde{I}_{\mathrm{atom},k}$ according to

$$c_{i,k} = \tilde{I}_{\mathrm{atom},k} \cdot \tilde{b}_i \ , \tag{3.19}$$

with $\cdot$ being the scalar product. The absorption image is then computed via 3.3 using $I_{\mathrm{atom},k}$ and $I_{\mathrm{const},k}$. Although the basis we choose with a typical size of $n = 200$ is much smaller than the amount of pixels in a masked image ($\sim 10^5$), it is yet sufficient to construct a proper reference picture due to aforementioned repetitive features of the fringe patterns.

The effect of using a "defringed" reference picture is demonstrated on a typical absorption image shown in Fig. 3.18. The absorption image of the same experimental shot is evaluated

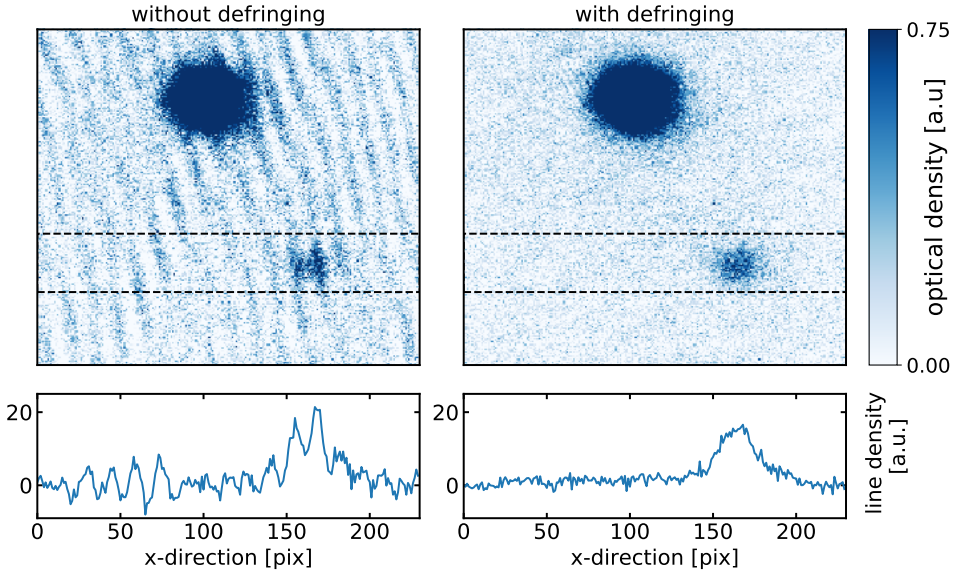

Figure 3.18.: **Demonstration of the effect of the defringing method on an absorption image.** The lithium absorption image of the same experimental shot is computed using the conventional (left) and the defringing method (right). The bottom panel shows the integrated signal of the region marked with the dashed lines. The decrease of the fringe pattern is clearly seen in the absorption image as well as in the integrated signal.

once using the conventional (not defringed) method and once with the defringing. Qualitatively, the effect of defringing is clearly seen in the absorption image as well as in the integrated signal. To quantitatively evaluate the effect of the defringing method, we select from the large dataset which is partially presented in Fig. 3.16, all shots that do not contain any atomic signal in $|1,0\rangle$ by definition ($t_{evo} = 0$). In this total of 58 shots we evaluate the

standard deviation of the atomic signal in the cropped region of $|1,0\rangle$. The standard deviation is reduced by 50% in the case of the defringing method compared to the not defringed one. We therefore apply the defringing method to the lithium data of all of our datasets. The method is applicable to the sodium data in an analogous way. The sodium pictures are about four times larger than the lithium ones. The way we implemented the defringing algorithm, however, led to the circumstance that the resources of a personal computer did not suffice to perform the defringing of the sodium data with the full sodium picture and a total number of basis pictures of n = 200. Since in our protocol the detection of $N_{\mathrm{Li},0}$ is the crucial part for investigating SCC, we applied the defringing solely to lithium and computed the absorption images for sodium with the conventional method.

3.6.2. Parameter scans

The usual way for generating useful datasets is to perform parameter scans, that is running the experimental cycle repeatedly, while a single parameter of the experiment is varied from shot to shot. The parameters of interest for investigating spin changing collisions are:

- the evolution time t_{evo} after the initialization quench
- the initial population ratio $N_{\mathrm{Na},0}/N_{\mathrm{Na,tot}}(0) \equiv \eta_0$ of sodium as set by the initialization quench
- the offset magnetic field B

From a technical point of view, the parameters t_{evo} and η_0 are most straightforwardly to scan. Variation of t_{evo} can directly be programmed into the experimental control sequence by changing one single time variable. η_0 is varied by changing the duration t_1 of the first pulse of the double pulse quench sequence, which again can be done by varying a single time variable. The setpoint for the offset magnetic field B is in principle controlled by a single variable as well. However, when scanning only B the linear Zeeman shift leads to a detuning in the MW pulses of the double pulse initialization, leading to a change in η_0. Therefore, isolating the scanning of B would require an adjustment of the double pulse parameters from shot to shot, which is rather involved, as our experimental control is designed to scan only one parameter at a time. We therefore refrain from scanning B directly and rather perform intensive scans of t_{evo} and η_0 at given B which we set manually inbetween the scans.

3.6.3. Data analysis of evolution time ($\mathrm{t_{evo}}$) parameter scans

The acquired information during one experimental cycle consists of the full set of timings and power levels which were used by the experimental control during this particular shot and the absorption images (set of three pictures per species) taken by the cameras. Each experimental cycle generates a hierarchical data format (HDF) file [108], where aforementioned information is stored. HDF allows for storage of large data and corresponding metadata and is our file format of choice for our analysis routines, which are written in Python. The HDF files are stored in folders corresponding to the day the data was taken on. The HDF files of parameter

scan measurements are tagged “scan_x_run_y”, with x being the number of the scan taken on that particular day in chronological order and y being the number of the single shot taken within particular scan in chronological order. First step of analyzing a scan measurement is

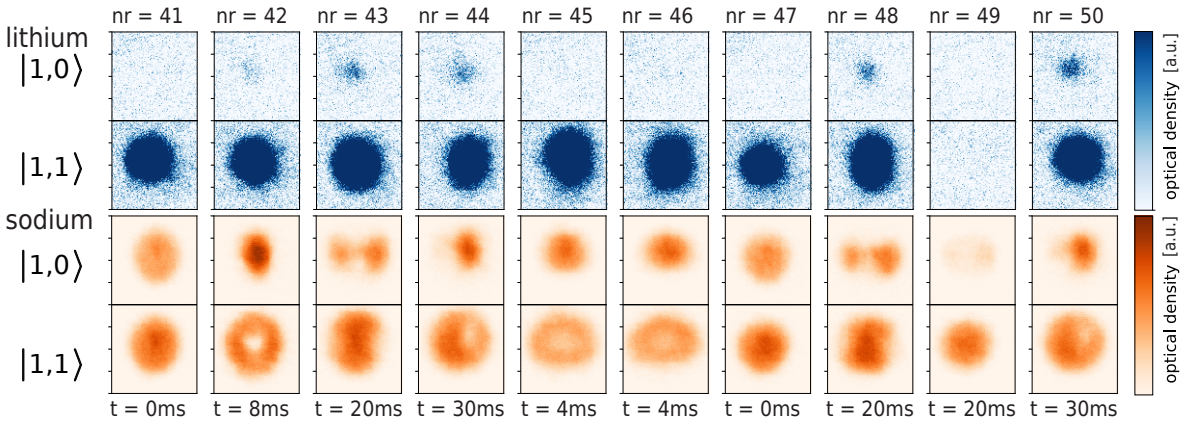

Figure 3.19.: **Segment of data display during the analysis routine of an t_{evo} parameter scan measurement.** For a first visual inspection of the absorption images, we crop the regions corresponding to the $|1,1\rangle$ and $|1,0\rangle$ state and plot them next to each other as a function of shot number within the scan. The scan consists of a total shot number of 483. The figure displays shot numbers 41 to 50. To avoid skewing of the data due to systematic drifts during the whole scan, the scan parameter is varied randomized. The value of t_{evo} of particular shot is displayed in the bottom line. The origin of the ring shaped distribution of sodium atoms in some shots is mentioned in the main text. The colorcode of the lithium optical density is chosen to emphasize the atom signal in $|1,0\rangle$ thus saturating the one in $|1,1\rangle$.

to evaluate the absorption images according to equation 3.3. We then select and crop out the regions of interest according to the atoms corresponding to the $|1,1\rangle$ and $|1,0\rangle$ state and display them next to each other, see Fig. 3.19 (in the following, if not stated otherwise we present data from the scan taken on 18.04.2019, with $B = 2.118\mathrm{G}$, $\eta_0 \approx 0.41$ and t_{evo} as the scanning parameter).

This display is particularly useful for a first visual inspection of the data. It allows to identify single outliers in the dataset due to experimental error. For instance, shot number 49 in Fig. 3.19 displays two characteristics that classify it as an outlier. Firstly, there is no atomic signal for lithium in any of the regions of interest, which indicates that in this shot lithium has been lost from the trap somewhere along the sequence. The loss of lithium atoms can have various reasons: insufficient loading in the MOT, inefficient transfer to the MT or the ODT, inefficient cooling of the atoms in one of the cooling stages. Such effects can occur due to transient malfunctions of one of the many components of the experimental apparaturs. Secondly, the sodium in shot 49 displays atomic signal in $|1,1\rangle$ as well as in the $|1,0\rangle$ state, yet the ratio of the initial internal state population η_0 is not consistent with the expected desired one of $\approx 41\%$. This means that the superposition quench has not been performed

correctly, either because the MW pulses were not applied properly or the magnetic offset field was not set properly, effectively detuning the transitions of the MW pulses.

From this initial visual inspection we empirically determine the typical characteristics of outliers that appear regularly in scan measurements. Those are small to vanishing total atom number in any of the species as well as a not properly initialized values for η_0. Based on these considerations we apply the following global postselection to the total set of data, see Fig. 3.20. We apply a total atom number threshold for sodium and lithium. All shots that exhibit total atom numbers below the threshold are disregarded for further analysis. Similarly we apply a threshold for sodium atoms in the $|1,0\rangle$ that filters the shots where a proper initial sodium superposition η_0 was not achieved (with respect to the desired value of η_0 which is chosen for the scan). We estimate an appropriate value for the threshold based on the total distribution of of atom numbers as displayed in the histrogramms in Fig. 3.20. In the case of the histogramm for the total sodium numbers (top right) and the sodium numbers in the $|1,0\rangle$ state (bottom right) one can clearly identify the distribution corresponding to regular shots (hight atom numbers, approxemately normal distributed, high frequency) and the distribution corresponding to the outliers (small atom numbers, low frequency and clearly separated from the distribution of regular shots). The threshold is in those cases chosen at a point that clearly marks a separation of those two distributions. In the case of the total lithium atom number histogramm (middle right) one does identify at one end the distribution of proper generated lithium clouds and at the other end the clearly outliers at zero. However, the distribution of proper operations is not as clearly normal as in the case of sodium and exhibits a long tail towards smaller atom numbers. In this case choosing an appropriate threshold is not as straightforward and to some degree heuristic. In this case cutting off the part of the long tail of smaller atom numbers is nonetheless important to ensure similar initial conditions.

After the postselection of the data set we perform the statistics evaluation, which is grouping the observables (internal state population) by scan parameter and evaluate mean and error on the mean. Fig. 3.21 displays this evaluation performed on the scan data from 18.04.2019.

One can clearly see an initial rise of $N_{\mathrm{Li},0}$ within the first $25\,\mathrm{ms}$ followed by damped oscillations. The appearance of $N_{\mathrm{Li},0}$ is a clear sign of heteronuclear spin changing collisions as explained in section 3.5. In the lithium data the spin transfer is clearly visible, however, in sodium the spin change due to SCC is not resolvable. First reason is that due to sodium having higher total atom number, the relative change in $N_{\mathrm{Na},0}/N_{\mathrm{Na,tot}}$ is about an order of magnitude lower than in $N_{\mathrm{Li},0}/N_{\mathrm{Li,tot}}$. The second reason is that there are other systematic effects that dominate the time evolution of the internal state population of sodium. For instance, we observe a loss of atoms from the $|1,0\rangle$ state as a function of time, clearly seen in the absolute as well as the relative state population. By fitting an exponential decay to the data we estimate the lifetime to be about $560\,\mathrm{ms}$ for the $|1,0\rangle$ state, while the $|1,1\rangle$ state remains stable on those timescales. The exact origin of the state dependent loss process is not fully resolved yet, however, we assume that it could be due to state sensitive loss processes or due to the external dynamics of the cloud in the trap, which is described in the following.

The superposition quench performed on sodium in addition induces characteristic spatial excitations of the individual sodium components in the dipole trap (due to the $|1,0\rangle$ and $|1,1\rangle$ state of sodium being immiscible, see section 4.2.4). These excitations result in characteristic density distributions (ring/hollow sphere and dumbell-like shapes) in the TOF images as seen,

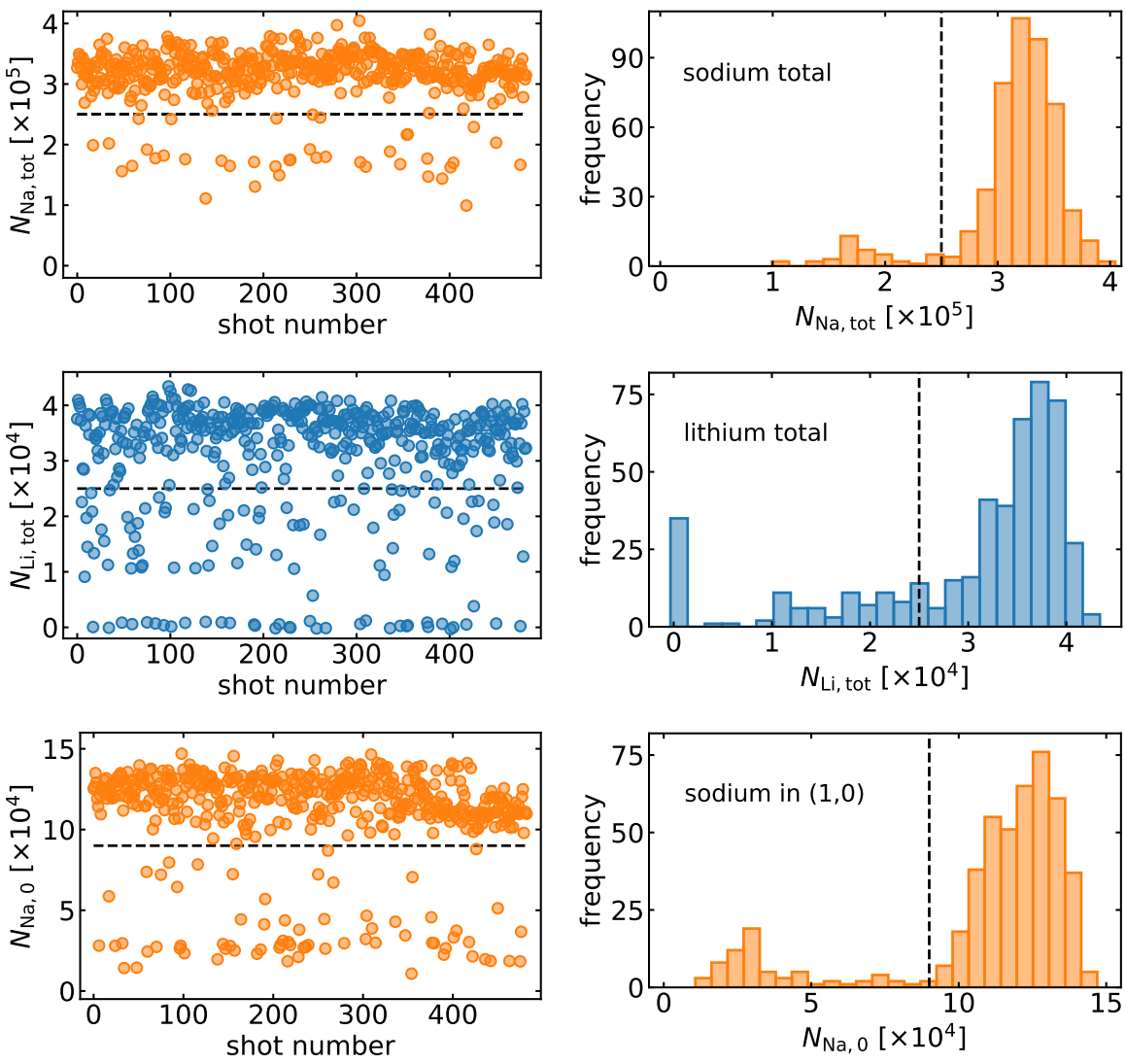

Figure 3.20.: **Postselection of a time evolution parameter scan. Observables of each experimental shot plotted in chronological order (left) and the corresponding histogramm of atom numbers (right).** Filters are applied to exclude outliers due to experimental error as well as to ensure similar initial condition with regard to total atom number. Common outliers are characterized by small to vanishing total atom numbers in lithium and sodium as well as an incorrect realization of η_0. The outliers are caused by transient malfunction of one or multiple components of the experimental setup. Circles represent the values of each individual shot, the dashed line marks the value of the threshold applied. The exact value of the threshold is chosen to separate the two distributions of normal operation and outliers, which is easily identified in the case of total sodium atom numbers (top right) and the sodium atom numbers in $|1,0\rangle$ (bottom right). The separation is not as straightforward in the case of total lithium atom numbers as the distribution exhibits a long tail towards smaller atom numbers.

for instance, in Fig. 3.22. In addition, our imaging system is systematically sensitive to these spatial dynamics. In Fig. 3.21 one can see a clear initial rise of $N_{\mathrm{Na},1}$, which appears to be an artifact, since the rise is correlated in time with the emergance of the spatial dynamics induced density shapes. This can be explained by systematically changing absorption imaging due to highly non uniform density distribution of the clouds. Further discussion and detailed comparison of the data to theoretical models is provided in the next chapter.

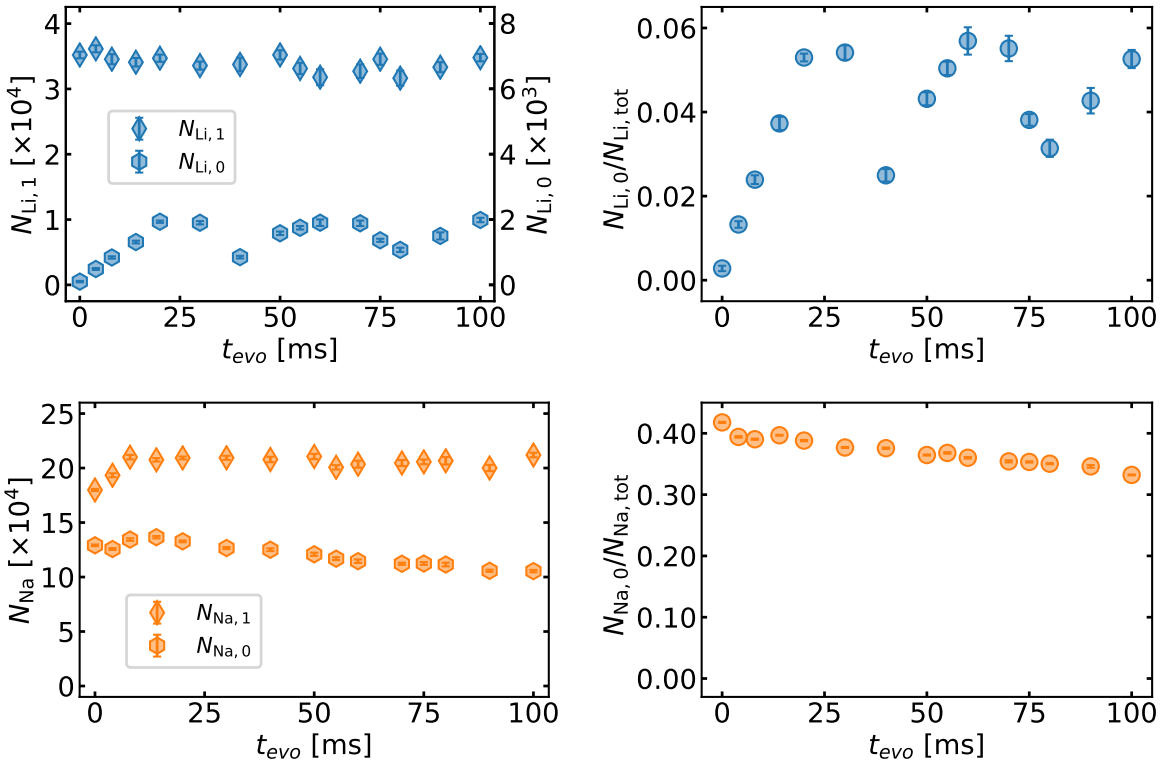

Figure 3.21.: **Qualitative display of internal state population of lithium (top) and sodium (bottom) as a function of the evolution time t_{evo}.** The absolute state population is shown on the left and the relative state population on the right. The appearance of $N_{\mathrm{Li},0}$ is a clear sign of SCC. The initial rise is on the order of $10\,\mathrm{ms}$ followed by damped oscillations. The maximum yield of lithium atoms in the $|1,0\rangle$ state is about 6% of the total lithium atoms. The corresponding change in $N_{\mathrm{Na},0}/N_{\mathrm{Na,tot}}$ due to SCC is not resolvable. Firstly, due to the higher sodium atom number the relative change is below 1%. Secondly, other effects (see text) are dominating the time evolution of $N_{\mathrm{Na},0}/N_{\mathrm{Na,tot}}$. Marker represent the mean and the errorbars the standard error on the mean.

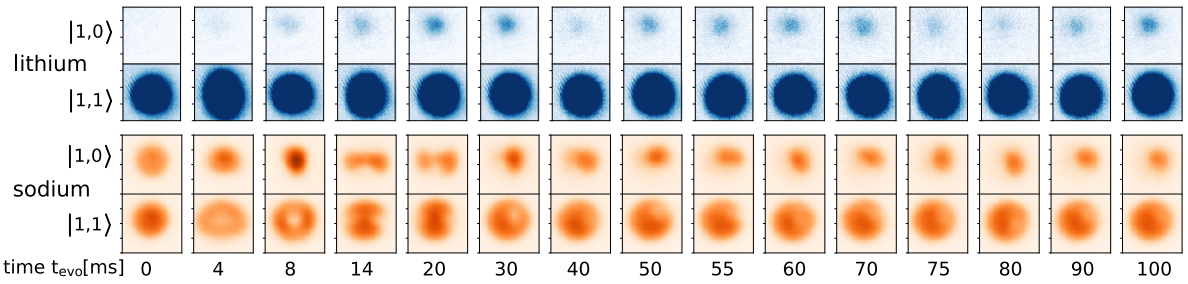

Figure 3.22.: **Averaged cropped density distributions as a function of t_{evo} for both species and respective internal states after time of flight. Data corrsponds to the data set shown in Fig. 3.21.** For lithium one observes an emergence of signal in the $|1,0\rangle$ state after a few tens of milliseconds. The colorbar cale for lithium has been chosen to make the signal in $|1,0\rangle$ visible by eye, accordingly the signal in $|1,1\rangle$ is saturated. The effect of spatial dynamics after the initialization quench is observed in the sodium images. On the order of a few milliseconds both components undergo oscillations of various shapes (ring,dumbell) after being damped out at later times.

3.6.4. Data analysis of initial sodium state population ratio (η_0) parameter scans

The data analysis of η_0 scans is analogous to time evolution scans with some exceptions which are mentioned here. The postselection in terms of total atom numbers for sodium and lithium is applied in the same way as for the t_{evo} scans. However, since the scanned parameter is the initial sodium population ratio, outliers related to incorrect superposition preparation can not be postselected by introducing a single global threshold but have to be excluded individually by visual inspection. Furthermore, the variation of η_0 is experimentally achieved by varying the duration τ_1 of the first MW pulse of the double pulse quench. The important properties of the MW pulses (duration, frequency, power) are experimentally realized with very low uncertainty compared to the uncertainties of other parameters in the experiment. However, due to uncertainties and shifts in the magnetic offset field which is applied in the experiment, shots performed at the same MW pulse durations do not result in the same value for η_0 (due to Zeeman-shift induced detuning in the transition). Therefore we perform the grouping of data by scan parameter in the following way (if not stated otherwise we present data from the scan taken on 25.04.2019, with $B = 2.118\mathrm{G}$, t_{evo} = 30 ms and η_0 as the scanning parameter in the following). We first evaluate the ratio $N_{\mathrm{Na},0}/N_{\mathrm{Na,tot}}$ for every single shot in the scan, see Fig. 3.23.

We then bin the data according to $N_{\mathrm{Na},0}/N_{\mathrm{Na,tot}}$ using 40 equidistant bins (resulting in bin size of 0.025). All superposition scans are performed for t_{evo} = 30 ms, which is small compared to the lifetime of the $|1,0\rangle$ state. Furthermore we know from the time evolution scans that the internal state transfer due to SCC in sodium is very small compared to the total atom number. We therefore approximate the initial sodium population ratio with the population ratio at t_{evo} = 30 ms, $\eta_0 \approx N_{\mathrm{Na},0}/N_{\mathrm{Na,tot}}(30\,\mathrm{ms})$.

The lithium observables are then grouped and displayed as a function of the binned scale

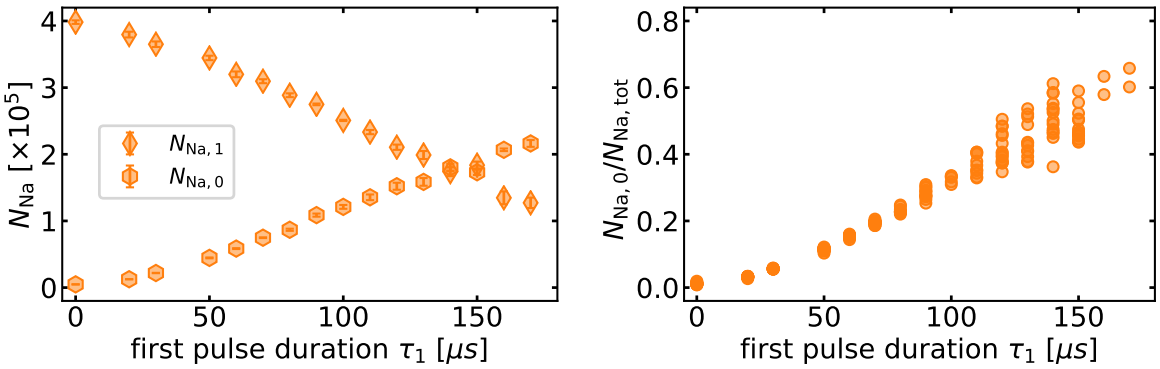

Figure 3.23.: **Sodium observables of an initial sodium population ratio (η_0) scan, absolute (left) and relative (right) population of internal states as a function of the first pulse duration, taken after (t_{evo} = 30 ms).** At longer times of τ_1 the data displays larger fluctuations, an indication of a fluctuating magnetic offset field B. We therefore bin the data by $N_{\mathrm{Na,0}}/N_{\mathrm{Na,tot}}$ and use this to determine the initial sodium population ratio by approximating $\eta_0 \approx N_{\mathrm{Na,0}}/N_{\mathrm{Na,tot}}$, which is then used as the x-axis for the lithium observables. Marker in the left figure represent the mean and the errorbars the standard error on the mean. Marker in the right figure represent single shot realizations.

η_0. Fig. 3.24 shows the analyzed data for a typical scan of initial sodium state population ratio. The characteristic feature seen in this data is a clear resonance of $N_{\mathrm{Li,0}}$ with respect to η_0. Furthermore, the resonance displays a characteristic asymmetry, with a very steep slope towards smaller values of η_0 and a less steep, tail-like behaviour towards higher η_0.

3.7. Summary

This chapter discussed the technical aspects of the experiment as well as the techniques and methods used to generate the data that is presented in this thesis.

We showed methods for the characterization of our experimental system. We demonstrated how we calibrate our absorption imaging procedure for determining total atom numbers for sodium and lithium. Typical experiments are performed with BECs containing about 3×10^5 (sodium) and 3.5×10^4 (lithium) atoms. To characterize the trapping potential of the optical dipole trap we excite spatial oscillations in the system and experimentally determine the trapping frequencies assuming a harmonic trapping potential.

We described the complete experimental cycle, mentioning the experimental sequence up until creation of a sodium and lithium BEC. We then went into detail and described the protocol for initializing and observing heteronuclear spin changing collision between sodium and lithium. This is done by having both species first spin polarized in the $|1,1\rangle$ state. A quench that renders sodium in a superposition between $|1,1\rangle$ and $|1,0\rangle$ initializes the spin dynamics. The clear signature for spin changing collisions is the subsequent appearance of lithium population in the $|1,0\rangle$ state which we detect using a combination of Stern-Gerlach

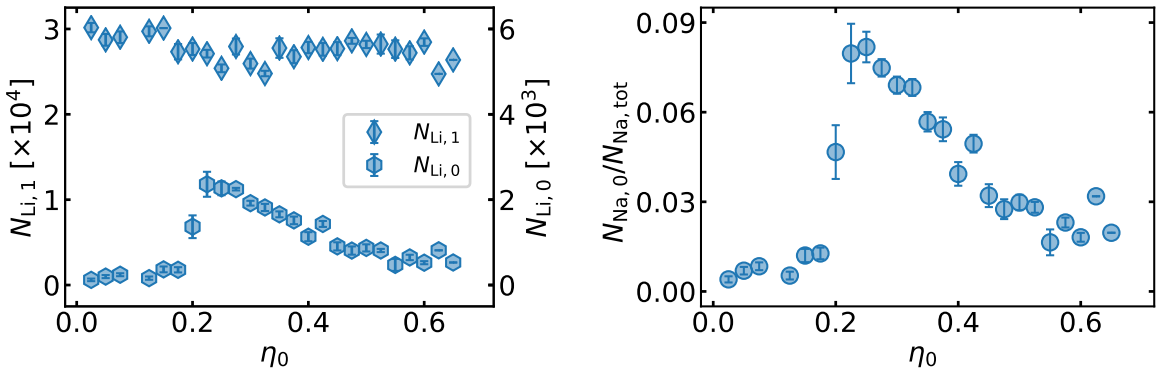

Figure 3.24.: **Lithium observables of an initial sodium population ratio (η_0) scan, absolute (left) and relative (right) population of internal states as a function of η_0, taken after (t_{evo} = 30 ms).** The SCC signal ($N_{\mathrm{Li},0}$) displays a clear resonance feature with an asymmetric shape which is characterized by a steep slope towards lower values of η_0 and a tail-like shape towards higher values of η_0. The maximum atom transfer to $|1,0\rangle$ amounts to about 8% of the total lithium atom number. Marker represent the mean and the errorbars the standard error on the mean.

separation and absorption imaging after time of flight.

Furthermore it was demonstrated how we generate large datasets. We do so by performing parameter scans, which is running the same experimental sequence repeatedly while changing one specific parameter from shot to shot. The parameters of interest for the investigation of spin changing collisions are the evolution time t_{evo} between initialization quench and readout, the initial sodium state population ration η_0 as set by the initializations quench, and the magnetic offset field B at which the SCC experiments are performed.

We showed how we postprocess the acquired data. We apply a defringing algorithm to the absorption images of lithium to reduce specific systematic noise on the absorption images caused by interference fringes in the optical imaging system. The observables of the experiments are the absolute and relative internal state population of sodium and lithium. We determine them by cropping the absorption images in the dedicated location of atomic signal after the Stern-Gerlach separation and integrating the atomic signal in those areas. In addition, we have to postselect the data of large parameter scans due to outliers in the data that are caused by malfunctions of the experimental system. Those outliers appear typically as strongly reduced atom numbers in any of the species and can easily be detected and excluded by threshold filters.

Typical data for parameter scans were presented. Scans of t_{evo} are characterized by an initial rise of $N_{\mathrm{Li},0}$ on the order of a few tens of seconds followed by oscillations which are damped. The maximum population transfer of lithium into the $|1,0\rangle$ state due to SCC amounts only to several percent of the total atom number. Scans of η_0 at fixed t_{evo} are characterized by an asymmetrical resonance feature with a steep edge at smaller η_0 and a tail like behaviour at larger η_0. Both scans provide clear evidence for heteronuclear spin changing collisions

between sodium and lithium.

4. Gauge invariance in ultracold atoms - the experimental building block

In chapter 2 we proposed a one dimensional $U(1)$ lattice gauge theory with bosonic matter. We have put forward a clear roadmap for the experimental implementation of this lattice gauge theory in cold atom mixture experiments. The cornerstone of this implementation is the elementary building block, see section 2.4.3 which entails degrees of freedom for both matter field and gauge field. Furthermore, the building block comprises all necessary gauge invariant interactions between matter field and gauge field and can therefore be considered as a minimal gauge theory with reduced dimensionality. Our proposed construction of an extended lattice gauge theory is based on repetitions of such building blocks.

In this chapter we show that our experimental system is a faithful representation of the building block model. To this end we study the characteristic dynamics that emerge in the framework of the building block. For this purpose we numerically solve the equations of motion resulting from Hamiltonian 2.76 in the mean field approximation. Our goal is to determine the distinct properties that characterize these dynamics in order to make qualitative and quantitative comparisons to the measurements we performed in our experiment. We therefore investigate the behaviour of the building block via the observable $N_\mathrm{p}/N = (L_{z,L} + L_L)/N_L = N_{L,0}/N_L$ and as a function of time, $L_{z,N}(0)/L_N$ and B, which is equivalent to the experimental parameters scans of t_evo, η_0 and B as introduced in section 3.6.2. For this study we make an ab initio estimate for the building block parameters (χ^th,λ^th and Δ^th) based only on experimental input parameters and wave-functions determined by imaginary-time propagation of the Gross-Pitaevskii equation corresponding to the full microscopic Hamiltonian.

After identifying the characteristics of the building block dynamics we compare these findings with our experimental measurements on heteronuclear spin changing collisions between sodium and lithium. In particular we made use of the high tunability of our experiment to study the dynamics and characteristic resonance features of spin changing collisions across a wide parameter range. We compare the experimental data to the building block dynamics in the mean field approximation and show that the resonance characteristics of spin changing collisions are perfectly described by this model and numerically determined, best fitting building block parameters.

We further find that the experimentally observed oscillations in the spin population are damped compared to the mean field prediction, however, show good agreement with the model when we incorporate a phenomenological damping term. The observed damping has various origins which we discuss in detail and address the effects that potentially compromise gauge invariant interaction and point out methods to overcome them.

The findings and data presented in this chapter are partly based on [36], however, in the current work updated calibration and data treatment routines were used, leading to slight variation of some numerical values. The theoretical framework of the building block has been mainly developed by T. V. Zache. The analysis of the experimental data, particularly the numericl determination of best fitting parameters has been performed by myself.

4.1. Mean field approximation of the building block

In this section we introduce the numerical mean field approach that we use to describe the experimental findings both qualitatively and quantitatively. Moreover, this profound theoretical model provides predictions in parameter regimes which have not been explored experimentally.

4.1.1. Mean field equations of motion

We start out with the building block Hamiltonian

$$H_{\mathrm{BB}}/\hbar = \chi \hat{L}_{z,N}^2 + \frac{\Delta}{2}\left(\hat{b}_{L,0}^\dagger \hat{b}_{L,0} - \hat{b}_{L,1}^\dagger \hat{b}_{L,1}\right) + \lambda\left(\hat{b}_{L,0}^\dagger \hat{L}_{-,N} \hat{b}_{L,1} + \hat{b}_{L,1}^\dagger \hat{L}_{+,N} \hat{b}_{L,0}\right) . \tag{4.1}$$

In particular we are going to demonstrate that this Hamiltonian is a faithful representation of our experimental system. For this purpose we solve the dynamics arising form H_{BB} in the mean field limit and compare them to our experimental findings. For convenience we first write the Hamiltonian in terms of spin components for both species

$$H_{\mathrm{BB}}/\hbar = \chi \hat{L}_{z,N}^2 + \Delta \hat{L}_{z,L} + 2\lambda\left(\hat{L}_{x,N}\hat{L}_{x,L} + \hat{L}_{y,N}\hat{L}_{y,L}\right) , \tag{4.2}$$

where we used the relations $\hat{L}_+ = \hat{L}_x + i\hat{L}_y$ and $\hat{L}_- = \hat{L}_x - i\hat{L}_y$. Note that we are using the Schwinger boson representation to relate the occupation number of the internal states of the atoms to spins via $\hat{L}_{z,s} = \frac{1}{2}(\hat{N}_{s,0} - \hat{N}_{s,1})$ with total spin length $L_s = N_s/2$, where $s \in \{N, L\}$.

In the next step we assume the mean field limit in which the spin operators are replaced by their expectation value[1] [73]. This is a reasonable approximation, since the total atom numbers in our BECs are in the order of 10^5 for sodium and 10^4 for lithium and quantum fluctuations can be neglected at high occupation numbers. We then compute the equations of motion for the spin components $L_{i,s}$ with $i \in \{x, y, z\}$ using the Ehrenfest theorem [109,

[1] We use the notation without ˆ to represent the expectation value of an operator

110]. This leads to the following set of coupled differential equations

$$\partial_t L_{x,N} = -2\chi L_{z,N} L_{y,N} + 2\lambda L_{z,N} L_{y,L} \ , \tag{4.3a}$$
$$\partial_t L_{y,N} = 2\chi L_{z,N} L_{x,N} - 2\lambda L_{z,N} L_{x,L} \ , \tag{4.3b}$$
$$\partial_t L_{z,N} = 2\lambda (L_{y,N} L_{x,L} - L_{x,N} L_{y,L}) \ , \tag{4.3c}$$
$$\partial_t L_{x,L} = -\Delta L_{y,L} + 2\lambda L_{z,L} L_{y,N} \ , \tag{4.3d}$$
$$\partial_t L_{y,L} = \Delta L_{x,L} - 2\lambda L_{z,L} L_{x,N} \ , \tag{4.3e}$$
$$\partial_t L_{z,L} = 2\lambda (L_{y,L} L_{x,N} - L_{x,L} L_{y,N}) \ . \tag{4.3f}$$

We solve this set of equations numerically for building block parameters that we determine by either making an ab initio estimate (see section 4.1.3) or by determining parameters that lead to best agreement with the experimental data (see section 4.2).

The initial conditions are chosen according to the settings we use in the experimental measurements i.e. $(L_{x,L}, L_{y,L}, L_{z,L})(t=0) = (0,0,-1) \times L_L$ and $(L_{x,N}, L_{y,N}, L_{z,N})(t=0) = (\cos\theta, 0, \sin\theta) \times L_N$, where $\theta \in [-\pi, \pi]$ is chosen in accordance to the quench that initiates the dynamics. We chose the observable $N_\mathrm{p}/N = (L_{z,L} + L_L)/N_L = N_{L,0}/N_L$ to characterize the resulting mean field building block dynamics, as it is the same observable we use in the experimental measurements.

4.1.2. Microscopic origin of the building block parameters

The dynamics that emerge from the equations in 4.3 genuinely depend on the building block parameters χ, Δ and λ. In fact, time dependent change in $L_{z,L}$ is only expected for a certain constrained parameter regime. To get a better understanding of how the building block relates to the cold atom system on a microscopic level, we recall the definitions of the building block parameters from section 2.4.2 and 2.4.3. The parameter λ is most straightforwardly to grasp from a microscopic point of view

$$\lambda = X^{\mathrm{SCC}} = g^{SCC} \int_{\mathbf{x}} \Phi^*_{N,1} \Phi^*_{L,1} \Phi_{N,0} \Phi_{L,0} \ . \tag{4.4}$$

What enters lambda is on the one hand the overlap integral between the sodium and lithium cloud and on the other hand the interaction strength g^{SCC}. The interaction strength is a fixed value for our experiments, since it is determined by the scattering length a^{SCC}, which we consider constant in the range of magnetic fields that we operate the experiments in, see table 2.1. The spatial modes of our atomic clouds are determined by many factors, but mainly by the trapping potential and the total atom numbers. Since those parameters are not actively scanned in our experiment, λ is generally considered a fixed parameter.

The parameter χ is similar to λ a combination of overlap integrals and interaction strengths

$$\chi = -\left[(X^N_{11} - X^N_{00}) + (X^L_{11} - X^L_{00}) + (X^{NL}_{11} - X^{NL}_{00})\right] = -\chi_N - \chi_L - \chi_{NL} \ . \tag{4.5}$$

In total six overlaps and interaction strengths enter into χ. By the same reasoning as in the case above, χ is considered to be fixed in the regime we operate our experiment in.

The parameter Δ includes the most contributions from different physical effects

$$\Delta = -\Bigg\{ \underbrace{\big(E_{L,1}(B_0) - E_{L,0}(B_0)\big) - \big(E_{N,1}(B_0) - E_{N,0}(B_0)\big)}_{\text{(I.)}} + \underbrace{\chi_L(\hat{N}_L - 1) - \chi_N(\hat{N}_N - 1) + \frac{1}{2}\chi_{NL}(\hat{N}_N - \hat{N}_L)}_{\text{(II.)}} + \underbrace{2M\left(-\chi_L - \frac{1}{2}\chi_{NL}\right)}_{\text{(III.)}} \Bigg\} . \tag{4.6}$$

The first term (I.) describes the relative difference in energy of the magnetically sensitive substates of both species due to the Zeeman effect. As described in section 3.5 this term approaches zero at an offset magnetic field of $B_0 \approx 2\mathrm{G}$. This term allows for very controlled tunability in the experiment. The second term (II.) contains the same overlap integrals as in the parameter χ. In addition this term scales with the total atom number of each species as well as the difference in total atom number. In general (II.) can be considered as a density or mean field shift that causes a detuning effect to the zero condition of the energy splitting in (I.). The last term (III.) scales with the magnetization $M = L_{z,N} + L_{z,L}$ which we can experimentally control very conveniently, since $L_{z,N} = \frac{1}{2}\left(N_{N,0} - N_{N,1}\right)$. Scanning the initial internal state population ratio of sodium η_0 corresponds to a scanning of term (III.). It is important to stress here that M depends on the initial internal state population ratio of lithium as well. However, we can treat it as a fixed offset here, since all experiments are initialized with $L_{z,L} = -N_L/2$. For convenience we rewrite the expression for Δ in equation 4.6 to point out that this parrameter has three contributions. One that can be considered a fixed value, one that is tunable in the experiment by varying the initial sodium state population and one that is as well tunable in the experiment and scales with the applied magnetic field offset

$$\begin{aligned} \Delta &= \Delta_0 + \Delta_L L_{z,N}(0)/L_N + \Delta_B(B - B_0)/B_0 \\ &= \Delta_0 + \Delta_L(2\eta_0 - 1) + \Delta_B(B - B_0)/B_0 \ , \end{aligned} \tag{4.7}$$

where Δ_0 describes the fixed offset contribution to D, Δ_L describes the contribution that scales with magnetization and Δ_B describes the contribution that scales with the applied magnetic offset field B. Here we have chosen $B_0 = 2.118\mathrm{G}$ for convenience.

We have examined the physical origin of the parameters that are contained in the building block Hamiltonian. In the next step we compute ab initio estimates for those parameters in a physically meaningful regime and investigate the ensuing dynamics resulting from those parameters using the equations of motion 4.3 derived in the previous section.

4.1.3. Ab initio estimates of building block parameters

In this section we determine building block parameters χ, Δ and λ that are reasonable for our system from a physical point of view. We will do a first principle estimation of the parameters,

that is making predictions based on a few experimental parameters of the system and not relying on the actual spin changing collisions measurements.

The main task of this estimation is to determine the density distributions of the two species from which the overlap integrals are computed. They enter into the three parameters in equations 4.4 - 4.6. In situ images of the clouds, which are in principle a direct measurement of the projected density distribution are in our case not reliable with our usual absorption imaging procedure. The high peak densities due to high atom numbers and strong confinement lead to opaqueness of the cloud to the resonant light beam and inhibit quantitative evaluation of the cloud, even for imaging intensities much higher than I_0^{sat}. We therefore rely on measurements which are performed in TOF, which our imaging procedure is optimized to.

We determine the density distribution of the sodium and lihtium cloud by computing the ground state wavefunction by imaginary-time propagation[111–113] of the Gross-Pitaevskii equation 2.1.2 corresponding to the full microscopic Hamiltonian 2.40. As experimental input parameter we use the experimentally determined trapping frequencies 3.13-3.16 and the total atom numbers for sodium and lithium $N_N = 300 \times 10^3$ and $N_L = 35 \times 10^3$. The trap frequencies are used to determine the external trapping potential. The total atom numbers are used for the normalization condition for the wavefunction. As the initial guess for the iteration of the wavefunctions we choose the Thomas Fermi profile for sodium and lithium i.e. we consider homonuclear interactions and disregard heteronuclear interactions. For a starting point this is a reasonable assumption as it provides a profile in the right order of magnitude. However, as it will be shown the interaction between sodium and lithium has a major influence on the exact density profile of both clouds and the resulting overlap integrals. In Fig. 4.1 we show results of the imaginary time propagation. The colorplots represent the predicted column density for sodium and lithium projected on the respective spatial direction. For this simulation we used the following numerical parameters. We used a three dimensional grid with $(256, 256, 128)$ grid points along the (x, y, z) directions. The spacing between two grid points corresponds to a physical length of $0.15\,\mu\mathrm{m}$. The reduced grid points along the z direction accounts for the stronger confinement in this direction and the subsequently smaller spatial extent of the clouds in this direction. As a convergence criterion we chose a relative change below 1×10^{-5} for the chemical potential of sodium and lithium between two consecutive iterations. The simulation corresponding to the data shown in Fig. 4.1 converged at a chemical potential of $\mu_N/h = 5263\,\mathrm{Hz}$ for sodium and $\mu_L/h = 3739\,\mathrm{Hz}$ for lithium.

The characteristic feature that is seen from those profiles is that the interactions between sodium and lithium cause the clouds to repell each other resulting in an indent in the sodium distribution at the position of the lithium cloud. Furthermore, the lithium cloud is pushed away by the sodium resulting in an upshift of the lithium cloud against gravity direction. Even though the peak density of the ground state wavefunctions of the individual species is slightly higher compared to the Thomas Fermi case, the overlap between sodium and lithium is smaller due to the displacement of both clouds.

The line plots in Fig. 4.2 are the corresponding integrated signal of the column densities. Solid lines are the results of the imaginary time propagation, dashed lines correspond to the Thomas Fermi profiles which were used as the initial profiles for the iteration. Having determined the density distributions of sodium and lithium, the corresponding overlap integrals are computed numerically. From those we compute the following ab initio building block

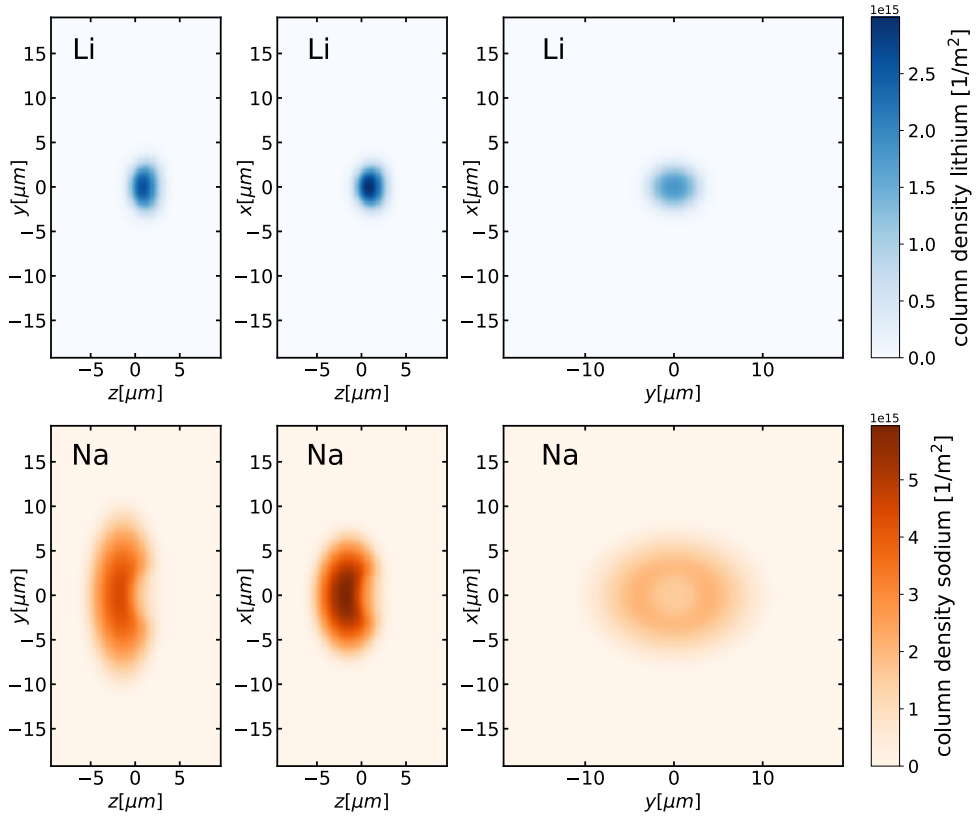

Figure 4.1.: **Column densities of lithium (top) and sodium (bottom) determined from imaginary time propagation of the Gross-Pitaevskii equation.** As experimental input parameters we used $N_N = 300 \times 10^3$ and $N_L = 35 \times 10^3$ and the trapping frequencies determined in section 3.4.1. As initial start wavefunction we used Thomas Fermi profiles of the individual species (disregarding heteronuclear interactions). Further details regarding the numerical methods are described in the main text. The most distinct feature that is seen in the trapped mixture is the repulsive interaction between the two species. This results in a density indent of sodium around the position of the lithium cloud. Moreover, the lithium cloud is pushed significantly upwards against gravity compared to its trapping potential center position.

parameters

$$\chi^{\mathrm{th}} = 20.88\ \mathrm{mHz} \tag{4.8a}$$
$$\lambda^{\mathrm{th}} = 57.7\ \mu\mathrm{Hz} \tag{4.8b}$$
$$\Delta_0^{\mathrm{th}} = -75.2\ \mathrm{Hz} \tag{4.8c}$$
$$\Delta_L^{\mathrm{th}} = 6.324\ \mathrm{kHz} \tag{4.8d}$$
$$\Delta_B^{\mathrm{th}} = -1.669\,\mathrm{kHz}\ . \tag{4.8e}$$

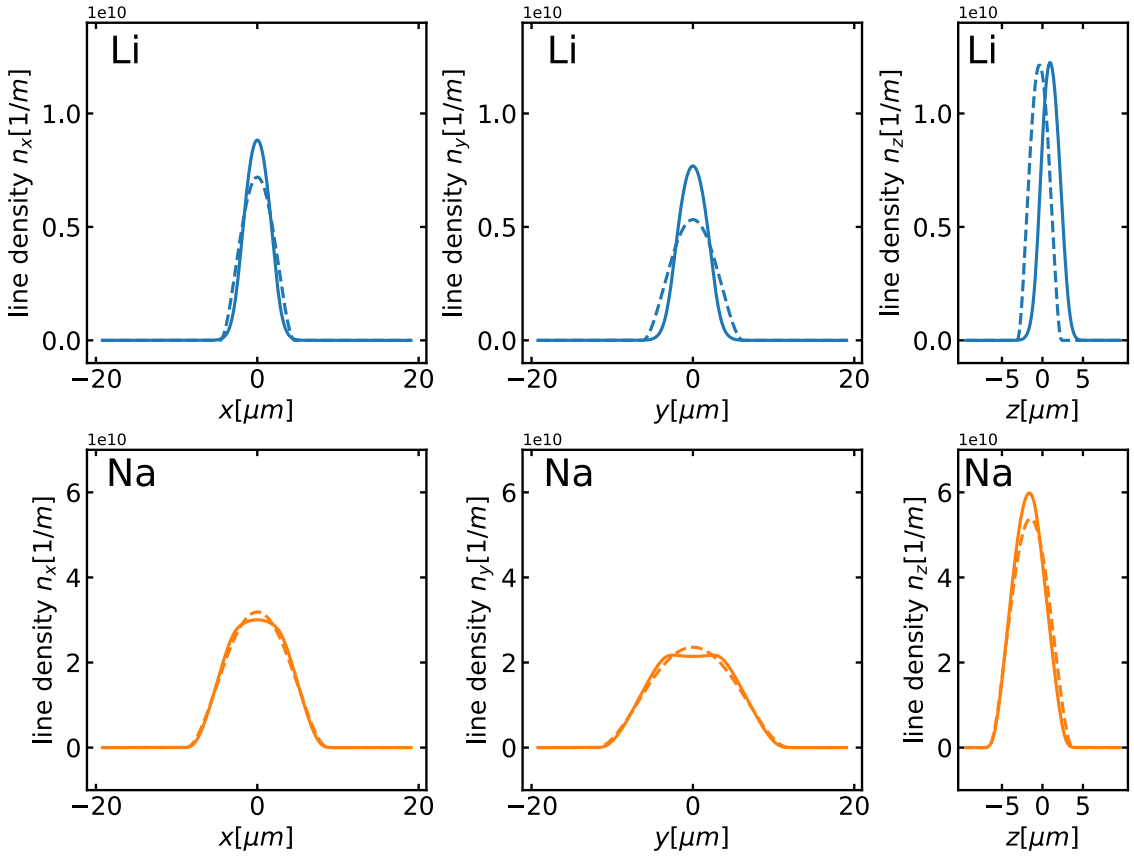

Figure 4.2.: **Line densities of lithium (top) and sodium (bottom) corresponding to the numerical data shown in Fig. 4.1**. Dashed lines corespond to the line profiles of the Thomas Fermi profiles that were used as the initial start wavefunction for the imaginary time propagation.

The parameter Δ_B^{th} is calculated by linearizing the energy difference $\Delta E_L - \Delta E_N$ as a function of the magnetic offset field B around $B_0 = 2.118\mathrm{G}$, see Fig. 3.12.

4.1.4. Building block dynamics from ab initio estimates

We numerically solve the equations of motion 4.3 with parameters 4.8. The initial conditions are chosen according to the settings we use in the experimental measurements i.e. $(L_{x,L}, L_{y,L}, L_{z,L})(t=0) = (0,0,-1) \times L_L$ and $(L_{x,N}, L_{y,N}, L_{z,N})(t=0) = (\cos\theta, 0, \sin\theta) \times L_N$, where $\theta \in [-\pi, \pi]$ is chosen in accordance to the quench that initiates the dynamics. We chose the observable $N_{\mathrm{p}}/N = (L_{z,L} + L_L)/N_L$ to characterize the resulting mean field building block dynamics, as it is the observable we use in the experimental measurements.

Time evolution

In Fig. 4.3 we display the time evolution of N_{p}/N for various values of η_0 ranging over the full span of tunability. For convenience we chose $B = B_0$ to not take into account the magnetic

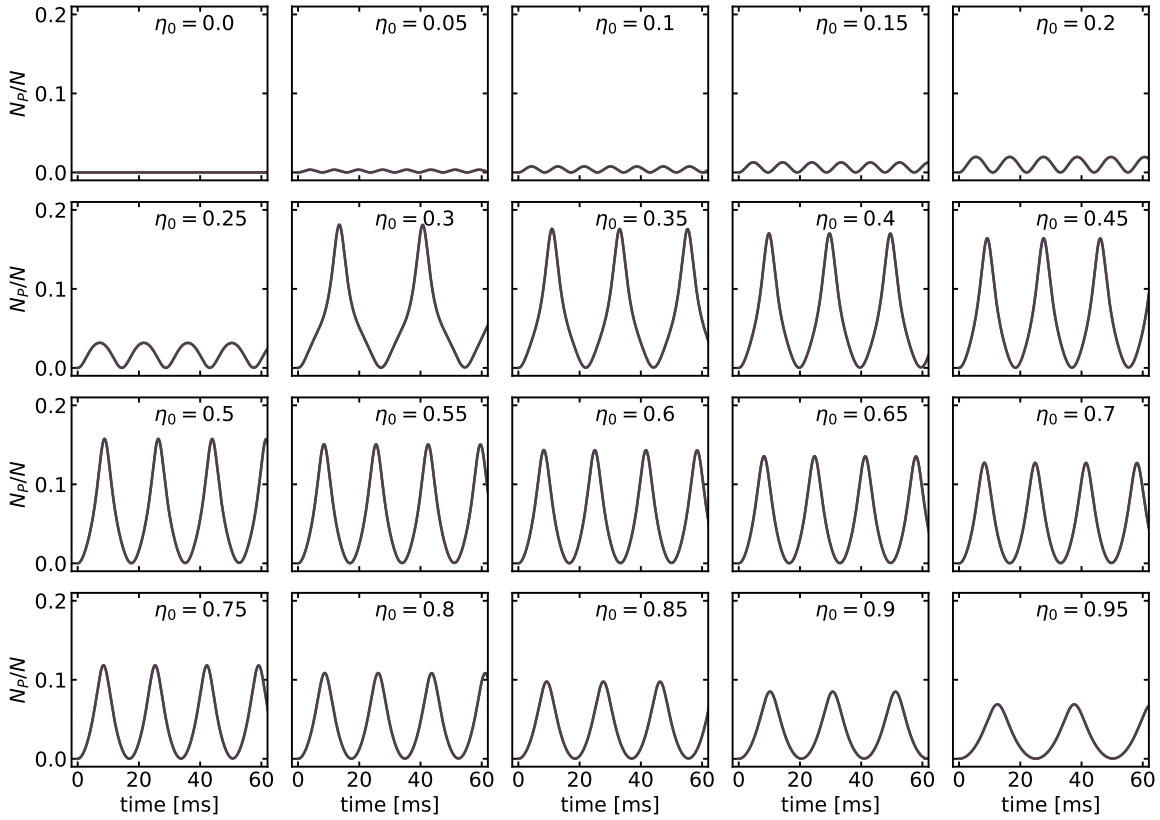

Figure 4.3.: **Mean field building block dynamics of observable N_p/N for various values of η_0.** The time evolution of N_p/N resulting from numerically solving equations 4.3 with the ab initio estimates of the building block parameters 4.8. The used magnetic offset field is $B = B_0 = 2.118$ G. The time dependence is characterized by non harmonic oscillations with frequency and amplitude strongly depending on η_0, whereby the amplitude is zero at the extrema of η_0. As a function of η_0, the oscillations display a discontinuity in the region between $\eta_0 = 0.25$ and $\eta_0 = 0.3$, resulting in a sudden change of amplitude, frequency and the functional shape of the oscillations.

field dependence yet. The time dynamics of N_p/N are characterized by clearly non-harmonic oscillations with varying period and amplitude, which depend strongly on η_0. The timescale of the oscillations is tens of milliseconds. The amplitude is vanishing when η_0 approaches zero, and has a maximum value of about 0.18 at $\eta_0 \approx 0.3$. As a function of η_0, the oscillations display a very characteristic resonance feature. This feature is characterized by a sudden functional change of the oscillations when reaching a critical value of $\eta_0 = \eta_\mathrm{crit} \approx 0.27$, see Fig. 4.4 and 4.5. Below η_crit the oscillations are of low amplitude and increase in amplitude and decrease in frequency with increasing η_0. When crossing η_crit a discontinuity occurs which is reflected in a sudden increase of amplitude, a sudden decrease of frequency, and a change of the functional shape of the oscillations. For further increasing values of η_0 the oscillations continue to gradually decrease in amplitude.

Resonance

We visualize the resonance behaviour in Fig. 4.4 by displaying the amplitude as a function of η_0. Clearly seen is the asymmetric shape of the resonance with a steep edge around $\eta_{\mathrm{crit}} \approx 0.27$

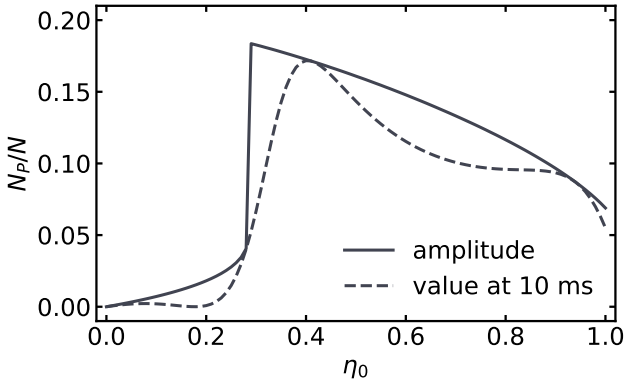

Figure 4.4.: **Maximum amplitude of N_{p}/N as a function of η_0.** The parameter settings are equivalent to the ones in Fig. 4.3. A clear resonance features is seen characterized by a discontinuity around $\eta_0 = \eta_{\mathrm{crit}} \approx 0.27$ where a sudden change in amplitude occurs. In addition the curve is shown where instead of the amplitude, the value of N_{p}/N at a fixed time of $10\,\mathrm{ms}$ is recorded with the idea to sample the maximum of the first fringe. This curve is only an approximation to the exact amplitude curve, since the maximum of the first fringe moves in time due to the frequency varying as a function of η_0. Nonetheless, this approximation captures all important qualitative and to a degree the qualitative features of the resonance. Since the method of sampling a single point at a fixed time is much less ressource heavy, it is the method used to generate the experimental resonance data.

and a long tail towards higher values of η_0. In addition to displaying the amplitude of the oscillations we display the value of N_{p}/N that is reached after $10\,\mathrm{ms}$. The idea is to sample the resonance by measuring the maximum of the first oscillation. As expected, this method is only an approximation to the exact resonance, since the maximum value of the first oscillation varies due to the frequency change that is associated with varying η_0. The advantage of only sampling a maximum point lies in the great reduction of necessary resources, since only a single point has to be recorded compared to sampling at least one whole fringe. For the numerical simulation of the dynamics this effect is negligible, however, for the experimental measurements it makes a significant difference, since about an order of magnitude more data acquisition would have been necessary. Therefore, we sampled the oscillations only at one point tor record the resonance data.

In Fig. 4.5 we visualize the behaviour of N_{p}/N around η_{crit} by displaying the same dynamics as shown in Fig. 4.3 but now for values of η_0 around the critical value. In this "zoom-in" the non harmonicity of the oscillations becomes most apparent and the discontinuity at this point is clearly seen as a sharp spike that emerges out of the flat oscillations at smaller values of η_0. The origin of the discontinuity is a strict consequence of the nonlinear coupling that is an

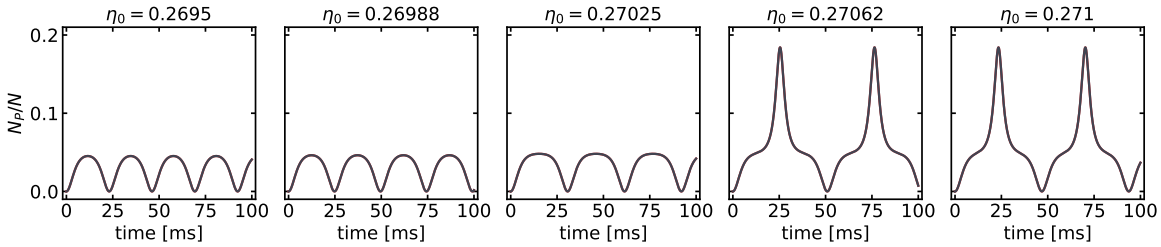

Figure 4.5.: **"Zoom-in" of Fig. 4.3 around $\eta_0 = \eta_{\mathrm{crit}}$.** The smaller step size of η_0 reveals the exact changes associated with the discontinuity. At this level the non harmonicity of the oscillations is clearly seen.

inherent feature of the building block Hamiltonian. For more detailed information and an alternative interpretation of this discontinuity the interested reader is referred to [43].

Resonance behaviour as a function of B

So far we have considered the dynamics and resonance features of the building block at a fixed magnetic field of $B = 2.118\mathrm{G}$. However, the magnetic offset field offers another convenient way for experimental tunability via the term $\Delta_B(B - B_0)/B_0$ that enters in Δ. To show the depenence of the magnetic field on the building block dynamics, we evaluate the resonance as in Fig. 4.4 for various magnetic offset fields B. The plots are shown in Fig. 4.6. Around $B = B_0$ a change in mangetic field causes the resonance to shift. Reducing B results in a shift of η_{crit} towards smaller values and increasing B results in a shift of η_{crit} towards higher values. When the magnetic field is tuned sufficiently far from B_0, i.e. $B_0 - B \approx 400\mathrm{G}$ or $B - B_0 \approx 250\mathrm{G}$, the signal of N_{p}/N is vanishing for all possible values of η_0.

The reduction of N_{p}/N as a function of B can easily be understood on a microscopic level. Tuning B results in variation of the energy splitting of the atomic levels via the Zeeman effect. Therefore, a B value that is tuned sufficiently far from B_0 results in supressing the spin changing collisions, as it adds an energy penalty to the process.

4.1.5. Summary

In this section we have established a theoretical model that describes the building block dynamics in the mean field limit. We studied the emerging dynamics of this system across a wide range of parameters which are available in the experiment as well. We found that the system shows very distinct features of which the most prominent one is a discontinuity in the functional behaviour of the temporal oscillations of the observable N_{p}/N. These characteristic signatures will allow to identify our experimental measurements as a faithful implementation of the building block.

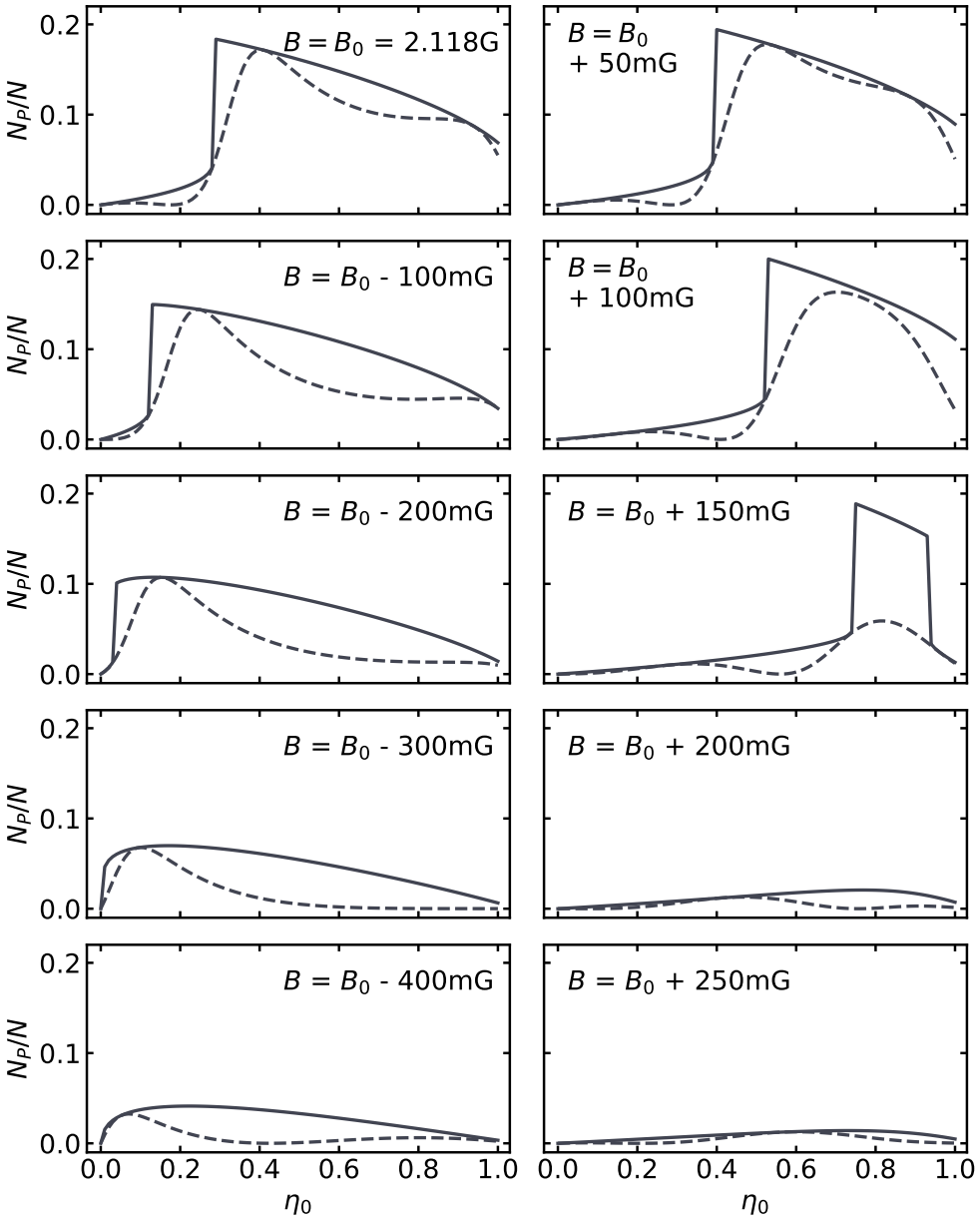

Figure 4.6.: **Maximum amplitude of N_p/N as a function of η_0 for various magnetic offset fields B.** The individual resonance curves are plotted analogously to Fig. 4.4. The left column shows decreasing B from top to bottom, the right column shows increasing B from top to bottom. Varying of B results in a continuous shift of the position of the discontinuity η_crit. The peak of N_p/N vanishes when B is reduced to about $B_0 - 400$ mG and when B is increased to $B_0 + 200$ mG. In terms of varying B, the resonance shows asymmetric behavour as well since the reduction in amplitude is gradually when reducing B and sharper when increasing B.

4.2. Experimental measurements

In the previous section we studied the dynamics that emerge from the building block in the mean field approximation and we have identified distinct features that characterize these dynamics. In this section we will show that these features are found in our experimental measurements as well, clearly identifying it as an experimental realization of a building block.

We first present time evolution data and introduce a formalism that can be implemented into the equations 4.3 to account for the reduced visibility of the oscillations in the experimental data. Using this method we numerically determine best fitting building block parameter that remarkably describe the experimental data.

We then show that the determined building block parameter are consistent with experimental resonance data that were recorded at the same magnetic offset field B. Our recorded resonance data display all characteristic features of the building block dynamics as a function of both η_0 and B. To emphasize even more the agreement between building block and experimental resonance data we find building block parameter that perfectly describe the resonance data even without the necessity to account for experimental visibility loss of the oscillations. This is possible due to the resonance data being insensitive to the experimental visibility loss.

We compare the building block parameter that we determine via ab initio estimation in section 4.1.3 and via fitting to the experimental data. We discuss the potential sources that lead to deviation between the two parameter sets as well as sources that lead to the experimental visibility loss of the oscillations.

4.2.1. Experimental time evolution measurements

We have recorded a total of three time evolution datasets at a magnetic offset field of $B = B_0 = 2.118$ G. The data sets are tagged by the date they were recorded on. The data sets from 18.04.2019 and 23.04.2019 were recorded with considerably long time inbetween, during which the experiment was turned into standby mode. Nonetheless the experimental benchmark values for the performance of the experiment on these two days were compatible and the same value for η_0 has been used on both days. We therefore combine the two data sets to increase the overall number of data points as well as to improve the sampling of the scanned parameter t_{evo}. Table 4.1 summarizes all important parameter of the three mentioned time evolution data sets. Further details on the experimental procedure, data generation and post processing are found in section 3.6.3. Further statistics information on all experimental data sets presented in this section are found in Appendix A.1. The observable $N_{L,0}/N_L$ that corresponds to N_{p}/N as introduced in the previous section is plotted as a function of evolution time t_{evo} for the datasets in Fig. 4.7. Similar to the numerical data in Fig. 4.3 the experimental data shows non harmonic oscillatory behaviour on the order of tens of milliseconds. However, the experimental oscillations are damped at later times. Various effects and mechanisms come to mind that can cause such form of reduced visibility:

- fluctuations in experimental parameters from shot to shot leading to fluctuations in the building block parameters.

	data set 18.04.2019 and 23.04.2019	data set 24.04.2019
total shot number	541	211
magnetic field B [G]	2.118 ± 0.002	2.118 ± 0.002
η_0	0.407 ± 0.002	0.292 ± 0.002

Table 4.1.: **Characteristic properties of the time evolution data sets.** Errors represent the standard error of respective parameter.

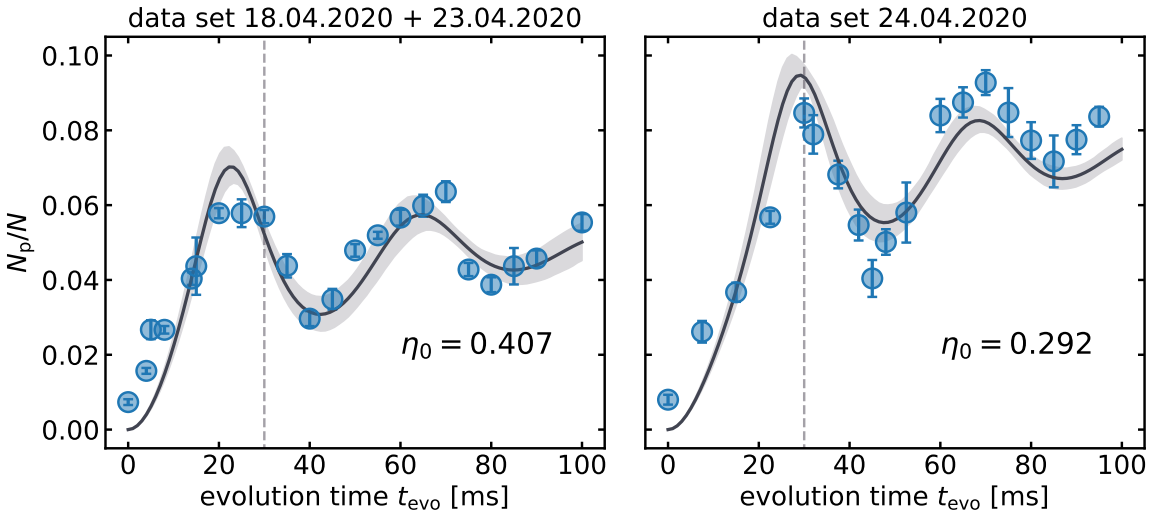

Figure 4.7.: **Experimental time evolution measurements for two different values of η_0 (left and right) and the respective building block dynamics with best fitting parameters.** The observable N_p/N is plotted as a function of the evolution time t_{evo}. The experimental data (blue circles) displays an initial onset of N_p/N followed by damped oscillations at later times. The black curve is the result of numerically solving the set of equations of motion 4.9 with parameters λ^{exp}, χ^{exp} and Δ^{exp} that best fit the experimental data. The shaded area represents the 68% confidence interval from bootstrap resampling of the fitted parameters. The grey dashed line marks the value at $t_{evo} = 30$ ms as used for generating the resonance data presented in section 4.2.2. Errorbars on the experimental data points indicate the standard error on the mean.

- atom loss from the trap during the evolution time, especially in the $|1, 0\rangle$ state of sodium, see section 3.6.3.
- quantum fluctuations of the initial state.

- spatial dynamics of both atomic clouds within the trap that are not fully frozen out.
- finite temperature effects since the clouds are only partially condensed.

A more detailed discussion about each of these points is provided in section 4.2.4, where we elaborate on the impact that each effect has on the resulting dynamics and how it can potentially be overcome. For now we disregard the exact origin of the damping and treat it from a phenomenological point of view, generalizing all possible influences simply as a decoherence effect. To this end we use the Lindbladian formalism which generally allows for the description of non-unitary evolution of quantum systems [114, 115]. Formally, we introduce a decoherence term into the equations of motion 4.3 that accounts for the damping mentioned above, resulting in the modified equations of motion

$$\partial_t L_{x,N} = -2\chi L_{z,N} L_{y,N} + 2\lambda L_{z,N} L_{y,L} - \frac{\gamma}{2} L_{x,N} \ , \tag{4.9a}$$

$$\partial_t L_{y,N} = 2\chi L_{z,N} L_{x,N} - 2\lambda L_{z,N} L_{x,L} - \frac{\gamma}{2} L_{y,N} \ , \tag{4.9b}$$

$$\partial_t L_{z,N} = 2\lambda (L_{y,N} L_{x,L} - L_{x,N} L_{y,L}) \ , \tag{4.9c}$$

$$\partial_t L_{x,L} = -\Delta L_{y,L} + 2\lambda L_{z,L} L_{y,N} - \frac{\gamma}{2} L_{x,L} \ , \tag{4.9d}$$

$$\partial_t L_{y,L} = \Delta L_{x,L} - 2\lambda L_{z,L} L_{x,N} - \frac{\gamma}{2} L_{y,L} \ , \tag{4.9e}$$

$$\partial_t L_{z,L} = 2\lambda (L_{y,L} L_{x,N} - L_{x,L} L_{y,N}) \ , \tag{4.9f}$$

with the introduced decoherence timescale $1/\gamma$, which is estimated by fitting an exponential decay to the envelope of the data shown in Fig. 4.7, yielding $1/\gamma = 41 \pm 13$ ms, i.e. $\gamma/2\pi = 3.9 \pm 1.2$ Hz. A more rigorous derivation of equations 4.9 is found in [43].

We use this modified set of equations to numerically determine best fitting building block parameters λ^{exp}, χ^{exp} and Δ^{exp} that best describe the experimental time evolution data shown in Fig. 4.7. The respective fitting results are summarized in table 4.2. The curves corresponding to the fitted parameters are plotted in Fig.4.7, clearly illustrating that the experimental data is well described by the model given by the equations 4.9. An important point to mention is that fitting the experimental data did not converge then using simple damped trigonometrical functions, stressing that the physics involved in our experiment cannot be described by a Rabi-type coupled two level system [85].

In terms of the fitted parameters as presented in table 4.2 the results are consistent between the two data sets, i.e. the parameters χ^{exp} and λ^{exp} are compatible within errorbars and only Δ^{exp} varies between the two data sets as expected for a change of η_0 according to relation 4.7. Using this relation and extrapolating between the two measured values of Δ^{exp}, in addition we determine the parameters Δ_0^{exp} and Δ_L^{exp}.

	data set 18.04.2019 and 23.04.2019	data set 24.04.2019
$\chi^{\mathrm{exp}}/2\pi$ [mHz]	9.52 ± 0.09	9.52541 ± 0.00023
$\lambda^{\mathrm{exp}}/2\pi$ [µHz]	17.6 ± 1.0	18.7 ± 0.8
$\Delta^{\mathrm{exp}}/2\pi$ [Hz]	-546 ± 4	-1218
$\Delta_0^{\mathrm{exp}}/2\pi$[Hz]	2 ± 7	
$\Delta_L^{\mathrm{exp}}/2\pi$[kHz]	2.919 ± 0.017	

Table 4.2.: **Overview of the building block parameters determined by the fitting routine based on the equations in 4.9 and the time evolution data presented in Fig. 4.7.** The values for λ^{exp} and χ^{exp} are (as predicted by the building block model) fully compatible within errorbars. As the two time evolution measurements were recorded at two different values of η_0, the fitted values for Δ^{exp} differ accordingly. By using these two values for η_0 and Δ^{exp} we determine the parameters Δ_0^{exp} and Δ_L^{exp} using relation 4.7. Errors represent the standard error of respective parameter as provided by the covariance matrix of the least squares fitting routine. No error is indicated for Δ^{exp} from 24.04.2019 as it is negligibly small.

4.2.2. Experimental resonance measurements

Complementary to the time evolution data presented in the previous section we have recorded an η_0 scan at the same magnetic field of $B = B_0$ (recorded on 25.04.2019). Further details on the experimental procedure of generating this type of data set is found in section 3.6.4. Additional statistics information on the experimental data sets are found in Appendix A.1.

Fig. 4.8 displays the data of this particular scan by plotting N_{p}/N as a function of η_0. The experimental resonance scan shows all features of the building block resonance behaviour as previously found with ab initio parameters, (see Fig. 4.4), i.e. the functional shape with a steep edge at lower values of η_0 and the long tail towards higher values of η_0.

This scan allows for very useful crosschecking of our experimental measurements. The time evolution data shown in Fig. 4.7 is partially incorporated in the data shown in Fig. 4.8 and vice versa. In particular the values for $\eta_0 \approx 0.4$ and $\eta_0 \approx 0.29$ in Fig.4.8 correspond to respective time evolution data at $t_{\mathrm{evo}} = 30\,\mathrm{ms}$. This correspondence is indicated in all three plots by dashed lines. In terms of this relation the experimental data of time evolution and resonance scans are fully compatible. This finding further confirms that the experimental η_0 scans are a valid measurement to determine the discontinuity feature that has been proven to be a characteristic feature arising from building block dynamics.

Analogously to the fitting procedure described in the previous section we numerically fit the resonance data with the model described by the set of equations 4.9 for varying values of η_0 and sampling the emerging dynamics at $t_{\mathrm{evo}} = 30\,\mathrm{ms}$ according to the experimental

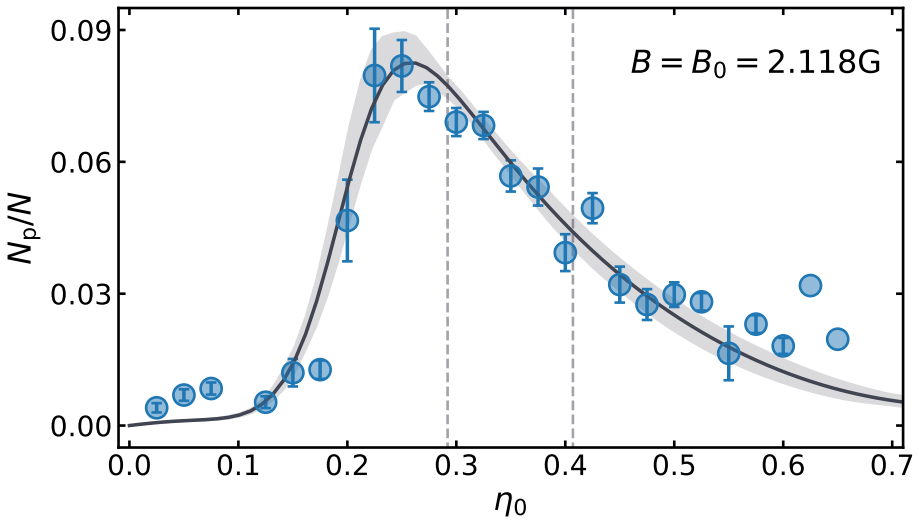

Figure 4.8.: **Experimental resonance measurement and the respective building block resonance curve based on best fitting parameters.** The observable N_p/N plotted as a function of η_0. The experimental data (blue circles) display a clear resonance feature characterized by a steep edge around $\eta_0 \approx 0.2$ and a long tail towards higher values of η_0. The black curve is the result of numerically solving the set of equations of motion 4.9 and sampling the resulting curves at $30\,\mathrm{ms}$. The parameters λ^exp, χ^exp, Δ_0^exp and Δ_L^exp were chosen to best fit the experimental data. The shaded area represents the 68% confidence interval from bootstrap resampling of the fitted parameters. The grey dashed lines mark the values of η_0 at which the time evolution data shown in Fig. 4.7 were recorded. Errorbars on the experimental data points indicate the standard error on the mean. Datapoints without errorbars represent experimental realizations of a single value and not a mean, see Appendix A.1.

protocol. The so determined best fitting building block parameters are summarized in table 4.3 and the corresponding curve is shown in Fig. 4.8 once again confirming the validity of the used model to describe the experimental data. The best fitting parameters from the time evolution measurements (table 4.2) and the resonance measurements (table 4.3) are fully compatible within errorbars (with exception of λ^exp at $\eta_0 = 0.292$).

The data presented so far has been recorded at a fixed magnetic offset field of $B = 2118$ G. To make full use of the tunability of the building block, we performed resonance measurements analogously to the data shown in Fig. 4.8 at various values of B. This data is shown in Fig. 4.9. Once again one identifies every qualitative feature of this kind of B field scan as previously found in Fig. 4.6. With varying value of B the position of the steep edge moves in terms of η_0 to smaller values for decreasing B and to higher values of η_0 for increasing B. Furthermore, the peak value of N_p/N reduces with reduced B until almost no distinct peak structure is seen at $B = 1.968$ G.

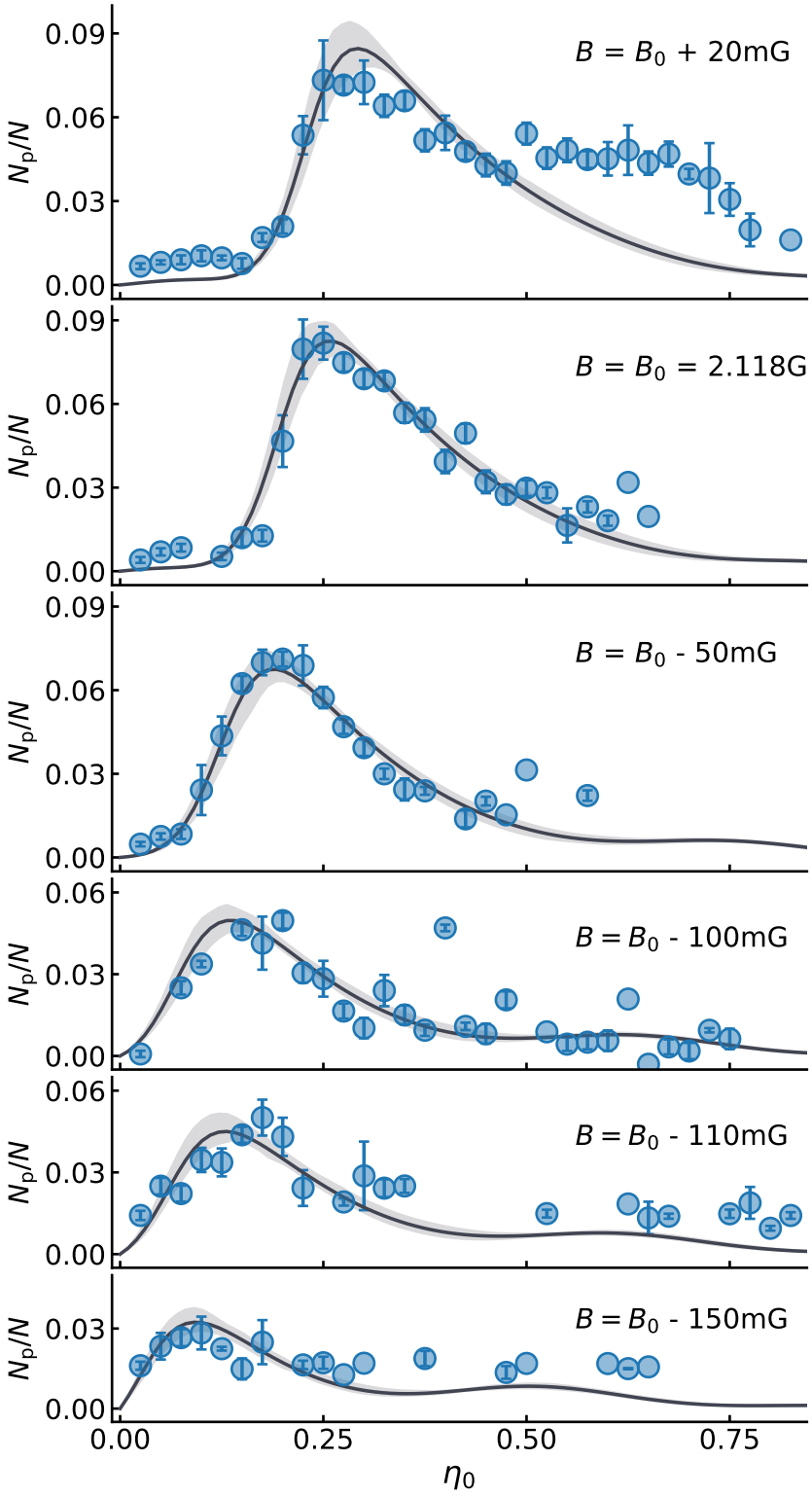

Figure 4.9.: **Experimental resonance measurements recorded at different magnetic offset fields B.** Resonance scans analogous to Fig. 4.8 for different values of B. For reducing values of B the experimental data (blue circles) show a shift of the steep edge of the resonance to smaller values of η_0. Furthermore, a reduction of B is associated with a reduction of the peak value of N_p/N. The black curves are the results of our building block model in analogy to the curve shown in Fig. 4.8. Note that for all curves we used the building block parameter λ^exp, χ^exp, Δ_0^exp and Δ_L^exp as determined from the fit to the data at $B = B_0$. For the data at $B \neq B_0$ we used the magnetic field dependence term $\Delta_B(B - B_0)/B_0$ from equation 4.7, with Δ_B chosen to best fit all data sets.

	data set 25.04.2019
$\chi^{\mathrm{exp}}/2\pi$ [mHz]	9.559 ± 0.010
$\lambda^{\mathrm{exp}}/2\pi$ [μHz]	16.7 ± 0.5
$\Delta_0^{\mathrm{exp}}/2\pi$[Hz]	3.9 ± 2.1
$\Delta_L^{\mathrm{exp}}/2\pi$[kHz]	2.9168 ± 0.0015

Table 4.3.: **Overview of the building block parameters determined by the fitting routine based on the equations in 4.9 and the resonance data presented in Fig. 4.8.** Errors represent the standard error of respective parameter as provided by the covariance matrix of the least squares fitting routine. With only one exception (λ^{exp} at $\eta_0 = 0.292$), these values are fully compatible with the fitted values from the time evolution data, see table 4.2.

According to the building block model, all changes seen in the resonance plots at different values of B are governed by the single parameter Δ_B, see equation 4.7. To emphasize that all resonance measurements are consistent with this model, we use the values for the building block parameters χ^{exp}, λ^{exp}, Δ_0^{exp}, and Δ_L^{exp} as determined by the fit at $B = 2118$ G, see table 4.3, to describe all resonance data shown in Fig. 4.9, only using the term $\Delta_B(B - B_0)/B_0$ to account for changes in Δ due to the magnetic offset field B, with Δ_B determined to best match all resonance data at the same time. The best fitting value for Δ_B is found to be $\Delta_B/2\pi = (-517.10 \pm 0.28)$ Hz. The so determined curves are plotted together with experimental data in Fig. 4.9, showing an agreement that is remarkable, considering the complexity of the underlying model based on the building block equations of motion 4.9 and the fact that only the fitted parameter Δ_B was used to describe the additional five resonance scans taken at different B.

With respect to the measurements at different magnetic offset fields B, the parameter Δ_0^{exp} has an intuitive interpretation. It is a constant value for the building block in the sense that it is not changed by the parameters η_0 or B. The physical origin of this constant Parameter are contributions of various mean field shifts, see equation 4.6. For the fitting routine we have chosen the zero point of the magnetic field dependence to be $B_0 = 2.118$ G, which is 165 mG higher than the zero magnetic field determined from the single particle evaluation by the Breit-Rabi formula, see Fig. 3.12. By choosing B_0 we therefore implicitly absorbed the effect of the mean field shifts. The fitted value of Δ_0^{exp} being close to zero is confirmation that with our choice of B_0 we have anticipated the correct value for the mean field shift in this model which amounts to a value of approximately $h \cdot 107$ Hz.

4.2.3. Comparison of ab initio and best fitting parameter

When comparing our ab initio estimates for the building block parameters 4.8 with the experimentally determined ones from table 4.3 one gets

$$\chi^{\text{th}}/\chi^{\text{exp}} \approx 2.2 \,, \tag{4.10a}$$
$$\lambda^{\text{th}}/\lambda^{\text{exp}} \approx 3.5 \,, \tag{4.10b}$$
$$\Delta_0^{\text{th}}/\Delta_0^{\text{exp}} \approx 19 \,, \tag{4.10c}$$
$$\Delta_L^{\text{th}}/\Delta_L^{\text{exp}} \approx 2.2 \,, \tag{4.10d}$$
$$\Delta_B^{\text{th}}/\Delta_B^{\text{exp}} \approx 3.2 \,. \tag{4.10e}$$

The values of the ab initio estimates are with exception of Δ_0 in the same order of magnitude. Furthermore all ab initio estimates are larger than the experimentally determined ones. Most important, the signs of the values agree, leading to a correct prediction of the resonance shift as a function of B and η_0 with regard to the experimental data. Comparing the time evolution measurements with the dynamics emerging from the ab initio parameters in Fig. 4.1.4 one can see that the experimental data have about a factor of two slower oscillation frequency and about a factor two smaller amplitude. However, one can clearly see qualitative similarities, for instance the non harmonic behaviour of the oscillations that reflects in the strongly curved and "pointy" looking maxima for $\eta_0 \approx 0.29$.

There are multiple reasons for the discrepancy of ab initio estimates and experimentally determined values. First, the ab initio estimates were derived by assuming zero temperature (Gross-Pitaevskii equation) and only a single spatial mode (see overlap integrals 2.52). Assumptions which are only partly fulfilled in the experiment. Second, the experimental input parameter for deriving the density distributions by means of imaginary time propagation have uncertainties which were not taken into account. Third, all effects that are incorporated into our building block model via the decoherence term are not included in the ab initio estimation of the building block parameters.

4.2.4. Decoherence effects present in the experimental building block

A described in section 4.2.1 we incorporated a phenomenological decoherence term into the mean field building block equations of motion 4.9 to account for the damping of oscillations that we observe in the time evolution data. This modification allowed for finding building block parameters that excellently describe all experimental findings.

In the following we will show that the inclusion of such a decoherence term is not only justified but strictly necessary to describe our system even in the absence of any experimental imperfection, since undamped time evolutions are only expected to occur in the mean field limit.

Spatial dynamics of sodium

All experimental measuements are initialized by quenching sodium into a superposition of the two magnetic substates $|1,1\rangle$ and $|1,0\rangle$, which corresponds to preparing a certain value of η_0. In addition to the state population the quench also initializes spatial dynamics in the sodium cloud. In Fig. 4.10 we display the time of flight density distribution of sodium after a quench initialization to a value of $\eta_0 \approx 0.5$ as a function of evolution time and for two different total sodium atom numbers. The data is recorded after a Stern Gerlach separation and in the absence of lithium in the trap. In the upper panel of Fig. 4.10 one can see a clear signature of the spatial dynamics. The $|1,1\rangle$ component develops a ring shaped structure while the $|1,0\rangle$ component is compressed stronger and increases in density for the first few milliseconds of the time evolution. For later interaction times the sodium components continue to perform a breathing-type motion, where they oscillate between various shapes on a timescale of the trapping frequencies. For the effects of the spatial dynamics at later evolution times, see Fig. 3.22.

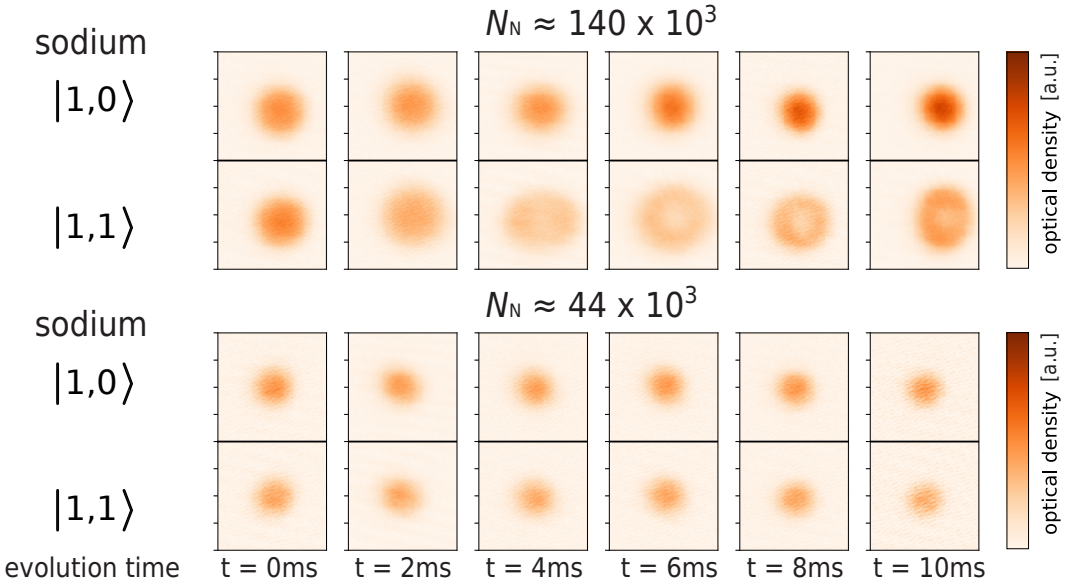

Figure 4.10.: **Averaged absorption images of sodium revealing signatures of the spatial dynamics.** An about equal superposition of sodium in the $|1,1\rangle$ and $|1,0\rangle$ is created and held in the trap for various evolution times t_{evo}. Afterwards, we apply our usual state sensitive readout, see Fig. 3.15. In this measurement lithium is absent from the trap. In the case of higher total atom number (top row) the $|1,1\rangle$ component develops a ring shape structure as a function of time while the $|1,0\rangle$ component is visibly compressed, an observation which we attribute to the spatial dynamics that occur after the superposition quench. In the case of reduced atom number (bottom row) those kind of signature effects cannot be detected visually. Note that the spin changing measurements that we presented in this chapter were performed with a total sodium atom number of $N_N \approx 300 \times 10^3$.

Those dynamics emerge from two different physical effects, which are known as “poten-

tial separation" [116, 117] and "sphase separation" or "immescibility" [53, 116, 117]. Both effects arise from the fact that the ground state density distribution of an interacting BEC is generally governed by the external trapping potential and the intra-species interaction energy $g_j|\Phi_j(\mathbf{x})|^2$, with $j \in \{0, 1\}$, see equation 2.43. In the case of a two-component bose gas this can lead to situations where it is energetically favourable for the system that the two components increase their spatial overlap (miscibility), or reduce their spatial overlap (immiscibility). A criterion for miscibility is given by relation [53]

$$\sqrt{g_{11}g_{00}} < g_{10}^2 \,, \tag{4.11}$$

where we have used the index notation from section 2.4. If inequality 4.11 is fulfilled, the system is miscible and if it is not fulfilled it is immiscible. In our case, the two components $|1, 1\rangle$ and $|1, 0\rangle$ of sodium are immiscible, see table 2.1. The miscibility criterion holds even in the absence of an external trapping potential, i.e. for a homogeneous system of two immiscible components the ground state is comprised by two separated phases.

However, even for miscible components a redistribution of density of two components can occur, when considering an external potential. Before the superposition quench all atoms occupy the $|1, 1\rangle$ state in our experiment and the density distribution is governed by the respective ground state of the system. By performing the sudden quench, the states $|1, 1\rangle$ and $|1, 0\rangle$ are populated, both having the spatial profile as the initial state before the quench. As this spatial profile is not the ground state of the new two-component configuration, the system initializes a redistribution of the components density, where due to the asymmetry $g_{11} > g_{00}$ the $|1, 1\rangle$ component favours the edges of the trapping potential as the density in that region is lower.

In general both mentioned effects contribute to the spatial dynamics that we observe in the sodium components. As we are recording time of flight measurements of the clouds we are only indirectly inferring the in situ spatial dynamics of the components and do not describe the process in a more quantitative way.

The spatial dynamics are not incorporated in the building block model, since in the single mode approximation we have dropped the kinetic term of the Hamiltonian. The introduction of a decoherence term in the equations in 4.9 is reasonable in order to account for the spatial dynamics.

Firstly, this approach led to the determination of the fitting parameters χ^{exp}, λ^{exp}, Δ_0^{exp} and Δ_L^{exp}, which on the one hand entail all characteristic features of the mean field building block dynamics as presented in section 4.1.4 and on the other hand describe the experimental data very well in both the time evolution and resoncance data. It is important to note here that the time evolution scans are effected stronger by the damping as the resonance scans, since latter samples the oscillation at $30\,\mathrm{ms}$, a time when the data is more robust towards the decoherence effects (as compared for instance to later times in the time evolution). Nonetheless, the same fitting parameter are capable to describe both type of scans, a consistency that further advocates our chosen approach.

Secondly, the method we chose can be understood from the following descriptive interpretation. During the spatial dynamics of the sodium clouds in the trap, lithium and sodium still have spatial overlap (although time vaying), i.e. the spin changing collision process is

still possible. Due to the time dependent overlaps, however, we cannot allocate a single set of parameters χ, λ, and Δ. We rather have to consider different sets of parameters at different times. The resulting dynamics from the building block equations of motion averaged over multiple parameter sets then indeed result in oscillations that would still have characteristic features of the single mode mean field building block dynamics, however, would decohere for later times. An observation that is compatible with our experimental findings.

Finally, we want to address possible methods to reduce the spatial dynamics. Since for now we do not have access to the time and space resolved density distributions of the individual components, we cannot quantitatively study how changing experimental parameters exactly influences the spatial dynamics. One can, however, make an energy argument. Since the spatial dynamics physically emerge form the interplay between potential energy and interaction energy of the atoms, increasing the potential energy to the point where the interaction energy becomes negligible would lead to a far less dominant effect of the spatial dynamics. Whether such a regime can be reached by tuning trapping potential and atom numbers in our experiment has yet to be explored.

An interesting observation related to the spatial dynamics is presented in the lower panel of Fig. 4.10. By reducing the total atom number of sodium, the typical signature of spatial dynamics that we use to observe in time of flight does not appear. To quantify the effect of the spatial dynamics, we compute the normalized spatial overlap between the $|1,1\rangle$ and $|1,0\rangle$ components as seen in Fig. 4.10 as a function of evolution time and for various total atom numbers of sodium, see Fig. 4.11. It shows that the general signature of spatial dynamics that we observe, i.e. different deformation of the two clouds in time of flight and after a few milliseconds of evolution time is less pronounced at smaller atom numbers. Note that this observation is just an implication on how the spatial dynamics can be influenced, since inferring the exact spatial dynamics in the trap from time of flight images is rather involved.

Atom loss

As mentioned in section 3.6.3 we observe state dependent atom loss of sodium during the time evolution measurements. In ultracold atom experiments there are generally various loss mechanisms of atoms from the trap. However, in the context of the spin changing collisions experiments that we perform, we are interested in loss mechanisms that lead to trap lifetimes on the order of hundrets of milliseconds. Therefore in this discussion we disregard the losses due to collisions with background atoms due to finite vacuum or the loss due to photon scattering from the dipole trap as those happen on timescales of multiple tens of seconds. We observe the atom loss solely in the $|1,0\rangle$ component of sodium. In Fig. 4.12 we estimate the $1/e$-lifetime τ of sodium atoms in the $|1,0\rangle$ state by fitting an exponential decay to the sodium atom number data corresponding to the data sets thar are presented in Fig. 4.7. The fits yield a lifetime of $\tau = (508 \pm 22)\mathrm{ms}$ for the combined data set of 18.04.2020 and 23.04.2020 ($\eta_0 = 0.407$) and a lifetime of $\tau = (240 \pm 6)\mathrm{ms}$ for the data set of 24.04.2020 ($\eta_0 = 0.407$). In terms of the spin exchange dynamics that we observe in lithium, a decay of the $|1,0\rangle$ component leads to time varying system parameters and similar to the case of the spatial dynamics can damp the overall oscillations. More important is that the atom loss breaks our assumption of the magnetization M to be a conserved quantity. In the end this process

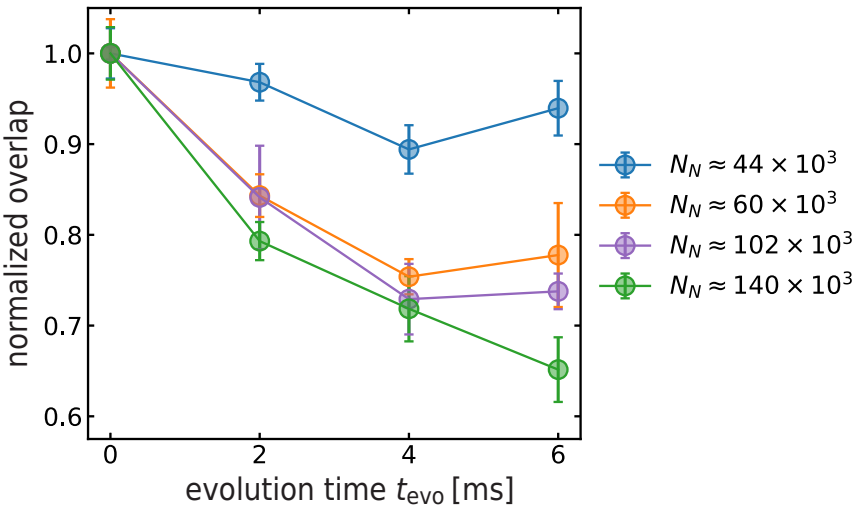

Figure 4.11.: **Quantitative evaluation of the spatial dynamics signature for various total atom numbers N_N as seen in Fig. 4.10**. The spatial overlap of the $|1,1\rangle$ and $|1,0\rangle$ column densities is evaluated and plotted as a function of the evolution time t_{evo} in the trap. The spatial overlap is normalized to the value at $t_{\mathrm{evo}} = 0\,\mathrm{ms}$. Generally, a reduction in total atom number leads to more overlap as a function of t_{evo}. Note that since the absorption images are recorded after time of flight, this findings are only indications for the exact spatial dynamics in the trap. Circles are experimental mean values with errorbars indicating the standard error on the mean, solid lines are guides to the eye.

compromises the gauge invariance in the lattice gauge theory model, since the necessary constraint between gauge field and matter field (which in the cold atoms system is given by the constraint that sodium population changes only when lithium population changes, and vice versa) is not fulfilled anymore.

In view of the detrimental effect of atom loss on gauge invariance it is of great importance to determine the underlying loss mechanism. A systematic study hereof has yet to be performed in our experiment. In particular the influence of the spatial dynamics on two-body loss [73, 118–120] and three-body loss [118, 121–123] processes has to be evaluated. Furthermore the loss process in sodium has to be studied with regard to the presence and absence of lithium in the trap.

Experimental fluctuations in initial parameters

Our experimental data relies on the averaging of many experimental realizations. Accordingly shot to shot fluctuations in the experiment give rise to uncertainties on the measured (mean) values. In particular fluctuations of important parameters (e.g. total atom number or η_0) lead to dynamics of spin changing collisions that average over various initial conditions. As mentioned before, an averaging over many oscillations will eventually lead to a damped oscillation as we observe in the experimental time evolution data.

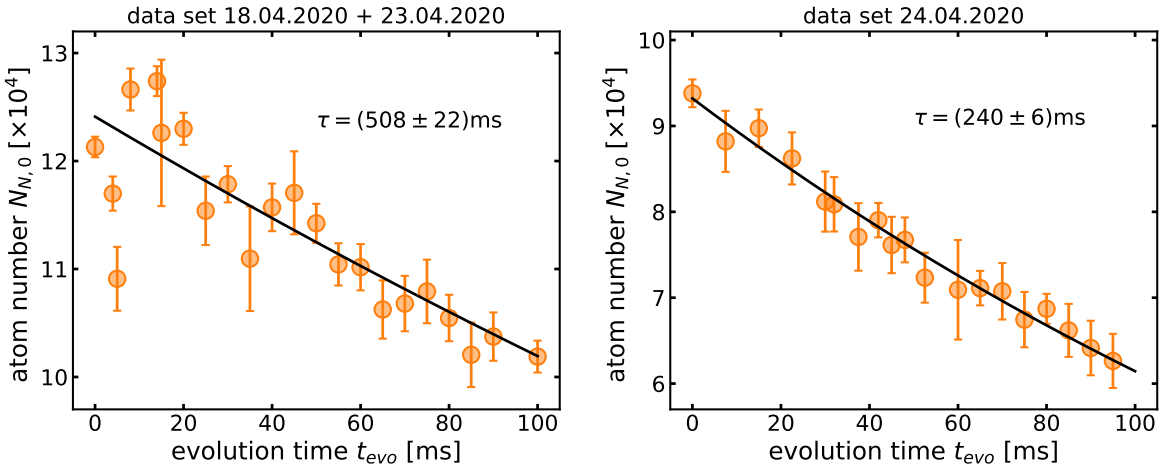

Figure 4.12.: **Lifetime estimation of the $|1,0\rangle$ component of sodium.** Experimental measurements (orange circles) of the sodium atom number in the $|1,0\rangle$ state as a function of evolution time t_{evo} for the data sets that are presented in Fig. 4.7. The data is fitted with an exponential decay (black line) to determine the $1/e$ lifetime τ. Errorbars indicate the standard error on the mean.

Since we rely on averaging many experimental realizations, while a single realization takes about one minute of time, makes data acquisition over a long period of time necessary. This makes the data susceptive to drifts of certain parameters on the time scale of hours or days. The effect of these drifts is not directly apparent from shot to shot, however, can influence the data significantly on a longer timescale. Parameters that tend to drift over time in our experiment are the ambient temperature of the room, magnetic offset fields and overall laser powers. We employed active stabilization schemes based on negative feedback control to stabilize the magnetic offset field [42, 124], the room temperature [73] and laser powers [90] that are known to be critical in the experiment (e.g. laser power of the dipole laser beams creating the optical trapping potential). Although these schemes greatly improved the performance stability of the experiment, a certain amount of experimental fluctuations will remain.

Quantum fluctuations

Even in the absence of any experimental fluctuations, our system will still exhibit quantum uncertainty. For our mean field building block equations of motion 4.3 we neglected quantum effects by replacing the quantum mechanical spin operators by their respective expectation values. Although the mean field approximation was reasonable considering the applicability of the model to our experimental data, the fact that the resulting dynamics exhibit full fringe contrast, is a signature of the mean field limit. Preliminary classical statistical simulations of the dynamics imply that taking into account quantum effects lead to a damping of the resulting dynamics. From this point of view our modification of the equations of motion by inclusion of a decoherence term (see equation 4.9) is in principle not only a method to

phenomenologically describe the experimental data, but also the right modification to our theoretical description to capture the physics of our system.

Note that although we expect quantum effects to contribute to decoherence in our system, it is not the dominating source. For instance, the quantum projection noise [92, 125] on the determination of the sodium superposition ratio η_0 is at least one order of magnitude smaller than the experimentally measured fluctuations, indicating that in this regard our experiment operates in a regime where experimental fluctuations dominate the noise source.

Non zero temperature effects

The building block Hamiltonian 2.76 has been derived assuming that all atoms of one species occupy a single mode, see equation 2.49. This assumption is only valid in the case of a pure BEC with none to very small thermal fraction and otherwise all atoms in the condensed ground state. As shown in Fig. 3.9 our system has a non negligible amount of atoms in the thermal part.

Although thermal atoms can undergo spin changing collisions as well, the underlying process is quantitatively different from the one in the condensed phase. Generally, the thermal atoms have lower density than the condensed atoms. Furthermore, one has to take into account that thermal atoms are populated over multiple momentum modes.

These considerations imply that the thermal part of the atoms does not coherently contribute to the spin dynamics as exerted by the condensed part and therefore a damping of the overall spin dynamics can occurs. In [37] coherent heteronuclear spin dynamics are reported between an almost pure BEC of sodium and a thermal cloud of rubidium. In our case, where both species are partly condensed, the quantitative influence of the thermal part is not fully described yet.

4.2.5. Summary

In this section we have presented experimental spin changing collisions data and compared it qualitatively and quantitatively to the building block dynamics in the mean field limit as derived in the previous section. Compared to the mean field dynamics the experimental time evolution data exhibit damped oscillations at longer times. We introduced a physically motivated decoherence term into the mean field equations of motion, such that the model shows excellent agreement for the experimental data with numerically determined best fitting building block parameters. This agreement is consistent across all systematically performed parameter scans, including measurements (time evolution) that are prone to the decoherence effects and measurements (resonance by scanning η_0) that are more robust to them. These findings stress the validity of our approach and identify our experimental system as a faithful representation of the building block.

The effects that contribute to the decoherence have different physical orgins and have been discussed in detail. In the cases where the reduction of decoherence is not fundamentally limited but due to experimental imperfections we lay out possible future efforts for reducing the decoherence.

5. Summary and outlook

In this work we have presented the experimental realization of a building block for a U(1) lattice gauge theory [36]. We have pointed out the theoretical framework for our proposed system in the quantum link formalism, analogous to the Schwinger model with Wilson Fermions [17]. Our proposal is based on repetitions of individual building blocks that are arranged on the sites of an optical lattice and linked via Raman-assisted tunneling. The individual building block is conceptionally the most crucial part of the proposal, as it contains the gauge invariant interactions between matter fields and gauge fields, a constraint that is by far the most difficult one to implement in quantum simulators. Regarding that, our building block offers the advantage that gauge invariance is systematically protected by inherent symmetries of the experimental system.

We have realized the building block in our ultracold mixture experiment of optically trapped bosonic sodium and lithium. In our system the gauge field is simulated by the sodium atoms and the matter field by lithium atoms. The gauge invariant interaction is realized by heteronuclear spin changing collisions between the two species. This process is constrained by angular momentum and energy conservation in our sytem, making it highly suitable for the experimental implementation of U(1) gauge invariance.

We have experimentally demonstrated heteronuclear spin changing collisions between bosonic sodium and bosonic lithium. We have identified the parameter regime in which this process occurs in our system, e.g. the value of the magnetic offset field where the spin changing collision process exhibits a large amplitude turns out to be hundrets of milligauss shifted compared to the single particle prediction based on the Breit-Rabi formula due to a mean field shift. The spin changing collisions dynamics have been systematically studied and characteristic features have been identified. One of these features is a typical asymmetric resonance of lithium spin transfer as a function of the initial sodium state population. We have identified our experimental system as a faithful representation of the building block as needed for the quantum simulation of our proposed U(1) lattice gauge theory.

The next steps towards the experimental realization of an extended lattice gauge theory include the arrangement of building blocks on sites of an optical lattice. The necessary technical setup for generating lattice trapping potentials has already been established in our experiment. In the course of this transition towards the lattice configuration, important questions to address are how the spatial dynamics and atom loss from the trap will behave in a lattice confinement compared to the confinement in the crossed dipole trap. Generally one could expect a reduction of spatial dynamics as those are effectively frozen out in lattice confinements with typical trap frequencies on the order of kilohertz. Furthermore, faster spin changing collision dynamics can be expected as the tighter confinement of the lattice wells will lead to a larger spatial overlap of the species. However, a tighter confinement could lead to higher three-body losses due to the increased density of the species.

Another important step towards the extended lattice gauge theory is the coupling of individual building blocks via Raman-assisted tunneling [74–76]. A highly tunable laser source that is capable of generating the necessary Raman laser beams has been established in our group. An estimation based on realistic experimental parameters [36, 43] has shown that our setup is capable of achieving Raman-assisted coupling strength on the order of kilohertz, which is orders of magnitude higher than undesired direct tunneling strength. Together with spin changing collision dynamics on the order of tens of milliseconds, our estimations for the overall dynamics of our proposed extended lattice gauge theory are significantly faster than in previous proposals with comparable parameters [15, 17]

The building block presented here and the corresponding extended lattice gauge theory are based on bosonic matter [36]. In order to realize a relativistic gauge theory as existing in nature one will have to replace bosonic lithium with fermionic lithium, which will recover Lorentz-invariance in the continuum limit. From a technical point of view the replacement of bosonic lithium with fermionic lithium in our experiment is straightforward and does require minimal effort [40, 41, 126, 127]. Towards the realization of heteronuclear spin changing collisions between sodium and fermionic lithium one has to identify the necessary experimental parameter regime. The findings about the heteronuclear spin changing collisions presented here are of great value for that.

The findings presented in this thesis open the door for quantum simulation of gauge theories in ultracold atoms experiments with the possibility to address physical questions that are out of reach for classical computational techniques [11–17]

A. Appendix

A.1. Statistics of individual data sets

The data points that are presented in section 4.2 represent the mean value of a set of raw data points and the errorbar is indicating the standard error on the mean. Due to the randomized fashion in which we recorded the data sets not every mean value is sampled with the same amount of raw data points. Especially in the case of the resonance measurements, where η_0 is estimated by measuring the corresponding sodium population and subsequent binning, (see section 3.6.4), this leads in some cases to data with far less samples at higher values of η_0 than at lower values.

In order to visualize the origin of the errorbars in the data presented in 4.2, here, we display the corresponding raw data of the scans. In Fig. A.1 we display the raw data that corresponds to the time evolution measurements shown in Fig. 4.7.

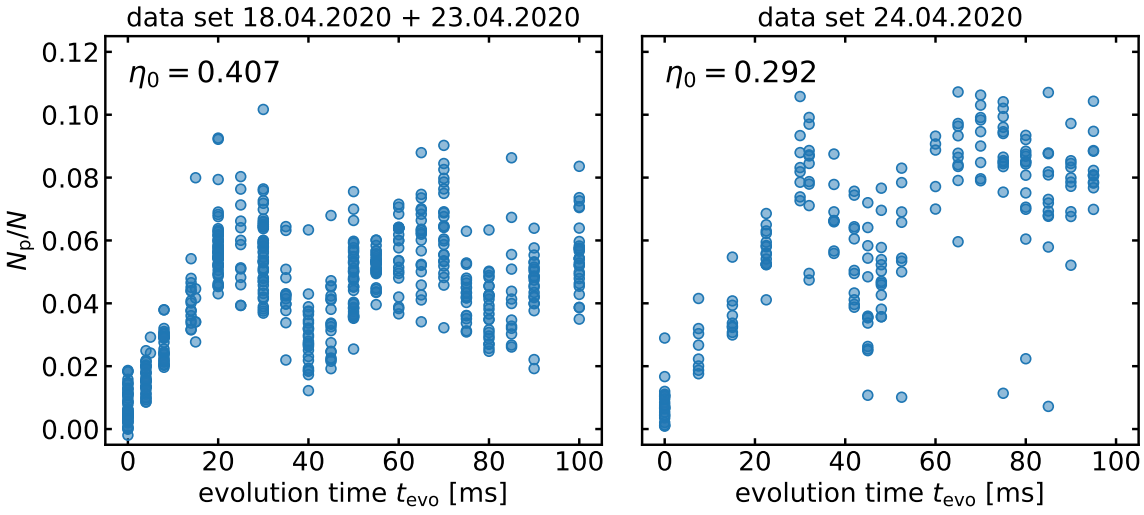

Figure A.1.: **Raw time evolution measurements corresponding to the data shown in Fig. 4.7.** Data points correspond to the value retrieved from a single experimental cycle. Due to way the data has been acquired, for instance by randomizing the parameter scan or due to the fact that two data sets have been combined, the parameters on the x-axis have not been sampled by equally many samples.

In Fig. A.2 we display the raw data that corresponds to the resonance measurements shown in Fig. 4.9.

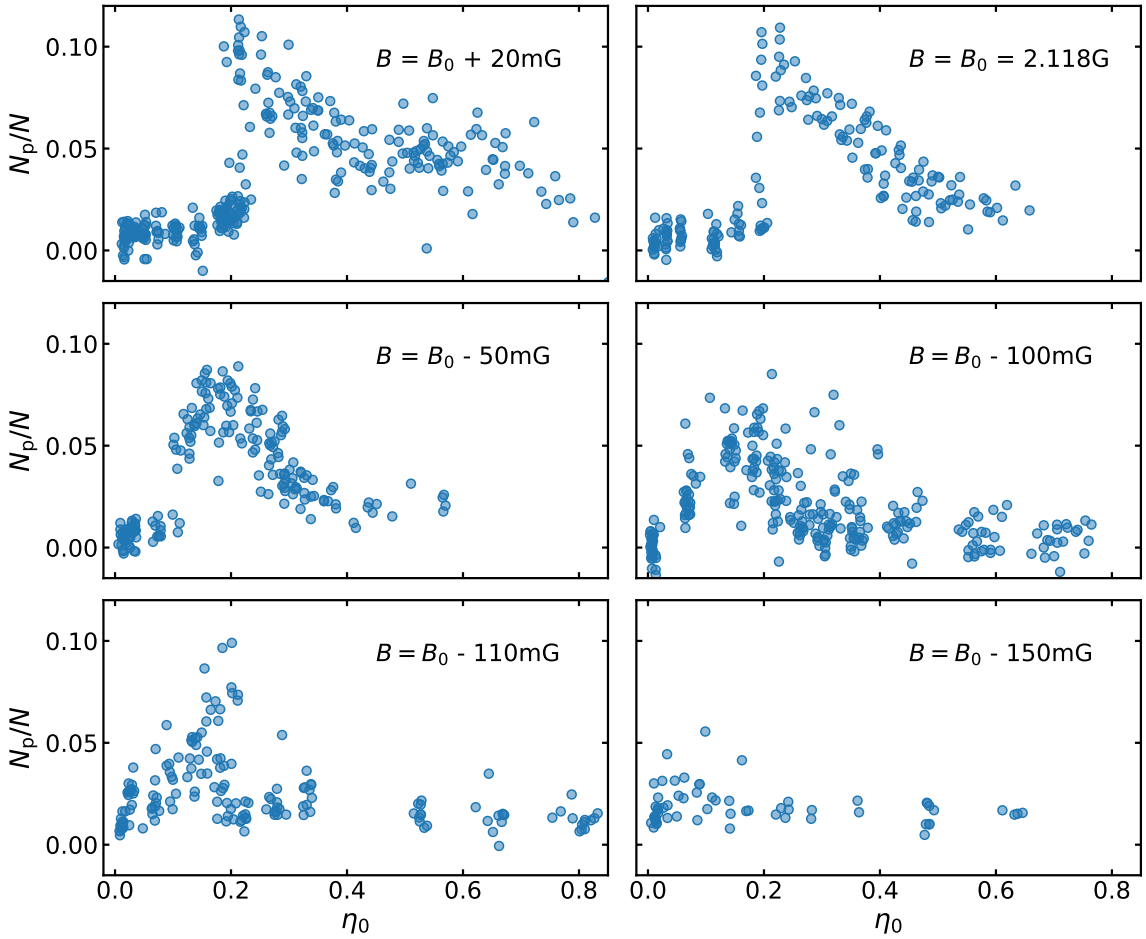

Figure A.2.: **Raw resonance measurements corresponding to the data shown in Fig. 4.9.** Data points correspond to the value retrieved from a single experimental cycle. The binning method for η_0 as described in 3.6.4 leads to the fact that larger values for η_0 are in some scans sampled less frequently. The scans at smaller magnetic fields, especially when approaching $B = B_0 - 150$ mG contain fewer data points. Since the curves in that parameter range become comparably featureless, we used our experiemental resources to more accurately resolve the other sets.

List of Figures

List of Tables

Bibliography

1. Greiner, M., Mandel, O., Esslinger, T., Hänsch, T. W. & Bloch, I. Quantum phase transition from a superfluid to a Mott insulator in a gas of ultracold atoms. *nature* **415,** 39–44 (2002).
2. Bartenstein, M. *et al.* Crossover from a molecular Bose-Einstein condensate to a degenerate Fermi gas. *Physical review letters* **92,** 120401 (2004).
3. Bourdel, T. *et al.* Experimental study of the BEC-BCS crossover region in lithium 6. *Physical Review Letters* **93,** 050401 (2004).
4. Zwierlein, M. W., Abo-Shaeer, J. R., Schirotzek, A., Schunck, C. H. & Ketterle, W. Vortices and superfluidity in a strongly interacting Fermi gas. *Nature* **435,** 1047–1051 (2005).
5. Simon, J. *et al.* Quantum simulation of antiferromagnetic spin chains in an optical lattice. *Nature* **472,** 307–312 (2011).
6. Feynman, R. P. Simulating Physics with Computers. *International Journal of Theoretical Physics* **21,** 467–488 (1982).
7. Lloyd, S. Universal quantum simulators. *Science,* 1073–1078 (1996).
8. Hauke, P., Cucchietti, F. M., Tagliacozzo, L., Deutsch, I. & Lewenstein, M. Can one trust quantum simulators? *Reports on Progress in Physics* **75,** 082401 (2012).
9. Bloch, I., Dalibard, J. & Nascimbene, S. Quantum simulations with ultracold quantum gases. *Nature Physics* **8,** 267–276 (2012).
10. Gross, C. & Bloch, I. Quantum simulations with ultracold atoms in optical lattices. *Science* **357,** 995–1001 (2017).
11. Banerjee, D. *et al.* Atomic quantum simulation of dynamical gauge fields coupled to fermionic matter: From string breaking to evolution after a quench. *Physical review letters* **109,** 175302 (2012).
12. Zohar, E., Cirac, J. I. & Reznik, B. Quantum simulations of gauge theories with ultracold atoms: Local gauge invariance from angular-momentum conservation. *Physical Review A* **88,** 023617 (2013).
13. Zohar, E., Cirac, J. I. & Reznik, B. Quantum simulations of lattice gauge theories using ultracold atoms in optical lattices. *Reports on Progress in Physics* **79,** 014401 (Dec. 2015).
14. Dalmonte, M. & Montangero, S. Lattice gauge theory simulations in the quantum information era. *Contemporary Physics* **57,** 388–412 (2016).
15. Kasper, V., Hebenstreit, F., Oberthaler, M. & Berges, J. Schwinger pair production with ultracold atoms. *Physics Letters B* **760,** 742–746 (2016).

16. Kasper, V., Hebenstreit, F., Jendrzejewski, F., Oberthaler, M. K. & Berges, J. Implementing quantum electrodynamics with ultracold atomic systems. *New Journal of Physics* **19,** 023030 (Feb. 2017).
17. Zache, T. V. *et al.* Quantum simulation of lattice gauge theories using Wilson fermions. *Quantum Science and Technology* **3,** 034010 (June 2018).
18. Lee, P. A., Nagaosa, N. & Wen, X.-G. Doping a Mott insulator: Physics of high-temperature superconductivity. *Reviews of modern physics* **78,** 17 (2006).
19. Montvay, I. & Munster, G. *Quantum Fields on a Lattice Cambridge University Press* 1994.
20. Weinberg, S. The Making of the standard model. *The European Physical Journal C-Particles and Fields* **34,** 5–13 (2004).
21. Fodor, Z. & Hoelbling, C. Light hadron masses from lattice QCD. *Reviews of Modern Physics* **84,** 449 (2012).
22. Sauter, F. Über das Verhalten eines Elektrons im homogenen elektrischen Feld nach der relativistischen Theorie Diracs. *Zeitschrift für Physik* **69,** 742–764 (1931).
23. Heisenberg, W. & Euler, H. Folgerungen aus der diracschen theorie des positrons. *Zeitschrift für Physik* **98,** 714–732 (1936).
24. Schwinger, J. On gauge invariance and vacuum polarization. *Physical Review* **82,** 664 (1951).
25. Philipsen, O. & Wittig, H. String breaking in non-Abelian gauge theories with fundamental matter fields. *Physical Review Letters* **81,** 4056 (1998).
26. Bali, G. S. *et al.* Observation of string breaking in QCD. *Physical Review D* **71,** 114513 (2005).
27. Hebenstreit, F., Berges, J. & Gelfand, D. Real-time dynamics of string breaking. *Physical review letters* **111,** 201601 (2013).
28. Creutz, M., Jacobs, L. & Rebbi, C. Experiments with a gauge-invariant Ising system. *Physical Review Letters* **42,** 1390 (1979).
29. Martinez, E. A. *et al.* Real-time dynamics of lattice gauge theories with a few-qubit quantum computer. *Nature* **534,** 516–519 (2016).
30. Kokail, C. *et al.* Self-verifying variational quantum simulation of lattice models. *Nature* **569,** 355–360 (2019).
31. Bernien, H. *et al.* Probing many-body dynamics on a 51-atom quantum simulator. *Nature* **551,** 579–584 (2017).
32. Surace, F. M. *et al.* Lattice gauge theories and string dynamics in Rydberg atom quantum simulators. *arXiv preprint arXiv:1902.09551* (2019).
33. Clark, L. W. *et al.* Observation of density-dependent gauge fields in a Bose-Einstein condensate based on micromotion control in a shaken two-dimensional lattice. *Physical review letters* **121,** 030402 (2018).

34. Görg, F. *et al.* Realization of density-dependent Peierls phases to engineer quantized gauge fields coupled to ultracold matter. *Nature Physics* **15,** 1161–1167 (2019).
35. Schweizer, C. *et al.* Floquet approach to Z 2 lattice gauge theories with ultracold atoms in optical lattices. *Nature Physics* **15,** 1168–1173 (2019).
36. Mil, A. *et al.* A scalable realization of local U (1) gauge invariance in cold atomic mixtures. *Science* **367,** 1128–1130 (2020).
37. Li, X. *et al.* Coherent Heteronuclear Spin Dynamics in an Ultracold Spinor Mixture. *Phys. Rev. Lett.* **114,** 255301 (25 June 2015).
38. Stamper-Kurn, D. M. & Ueda, M. Spinor Bose gases: Symmetries, magnetism, and quantum dynamics. *Rev. Mod. Phys.* **85,** 1191–1244 (3 July 2013).
39. Appmeier, J. *Immersed Quantum Systems: A Sodium Bose-Einstein Condensate for Polaron Studies* PhD thesis (University of Heidelberg, 2010).
40. Rentrop, T. *Observation of the Phononic Lamb Shift in a Synthetic Vacuum* PhD thesis (University of Heidelberg, 2016).
41. Trautmann, A. *Spin Dynamics and Feshbach Resonances in Ultracold Sodium-Lithium Mixtures* PhD thesis (University of Heidelberg, 2016).
42. Olivares Legal, F. A. *Towards Lattice Gauge Theories in Ultracold Mixtures of Sodium and Lithium* PhD thesis (University of Heidelberg, 2018).
43. Zache, T. V. *Quantum simulation of high-energy physics with ultracold atoms* PhD thesis (University of Heidelberg, 2020). Unpublished thesis.
44. Davis, K. B. *et al.* Bose-Einstein Condensation in a Gas of Sodium Atoms. *Phys. Rev. Lett.* **75,** 3969–3973 (22 Nov. 1995).
45. Anderson, M. H., Ensher, J. R., Matthews, M. R., Wieman, C. E. & Cornell, E. A. Observation of Bose-Einstein Condensation in a Dilute Atomic Vapor. *Science* **269,** 198–201. ISSN: 00368075, 10959203 (1995).
46. Bradley, C. C., Sackett, C. A., Tollett, J. J. & Hulet, R. G. Evidence of Bose-Einstein Condensation in an Atomic Gas with Attractive Interactions. *Phys. Rev. Lett.* **75,** 1687–1690 (9 Aug. 1995).
47. Ensher, J. R., Jin, D. S., Matthews, M. R., Wieman, C. E. & Cornell, E. A. Bose-Einstein Condensation in a Dilute Gas: Measurement of Energy and Ground-State Occupation. *Phys. Rev. Lett.* **77,** 4984–4987 (25 Dec. 1996).
48. Jochim, S. *et al.* Bose-Einstein Condensation of Molecules. *Science* **302,** 2101–2103. ISSN: 0036-8075 (2003).
49. Castin, Y. & Dum, R. Bose-Einstein Condensates in Time Dependent Traps. *Phys. Rev. Lett.* **77,** 5315–5319 (27 Dec. 1996).
50. Minguzzi, A., Conti, S. & Tosi, M. P. The internal energy and condensate fraction of a trapped interacting Bose gas. *Journal of Physics: Condensed Matter* **9,** L33–L38 (Feb. 1997).

51. Dalfovo, F., Giorgini, S., Pitaevskii, L. P. & Stringari, S. Theory of Bose-Einstein condensation in trapped gases. *Rev. Mod. Phys.* **71,** 463–512 (3 Apr. 1999).
52. Timmermans, E., Côté, R. & Simbotin, I. Self-similar BEC dynamics: accuracy and applications. *Journal of Physics B: Atomic, Molecular and Optical Physics* **33,** 4157–4176 (Sept. 2000).
53. Pitaevskii, L. & Stringari, S. *Bose-Einstein Condensation and Superfluidity* (Oxford University Press, 2016).
54. Bagnato, V., Pritchard, D. E. & Kleppner, D. Bose-Einstein condensation in an external potential. *Phys. Rev. A* **35,** 4354–4358 (10 May 1987).
55. Pethick, C. J. & Smith, H. *Bose–Einstein condensation in dilute gases* (Cambridge university press, 2008).
56. Gross, E. P. Structure of a quantized vortex in boson systems. *Il Nuovo Cimento (1955-1965)* **20,** 454–477 (1961).
57. Pitaevskii, L. P. Vortex lines in an imperfect Bose gas. *Sov. Phys. JETP* **13,** 451–454 (1961).
58. Kagan, Y., Surkov, E. & Shlyapnikov, G. Evolution of a Bose-condensed gas under variations of the confining potential. *Physical Review A* **54,** R1753 (1996).
59. Scelle, R. *Dynamics and Motional Coherence of Fermions Immersed in a Bose Gas* PhD thesis (University of Heidelberg, 2013).
60. Langacker, P. *The Standard Model and Beyond* (Taylor & Francis, 2017).
61. Halzen, F. & Martin, A. D. *Quarks and leptons: an introductory course in modern particle physics* (Wiley, 1984).
62. Kogut, J. & Susskind, L. Hamiltonian formulation of Wilson's lattice gauge theories. *Phys. Rev. D* **11,** 395–408 (2 Jan. 1975).
63. Wilson, K. G. Confinement of quarks. *Phys. Rev. D* **10,** 2445–2459 (8 Oct. 1974).
64. Kogut, J. B. The lattice gauge theory approach to quantum chromodynamics. *Rev. Mod. Phys.* **55,** 775–836 (3 July 1983).
65. Smit, J. *Introduction to Quantum Fields on a Lattice* (Cambridge University Press, 2002).
66. Kasper, V. *Lattice Gauge Theory and Cold Atoms Out of Equilibrium* PhD thesis (University of Heidelberg, 2016).
67. Nielsen, H. & Ninomiya, M. Absence of neutrinos on a lattice: (I). Proof by homotopy theory. *Nuclear Physics B* **185,** 20–40 (1981).
68. Wilson, K. G. *New Phenomena in Subnuclear Physics* 69–142 (Springer, 1977).
69. Chandrasekharan, S. & Wiese, U.-J. Quantum link models: A discrete approach to gauge theories. *Nuclear Physics B* **492,** 455–471 (1997).
70. Banerjee, D. *et al.* Atomic Quantum Simulation of $\mathbf{U}(N)$ and $\mathrm{SU}(N)$ Non-Abelian Lattice Gauge Theories. *Phys. Rev. Lett.* **110,** 125303 (12 Mar. 2013).

71. Feynman, R. P., Vernon, F. L. & Hellwarth, R. W. Geometrical Representation of the Schrödinger Equation for Solving Maser Problems. *Journal of Applied Physics* **28,** 49–52 (1957).

72. Landau, L. & Lifshitz, E. *Quantum Mechanics* (Pergamon Press, 2002).

73. Strobel, H. *Fisher Information and entanglement of non-Gaussian spin states* PhD thesis (University of Heidelberg, 2015).

74. Aidelsburger, M. *et al.* Experimental realization of strong effective magnetic fields in an optical lattice. *Physical review letters* **107,** 255301 (2011).

75. Jaksch, D. & Zoller, P. Creation of effective magnetic fields in optical lattices: the Hofstadter butterfly for cold neutral atoms. *New Journal of Physics* **5,** 56 (2003).

76. Dao, T.-L., Carusotto, I. & Georges, A. Probing quasiparticle states in strongly interacting atomic gases by momentum-resolved Raman photoemission spectroscopy. *Physical Review A* **80,** 023627 (2009).

77. Miyake, H., Siviloglou, G. A., Kennedy, C. J., Burton, W. C. & Ketterle, W. Realizing the Harper Hamiltonian with Laser-Assisted Tunneling in Optical Lattices. *Phys. Rev. Lett.* **111,** 185302 (18 Oct. 2013).

78. Stan, C. A. & Ketterle, W. Multiple species atom source for laser-cooling experiments. *Review of Scientific Instruments* **76,** 063113 (2005).

79. Weis, S. *Setup of a Laser System for Ultracold Sodium - Towards a Degenerate Gas of Ultracold Fermions* (Diploma Thesis, University of Heidelberg, 2007).

80. Krieger, J. *Zeeman-Slower und Experimentsteuerung für das NaLi-Experiment* (Diploma Thesis, University of Heidelberg, 2008).

81. Hadzibabic, Z. *et al.* Two-Species Mixture of Quantum Degenerate Bose and Fermi Gases. *Phys. Rev. Lett.* **88,** 160401 (16 Apr. 2002).

82. Mewes, M.-O. *et al.* Bose-Einstein Condensation in a Tightly Confining dc Magnetic Trap. *Phys. Rev. Lett.* **77,** 416–419 (3 July 1996).

83. Van der Stam, K. M. R., Kuijk, A., Meppelink, R., Vogels, J. M. & van der Straten, P. Spin-polarizing cold sodium atoms in a strong magnetic field. *Phys. Rev. A* **73,** 063412 (6 June 2006).

84. Myatt, C. J., Burt, E. A., Ghrist, R. W., Cornell, E. A. & Wieman, C. E. Production of Two Overlapping Bose-Einstein Condensates by Sympathetic Cooling. *Phys. Rev. Lett.* **78,** 586–589 (4 Jan. 1997).

85. Metcalf, H. J. & Peter, v. d. S. *Laser Cooling and Trapping* (Springer, 1999).

86. Ketterle, W., Durfee, D., Stamper-Kurn, D., *et al.* Making, probing and understanding Bose-Einstein condensates. *arXiv preprint cond-mat/9904034* **5** (1999).

87. Gajdacz, M. *et al.* Non-destructive Faraday imaging of dynamically controlled ultracold atoms. *Review of Scientific Instruments* **84,** 083105 (2013).

88. Reinaudi, G., Lahaye, T., Wang, Z. & Guéry-Odelin, D. Strong saturation absorption imaging of dense clouds of ultracold atoms. *Optics letters* **32,** 3143–3145 (2007).

89. Mil, A. *Design and Implementation of a Versatile Imaging Objective for Imaging of Ultracold Mixtures of Sodium and Lithium* (Master Thesis, University of Heidelberg, 2016).

90. Schymik, K.-N. *Implementing an Optical Accordion Lattice for the Realization of a Quantized Otto Cycle* (Master Thesis, University of Heidelberg, 2018).

91. Kwon, W. J., Choi, J.-y. & Shin, Y.-i. Calibration of saturation absorption imaging of ultracold atom clouds. *Journal of the Korean Physical Society* **61,** 1970–1974 (2012).

92. Muessel, W. *et al.* Optimized absorption imaging of mesoscopic atomic clouds. *Applied Physics B* **113,** 69–73 (2013).

93. Hueck, K. *et al.* Calibrating high intensity absorption imaging of ultracold atoms. *Opt. Express* **25,** 8670–8679 (Apr. 2017).

94. Reinaudi, G. *Manipulation et refroidissement par évaporation forcée d'ensembles atomiques ultra-froids pour la production d'un jet intense dans le régime de dégénérescence quantique: vers l'obtention d'un" laser à atomes continu"* PhD thesis (2008).

95. Kuppens, S. J. M., Corwin, K. L., Miller, K. W., Chupp, T. E. & Wieman, C. E. Loading an optical dipole trap. *Phys. Rev. A* **62,** 013406 (1 June 2000).

96. Adams, C. S., Lee, H. J., Davidson, N., Kasevich, M. & Chu, S. Evaporative Cooling in a Crossed Dipole Trap. *Phys. Rev. Lett.* **74,** 3577–3580 (18 May 1995).

97. Davidson, N., Jin Lee, H., Adams, C. S., Kasevich, M. & Chu, S. Long Atomic Coherence Times in an Optical Dipole Trap. *Phys. Rev. Lett.* **74,** 1311–1314 (8 Feb. 1995).

98. Kinoshita, T., Wenger, T. & Weiss, D. S. All-optical Bose-Einstein condensation using a compressible crossed dipole trap. *Phys. Rev. A* **71,** 011602 (1 Jan. 2005).

99. Grimm, R., Weidemüller, M. & Ovchinnikov, Y. B. Optical Dipole Traps for Neutral Atoms. *Advances in Atomic Molecular and Optical Physics* **42,** 95–170 (2000).

100. Ospelkaus, S., Ospelkaus, C., Humbert, L., Sengstock, K. & Bongs, K. Tuning of Heteronuclear Interactions in a Degenerate Fermi-Bose Mixture. *Phys. Rev. Lett.* **97,** 120403 (12 Sept. 2006).

101. Fukuhara, T., Sugawa, S., Takasu, Y. & Takahashi, Y. All-optical formation of quantum degenerate mixtures. *Phys. Rev. A* **79,** 021601 (2 Feb. 2009).

102. Wang, F., Li, X., Xiong, D. & Wang, D. A double species23Na and87Rb Bose–Einstein condensate with tunable miscibility via an interspecies Feshbach resonance. *Journal of Physics B: Atomic, Molecular and Optical Physics* **49,** 015302 (Nov. 2015).

103. Steck, D. A. Sodium D line data. *Report, Los Alamos National Laboratory, Los Alamos* **124** (2000).

104. Breit, G. & Rabi, I. I. Measurement of Nuclear Spin. *Phys. Rev.* **38,** 2082–2083 (11 Dec. 1931).

105. Ockeloen, C. F., Tauschinsky, A. F., Spreeuw, R. J. C. & Whitlock, S. Detection of small atom numbers through image processing. *Phys. Rev. A* **82,** 061606 (6 Dec. 2010).

106. Niu, L. *et al.* Optimized fringe removal algorithm for absorption images. *Applied Physics Letters* **113,** 144103 (2018).

107. Cheney, W. & Kincaid, D. *Linear Algebra: Theory and Applications* 544 (Jones and Bartlett, 2009).

108. *HDF official website* `https://www.hdfgroup.org/`. Accessed: 2020-01-27.

109. Ehrenfest, P. Bemerkung über die angenäherte Gültigkeit der klassischen Mechanik innerhalb der Quantenmechanik. *Z. Phys.* **45,** 455–457 (1927).

110. Smith, H. *Introduction to Quantum Mechanics* 108–109 (World Scientific Pub Co Inc, 1991).

111. Lehtovaara, L., Toivanen, J. & Eloranta, J. Solution of time-independent Schrödinger equation by the imaginary time propagation method. *Journal of Computational Physics* **221,** 148–157 (2007).

112. Chin, S. A., Janecek, S. & Krotscheck, E. Any order imaginary time propagation method for solving the Schrödinger equation. *Chemical Physics Letters* **470,** 342–346 (2009).

113. Bader, P., Blanes, S. & Casas, F. Solving the Schrödinger eigenvalue problem by the imaginary time propagation technique using splitting methods with complex coefficients. *The Journal of chemical physics* **139,** 124117 (2013).

114. Breuer, H.-P., Petruccione, F., *et al. The theory of open quantum systems* (Oxford University Press on Demand, 2002).

115. Manzano, D. A short introduction to the Lindblad Master Equation. *AIP Advances* **10,** 025106 (2020).

116. Nicklas, E. *A new tool for miscibility control: Linear coupling* PhD thesis (University of Heidelberg, 2013).

117. Timmermans, E. Phase separation of Bose-Einstein condensates. *Physical review letters* **81,** 5718 (1998).

118. Schuster, T. *Feshbach resonances and periodic potentials in ultracold Bose-Fermi mixtures* PhD thesis (University of Heidelberg, 2012).

119. Prentiss, M. *et al.* Atomic-density-dependent losses in an optical trap. *Optics letters* **13,** 452–454 (1988).

120. Tojo, S. *et al.* Spin-dependent inelastic collisions in spin-2 Bose-Einstein condensates. *Physical Review A* **80,** 042704 (2009).

121. Burt, E. *et al.* Coherence, correlations, and collisions: What one learns about Bose-Einstein condensates from their decay. *Physical Review Letters* **79,** 337 (1997).

122. Söding, J. *et al.* Three-body decay of a rubidium Bose–Einstein condensate. *Applied physics B* **69,** 257–261 (1999).

123. Kraemer, T. *et al.* Evidence for Efimov quantum states in an ultracold gas of caesium atoms. *Nature* **440,** 315–318 (2006).

124. Gall, M. *Active Magnetic Field Stabilisation for Ultracold Sodium Lithium Mixtures* (Master Thesis, University of Heidelberg, 2015).

125. Itano, W. M. *et al.* Quantum projection noise: Population fluctuations in two-level systems. *Physical Review A* **47,** 3554 (1993).

126. Scelle, R., Rentrop, T., Trautmann, A., Schuster, T. & Oberthaler, M. Motional coherence of fermions immersed in a Bose gas. *Physical review letters* **111,** 070401 (2013).

127. Rentrop, T. *et al.* Observation of the phononic Lamb shift with a synthetic vacuum. *arXiv preprint arXiv:1605.01874* (2016).

Acknowledgements

I am very grateful for having received support from so many people during the last years, which has made my exhausting phd-endeavour possible.

- I thank Fred for his support and supervision since the very beginning, when I joined him as a master student. He welcomed me into his new group and together we faced the task of taming the NaLi experiment. He has provided guidance to me whenever I felt lost in view of the insurmountable challenges ahead of us. His relentless effort to bring our mutual project forward has always been inspiring. Never have I seen him being shy to get his hands dirty, be it crawling across the optical table in the lab or tedious debugging of analysis code. Working with you has been a great experience, thank you.
- Many thanks to Selim, who willingly agreed as second referee for this thesis, even when he already had a whole lot of other theses to review.
- I thank all my collaborators in the gauge invariance project, in particular Markus and Jürgen, who were the first to be bold enough to even think about something like this.
- This work would not have been possible without my collegues at matterwave/SynQS. Everyone in this group has always been ready to help me out. Be it with discussions, good advice or borrowing lab equipment. All the great group activities proved that we have by far the greatest team spirit in the kip. It was an honor for me to be part of this great community.
- I thank all former NaLi members, who have put a tremendous effort into building the NaLi machine. Despite all of its stubbornness and flaws the NaLi was able to contribute to science.
- I thank all current members of the NaLi/SoPa team for the great atmosphere in the office/lab as well as for introducing me to all kinds of culinary treats.
- Special thanks goes to Torsten, who has brought physics back to my phd life, after it has consisted of treadmill lab work for an eternity. Our discussions have revived my fascination for the small and big questions in physics, something that I have lost track of. Thank you for that.
- I thank Helmut for being an almost infinite source of good advice, great jokes and lots of essential tricks that make you survive on the battleground of experimental physics.

- I thank Simon for our interesting discussions about god, philosophy and organs. Also a big thanks for proofreading this manuscript.
- I thank my physics alpha one gang which is accompanying me since my first days in Heidelberg. Without you I would not be as crazy as I am now, thank you.
- I thank my parents and my sisters for their support and trust in me. They gave me the possibility to do what I am doing.
- Finally I thank the most important person. Hannah, without you I would not be who I am now. You have always supported me, always trusted in me and in my strength to overcome all obstacles ahead of me, even when I have doubted it myself. You have encouraged me when I felt upset and calmed me down when I was furious. I can not imagine to live without you, thank you for everything.

Erklärung:

Ich versichere, dass ich diese Arbeit selbstständig verfasst habe und keine anderen als die angegebenen Quellen und Hilfsmittel benutzt habe.

Heidelberg, den 16.03.2020 . . . . . .